UNIVERSITY OF CALIFORNIA, SAN DIEGO

Fluorescence resonance energy transfer-based visualization and actuation of molecular signaling transductions for controlling cellular behaviors

A dissertation submitted in partial satisfaction of the

requirements for the degree

Doctor of Philosophy

in

Bioengineering

by

Pengzhi Wang

Committee in Charge:

Professor Yingxiao Wang, Chair
Professor Michael W. Berns
Professor Adam J. Engler
Professor Yu-Hwa Lo
Professor Andrew D. Mcculloch
Professor Robert L. Sah

2018

The dissertation of Pengzhi Wang is approved, and it is acceptable in quality and form for publication on microfilm and electronically:

Chair

University of California, San Diego

2018

Epigraph

Was mich nicht umbringt, macht mich stärker. - Friedrich Nietzsche

With self-discipline most anything is possible. - Theodore Roosevelt

Strive For Greatness.

Table of Contents

Signature Page ..... **iii**

Epigraph ..... **iv**

List of Figures ..... **vii**

List of Tables ..... **x**

Acknowledgements ..... **xi**

Vita ..... **xv**

Publications ..... **xv**

Fields of Study ..... **xvi**

Abstract of the Dissertation ..... **xvii**

Chapter 1: General Information **1**
1.1. Overview of the thesis 1
1.2. Introduction 3
1.2.1. Directed evolution and yeast display for protein engineering 3
1.2.2. FPs and FRET-based biosensors 3
1.2.3. Robotic laser scissors 4
1.2.4. Intercellular communications and Src signaling 4
1.2.5. Cancer, immunity and engineered T cell based therapeutics 4

Chapter 2: Development and Characterization of Src FRET Biosensors Based on High-Throughput Screening Platform **6**
2.1. Abstract 6
2.2. Introduction 6
2.3. Materials and Methods 8
2.4. Results and Discussion 13
2.4.1. High-throughput screening of the substrate-binding affinity toward a library of *c-Src* SH2 domains 13
2.4.2. Characterization of Src biosensors with identified mutations in live mammalian cells 15

2.4.3. Characterization of the identified Src biosensors *in vitro* 17
2.5. Conclusion 17
2.6. Figures 20

Chapter 3: Visualizing Spatiotemporal Dynamics of Intercellular Signaling Transmission by An Integrated Photonic Approach 36
3.1. Abstract 36
3.2. Introduction 37
3.3. Materials and Methods 38
3.4. Results and Discussion 40
3.4.1. Observation of Src signaling transmission following the laser-induced disruption of cell-cell contacts 40
3.4.2. Regulation of Src signaling activation following the disruption of cell-cell contacts through the passive cytoskeletal structure but not through the active actomyosin contractility 41
3.5. Conclusion 42
3.6. Figures 43

Chapter 4: Engineering Immune Cells for Cancer Therapy Through Synthetic Molecular Machinery 47
4.1. Abstract 47
4.2. Introduction 47
4.3. Materials and Methods 55
4.4. Results and Discussion 65
4.4.1. Development and characterization of synthetic molecular machineries 65
4.4.2. Engineering T cells for overcoming PD-1/PD-L1 signaling mediated T cell inhibition via synthetic molecular machineries 69
4.5. Conclusion 76
4.6. Figures and Tables 78

Chapter 5: Summary and Future Directions 103

References 106

List of Figures

Figure 2.1: The optimal *c-Src* SH2 domain variants and tyrosine kinase substrates identified by high-throughput screening. 20

Figure 2.2: Characterization of FRET-based Src biosensors in living mammalian cells. 22

Figure 2.3: System schematic of high-throughput screening for FRET-based biosensors. 24

Figure 2.4: Optimizing conditions and validating protein expression for the yeast display system. 25

Figure 2.5: Optimizing substrate peptides for the yeast display system. 27

Figure 2.6: Flow cytometry result of yeast surface displaying different SH2 domains against the EIpYGEF phosphopeptide. 29

Figure 2.7: The design of the FRET-based Src biosensor. 30

Figure 2.8: Characterization of FRET-based Src biosensors in mouse embryonic fibroblast cells. 31

Figure 2.9: Histogram of the sensitivities of different FRET-based Src biosensors. 32

Figure 2.10: Characterization of FRET-based Src biosensors *in vitro*. 33

Figure 2.11: Characterization of the inactive FRET-based Src biosensors *in vitro* and confirmation of purified Src biosensors. 35

Figure 3.1: Regulation of the transient Src activation following the laser-induced disruption of cell-cell contacts. 43

Figure 3.2: The responses of different FRET-based Src biosensors in PtK2 cells subjected to the laser-induced disruption of cell-cell contacts. 45

Figure 3.3: Effects of Myosin light chain kinase inhibitor on FAK activity in PtK2 cells. 46

Figure 4.1: The general domain organization of integrated sensing and activating proteins (iSNAPs) for ZAP70 and SYK. 78

Figure 4.2: The general working principle of iSNAPs for ZAP70 and SYK. 79

Figure 4.3: The FRET responses of iSNAPs for ZAP70 and SYK in response to different stimulants in living mammalian cells. 80

Figure 4.4: The normalized emission ratio time courses of different iSNAPs for ZAP70 and SYK in response to pervanadate (PVD) stimulation in HeLa cells. 81

Figure 4.5: The domain organization of His-tagged iSNAPs for ZAP70 and SYK. 83

Figure 4.6: Characterization of iSNAP-ZAP70s *in vitro*. 84

Figure 4.7: The domain organization of different human PD-1 fused iSNAPs for ZAP70 and SYK. 85

Figure 4.8: The general working principle of truncated human PD-1 fused iSNAPs for ZAP70 and SYK in living mammalian cells. 86

Figure 4.9: The FRET responses of different human PD-1 fused iSNAPs for ZAP70 and SYK in response to pervanadate (PVD) stimulation in HeLa cells. 87

Figure 4.10: The emission ratio time courses of different human PD-1 fused iSNAPs for ZAP70 and SYK in response to pervanadate (PVD) stimulation in HeLa cells. 88

Figure 4.11: Performances of truncated human PD-1 fused iSNAP-ZAP70s in Jurkat cells under pervanadate (PVD) stimulation. 89

Figure 4.12: Confirmation of biotinylated purified PD-L1 by protein gel eletrophoresis. 90

Figure 4.13: The working principle of truncated human PD-1 fused iSNAP-Z1 in living mammalian cells upon PD-L1 ligation. 91

Figure 4.14: Time-lapse imaging in HeLa cells expressing truncated PD-1 fused iSNAP-ZAP70s in response to particle-bound PD-L1. 92

Figure 4.15: The FRET responses of different human PD-1 fused iSNAPs for ZAP70 in response to particle-bound PD-L1 in HeLa cells. 93

Figure 4.16: Time-lapse imaging in Jurkat cells expressing truncated PD-1 fused iSNAP-ZAP70s in response to particle-bound PD-L1. 94

Figure 4.17: The FRET responses of truncated human PD-1 fused iSNAPs for ZAP70 in response to particle-bound PD-L1 in Jurkat cells. 95

Figure 4.18: Schematic of the activation of T cells expressing PD-1 fused iSNAP-Z1 upon the engagement of PD-L1-expressing cancer cells. 96

Figure 4.19: CD69 activation in Jurkat cells expressing different truncated human PD-1 fused iSNAP-ZAP70s during co-culture with PD-L1 expressing cancer cells. 97

Figure 4.20: Two independent mechanisms of ZAP70 activation. 98

Figure 4.21: The domain organization of truncated human PD-1-fused iSNAPs for ZAP70 with extra internal linkers. 99

List of Tables

Table 4.1: The substrate sequences of different iSNAPs for ZAP70 and SYK. 100

Table 4.2: The kinase activity assay results of iSNAP-ZAP70s. 101

Table 4.3: The descriptions of different human PD-1 fused iSNAPs for ZAP70 and SYK..... 102

Acknowledgements

First of all, I must thank Prof. Peter Yingxiao Wang for his advice, inspiration and help without reserve throughout my time in graduate school. I greatly appreciate Prof. Wang for accepting me into his lab as well as everything that I learned from him from both inside and outside of academia. He devoted tremendous amount of time and effort to teach and train me despite other obligations required by his faculty position. I truly thank him for giving me freedom to make mistakes and explore without limits, and for his great consideration about my wellbeing and future. All these allowed me to grow and become the scientist that I am today. My work wouldn't have been possible without his guidance and support.

Second, to Prof. Adam J. Engler, Prof. Yu-Hwa Lo, Prof. Andrew D. McCulloch and Prof. Robert L. Sah, I would like to sincerely thank and acknowledge them for all the great patience, insights, effort and time about this dissertation. Their advice to me was invaluable on many occasions. I learned enormously from many enlightening conversations and feel privileged to have had these opportunities to discuss and work with them.

I am also hugely indebted to Prof. Michael W. Berns. Working with him over the past years has significantly influenced my research and thoughts. Working with the members of his research group here was also an immeasurably positive and enriching experience, especially Dr. Daryl Preece, Dr. Veronica Gomez, Dr. Michelle Duquette-Huber and Vikash Morar. I would like to thank Dr. Linda Z. Shi for everything that she did for me, and I count myself extremely lucky to have had her as a colleague and friend over my time here.

I would also like to express my heartfelt gratitude to all my collaborators, Prof. Shu Chien, Prof. Chengbiao Wu, Prof. Huimin Zhao, Prof. Yu-Hwa Lo, Prof. Shawn S.C. Li, Prof. Alex Strongin and all their lab members, especially Dr. Hsin-Hung Lin, Phu Nguyen, Dr. Yi-shuan J. Li, Gerard N. Norwich, Dr. Xiaobei Zhao, Yue Hu, Dr. Jing Liang and Yu-Jui Chiu. In particular, partial work presented in Chapter 2 was done in collaboration with Prof. Zhao's research group, the work presented in Chapter 3 was done in collaboration with Prof. Berns' research group, and fractional work presented in Chapter 4 was done with the help from Prof. Shu Chien's research group.

This work also significantly benefits from the support, friendship, teamwork and conversations with my past and current labmates Dr. Jie Sun, Dr. Mingxing Ouyang, Dr. Shaoying Lu, Dr. Lei Lei, Dr. Qin Peng, Dr. Ziliang Huang, Dr. Yan Huang, Dr. Ping Zhang, Dr. Xianwei Liu, Dr. Yan Zhang, Dr. Binbin Cheng, Dr. Yu-Chi Chen, Dr. Jihye Seong, Dr. Taejin Kim, Dr. Li-Jung Lin, Dr. John Eichorst, Molly E. Allen, Lunan Shao, Chi-Wei Man, Yiwen Shi, Mint P. Limsakul, Rongxue Wan, Yi Wang, Yijia Pan, Shirley Y. Wu, Jason Fan, Rinoka Sato, Yanmin Ji, Chris Chu, Jenny Wu, Shannon Laub, Qin Qin, Ted Y. Dong, Xiaoqi Chai, Linshan Zhu, Ya Gong, Eddie Chung, Wade Zhang and many others. In particular, this work wouldn't have become realistic without the training and mentoring from Dr. Jie Sun and Dr. Mingxing Ouyang. This lab is indeed unique for the strong sense of community and profession. I truly appreciate being part of it and enjoy all the good times together along this long journey towards my doctorate degree.

I would also like to thank those who have guided my research career and cultivated my scientific abilities earlier before the graduate school. In particular, I would like to thank Prof. Yi Zhong, Dr. Cheng Huang and Lianzhang Wang for guiding and

supporting me as an undergraduate research assistant and shaped my scientific thinking and reasoning abilities in Tsinghua University. I would like to thank all the Yi lab members for show me the true meaning of being critical and focused. I have gained a tremendous amount of knowledge and insights along those journeys.

Moreover, my experience as a graduate student would have been much poorer without our great administration stuff and course faculty instructors of the Bioengineering department, especially Dear Jan Lenington, Kelly Thorpe, Prof. Karen L. Christman, Prof. Todd P. Coleman, and Prof. Ratneshwar Lal. My thanks go to them.

In addition, I would like to acknowledge a few individuals from whom I have learned quite much about how to grow mentally, physically and spiritually along the way towards my graduation. For their friendship and for many edifying talks and discussions, I would like to thank particularly Binbin Li, Suzhen Lin, Zhizhong Li and all the other SDTHAA members, Matt Cai, Dr. Shuai Li, Dr. Xin Li, Zheng Zhong, Jun Wang, Owen Tan, Daniel Chen, Cheryl Cai, Joanne Chan, Kevin Zhuang, Jeff Wang, Yanjin Li, Jimmy Wu, Kevin Tu, Terri Dowie and all the other lovely gym/bball group members, all my dear friends in UIUC neuroscience program, in particular Samuel N. Beshers and Dr. Aki Nikolaidis, Prof. Qingtao Song, Dr. Sangpil Yoon, Dr. Zachary Breig, Dr. Chi Zhang, Zhe Yang, Kaiwen Zhang, Shangzhong Li, Dr. Guoliang Chai, Haidong Tang, Dr. Yang Song, Dr. Yue Zhang, Dr. Peng Zhao, C. Zhang, Dr. Renee Yang, J.W., Boyang Zhang, Lingzi Hu, Dr. Tong Si, Yu Sang, Dr. Bin Xie, Dr. Shuyin Liu, Ana M. Moreno, Joshua Francois, Dr. Aereas Aung, Dr. Han Liang Lim, Dr. Margie Mathewson, Clement Lee, Dr. Chris Ochs, and many old and new friends in U.S. or China or Europe.

I would also like to acknowledge all the funding agencies (National Institutes of Health, National Science Foundation, UC San Diego, Beckman Laser Institute Foundation, Air Force Office of Scientific Research, National Natural Science Foundation of China) for providing the rare opportunities and their generosity and effort have instilled in me a sense of desire to give back to the community in the future in any possible way.

Lastly, I would like to thank my dear parents, W.W. and H.Z., for giving me the priceless care and support to ensure my bright future. Without the basis they established, I couldn't possibly think to reach for my goals and I deeply appreciate their unconditional love and sacrifices. Additionally, I would like to give my special thanks to my dear friends Molly, Chi and Jan, I couldn't imagine how to finish filing my final graduation paperwork remotely without their generous and huge help.

Thank you all, my family and friends. All of you made this journey possible. I sincerely wish you all the best in your future endeavors and our paths will cross again.

Chapter 2 and Chapter 3, in full, are currently being prepared for submission for publication of the material. "Visualizing spatiotemporal dynamics of intercellular mechanotransmission upon wounding". Wang, Pengzhi; Liang, Jing; Shi, Linda Z.; Wang, Yi; Zhang, Ping; Ouyang, Mingxing; Preece, Daryl; Peng, Qin; Shao, Lunan; Fan, Jason; Sun, Jie; Li, Shawn Shun-Cheng; Berns, Michael W.; Zhao, Huimin; Wang, Yingxiao. The dissertation author was the primary investigator and author of this material.

Vita

2011 Bachelor of Science in Fundamental Sciences (Chemistry & Biology),
Department of Chemistry, Tsinghua University, Beijing, China

2015 Master of Science in Bioengineering,
University of California San Diego, La Jolla, United States

2018 Doctor of Philosophy in Bioengineering,
University of California San Diego, La Jolla, United States

Publications

Huang C, Zheng X, Zhao H, Li M, **Wang P**, Xie Z, Wang L, Zhong Y. A permissive role of mushroom body α/β core neurons in long-term memory consolidation in Drosophila. Current Biology. 2012 Nov 6;22(21):1981-9.

Huang C, **Wang P**, Xie Z, Wang L, Zhong Y. The differential requirement of mushroom body α/β subdivisions in long-term memory retrieval in Drosophila. Protein & cell. 2013 Jul 1;4(7):512-9.

Wang P, Liang J, Shi LZ, Wang Y, Preece D, Li SS, Berns MW, Zhao H, Wang Y. Directed evolution optimized FRET biosensors to visualize the laser-induced mechanotransduction between neighboring cells. (In preparation)

Ouyang M, Qin Q, **Wang P**, Wan R, Laub S, Lu S, Wang Y. Visualizing the spatial regulation of Fyn kinase at lipid rafts by a novel FRET biosensor in live cells. (In preparation)

Yoon S, **Wang P**, Peng Q, Wang Y, Shung KK. Acoustic-transfection for genomic manipulation of single-cells using high frequency ultrasound. (Under review)

Sun J, Lei L, ..., **Wang P**, …, Wang Y. Engineered Proteins with Sensing and Activating Modules for Automated Reprogramming of Cellular Functions. (Under submission)

Peng Q, ..., **Wang P**, …, Wang Y. A dynamic coordination between Histone phosphorylation and methylation in regulating chromatin structures during mitosis. (In preparation)

Fields of Study

Major Field: Bioengineering and Biomedical Engineering

Studies in Biophotonics, Molecular and Cellular Engineering, Synthetic Biology, Immunology, Cancer Biology

Abstract of the Dissertation

Fluorescence resonance energy transfer-based visualization and actuation of molecular signaling transductions for controlling cellular behaviors

by

Pengzhi Wang

Doctor of Philosophy in Bioengineering

University of California, San Diego, 2018

Professor Yingxiao Wang, Chair

Understanding and engineering of complex biological systems are key challenges to the scientific community for addressing health problems, especially diseases. Studies of biological systems can vary in scale from molecules, cells, to entire organisms. Cells,

as the basic building blocks of life, compose various biological entities of higher order and precisely control both structures and functions. Therefore, it is of vital importance to understand how cell functions and behaviors are regulated in order to engineer and manipulate cell behaviors. Recently, advances in molecular imaging technologies and synthetic biology approaches have enabled us to better detect and manipulate cell signals and behaviors, and provide a broad set of tools to influence and revolutionize basic research, medicine and therapy. In my dissertation, a general high-throughput platform has been established to systematically optimize biosensors and a new Src biosensor with high sensitivity has been developed accordingly. Combining fluorescence/Förster resonance energy transfer microscopy and laser scissors technology, the signaling transmission between neighboring cells and the underlying mechanism could thus be revealed, which could provide a cell model to understand intercellular communications and wound healing process. Furthermore, I have successfully developed, characterized and demonstrated specific molecular machineries to program cell behaviors by rewiring molecular signaling pathways, specifically immune responses in immune cells against cancer cells. These new tools and understanding may open a new avenue towards cancer therapy and lead to potential therapeutic strategies.

Chapter 1: General Information

1.1. Overview of the thesis

This thesis comprises five chapters in total. In this Chapter 1, I give a brief overview of the thesis as well as a literature review on the background of my thesis work. Specifically, I focus on directed evolution and molecular display for generating large libraries for protein engineering. Next, I briefly describe fluorescent proteins (FPs) and fluorescence/Förster resonance energy transfer (FRET) microscopy and the cellular imaging using genetically encoded FRET-based biosensors as well as a powerful photonic approach called robotic laser scissors. I also describe cell-cell communications and Src kinase signaling. Lastly, I briefly introduce cancer diseases, immunity and discuss the power of engineered T cell based cancer therapy by synthetic biology approaches.

In Chapter 2, I describe a general high-throughput platform based on directed evolution to systematically optimize a FRET-based biosensor for reporting the activity of Src kinase. The yeast surface display method and site-saturated mutagenesis were employed to develop mutant libraries for the identification of phosphopeptide sequences and Src homolog 2 (SH2) domain mutants with improved binding affinity, which ultimately led to a drastic improvement of the biosensor sensitivity after the thorough characterization. In Chapter 3, I describe how I integrated the FRET microscopy with laser scissors, a unique, highly precise micro-manipulation photonic system, and applied the newly developed Src FRET-based biosensor to reveal how cells react biochemically to photonic-driven physical perturbations from neighboring cells. A transient Src

activation was observed in epithelial cells following the physical disruption of cell-cell contacts at neighboring cells using a femtosecond laser pulse, which is dependent on passive cytoskeletal structure but not active actomyosin contractility. The study in Chapters 2 and 3 is about to submit to the journal.

In addition to detecting and understanding cell signals and behaviors, I also sought to use these tools to manipulate cell signals and behaviors. Therefore, in Chapter 4, I describe shifting my research focus towards developing molecular machineries, called the integrated Sensing aNd Activating Proteins (iSNAPs). First, I fully characterized both the sensing and activating functions of iSNAPs. I then introduced the optimal iSNAP into T cells to overcome immune exhaustion by engineering adaptive immune responses and demonstrated the potential significance for immunotherapy purposes. This study in Chapter 4 will soon be prepared for the journal submission.

In the last chapter, I summarize my thesis work and discussed the potential outcomes and applications of the tools that I have developed.

In summary, of my thesis work, a general platform has been established to systematically develop FRET-based biosensors in a high-throughput fashion. Moreover, integrating synthetic biology approaches and photonics technologies as a toolkit allows people to not only detect specific biological signaling events via FRET-based biosensors, but also to manipulate various cell signals and behaviors via iSNAPs. Together, these tools should advance our understanding of complex biological systems and may provide innovative and precise therapeutic tools for better cancer treatment.

1.2. Introduction

1.2.1. Directed evolution and yeast display for protein engineering

The emerging synthetic biology approaches have enabled us to engineer novel cell functions and behaviors by providing various new classes of useful molecular and modular designs [1, 2]. Different protein engineering strategies have been utilized to understand, design and engineer such biomolecules that can be applied for research, industrial and therapeutic purposes. In particular, directed evolution of molecules provides a high-throughput method to generate great genetic diversity and identify proteins of interest with desired properties, especially in cases where rational designs and engineering are ineffective [3, 4]. Cell display methods, such as bacterial and yeast surface display, allows for generating large libraries of proteins, which can be screened by fluorescence-activated cell sorting (FACS) technology to identify desired proteins [5].

1.2.2. FPs and FRET-based biosensors

It is very well known that the Nobel Prize in Chemistry 2008 was awarded to Osamu Shimomura, Martin Chalfie and Roger Y. Tsien "for the discovery and development of the green fluorescent protein, GFP". Since the GFP was discovered from jellyfish *Aequorea victoria*, a broad set of FPs with different colors has been developed and applied for biological imaging in biochemistry, cell biology and other biology disciplines [6-8]. Powerful molecular imaging approaches using FRET microscopy have been employed for cell biology studies [9], and numerous genetically encoded biosensors based on FPs and FRET have been developed to visualize and quantify molecular and cellular signaling events with high spatiotemporal resolutions in single live cells [10-12].

1.2.3. Robotic laser scissors

A photonic approach, called robotic laser scissors microscopy, enables us to precisely ablate subcellular targets of single live cells [13-15]. Meanwhile, cell viability is not affected and the surrounding regions of the laser focal spot remain intact. The use of this photonic approach allows us to introduce local physical perturbations on various cellular structures and investigate how cell structures and functions are correlated in a wide variety of studies [16-19].

1.2.4. Intercellular communications and Src signaling

Intercellular communications in multicellular organisms are crucial to their functions and behaviors, and cell-cell adhesion proteins are commonly believed to regulate tissue morphogenesis and enable communication between adjacent cells [20-22]. It is also known that Src kinase, the principal member of Src family kinases (SFKs), is a key signaling regulator linking both cellular and nuclear mechanotransduction, including integrin-, adhesion-, cytoskeleton- and nucleoskeleton-associated signal transductions [23-28]. For instance, studies on the E-cadherin signaling suggest Src family kinases are involved in modulating the interaction of E-cadherin with the cytoskeleton and maintaining the integrity of E-cadherin-mediated cell-cell adhesion [29-33].

1.2.5. Cancer, immunity and engineered T cell based therapeutics

At present, cancer disease with poor prognosis and treatment becomes one of the most dangerous and deadliest diseases for human beings. The public is more and more aware of the quality of life, and has hastened more effective and safer cancer treatments than conventional cancer therapy. With better understanding on cancer diseases, people have found that one major cause is that tumor can escape the immune surveillance to

enhance their survival, called cancer immune evasion or tumor escape [34], and suppress immune system by interfering with the anti-cancer immune responses and inhibiting immune cell functions against tumor cells [35]. T lymphocyte plays a central role in adaptive immunity and its signaling pathways have been extensively investigated, such as T cell activation signaling and co-regulatory signaling [36-42]. Harnessing the understanding of T cell signaling and the power of synthetic biology approaches, the immune-based cancer therapy, as the next generation therapeutic strategy, has already led to some success in clinical trials, such as chimeric antigen receptor (CAR) T-cell therapy for leukemia, and the blockade of immune checkpoints for several human tumors [35, 43-45].

Chapter 2: Development and Characterization of Src FRET Biosensors Based on High-Throughput Screening Platform

2.1. Abstract

Genetically encoded biosensors based on fluorescence/Förster resonance energy transfer (FRET) have enabled us to visualize and quantify a host of different molecular signaling events in single live cells with high-spatiotemporal resolutions. With more sensitive biosensors, it is envisioned that essentially every subtle signal can become observable. However, trial-and-error approaches based on rational assumptions to develop sensitive biosensors have low efficiency and low effectiveness. A systematic high-throughput platform based on yeast surface display and directed evolution was developed to identify interaction pairs with better binding affinity. I engineered Src FRET-based biosensors consisting of different identified Src Homolog 2 (SH2) variants and tyrosine peptides, and thoroughly examined the sensitivities and specificities of different Src biosensors in mammalian cells and *in vitro*. Comparing between the most current version of the Src biosensor and the parental Src biosensor, I showed the newly developed Src biosensor (SCAGE) got more than 40-fold improvement in sensitivities.

2.2. Introduction

Genetically encoded FRET-based biosensors are powerful tools for non-invasive visualization and quantification of intracellular signaling events with high spatio-temporal resolutions, especially in single live cells. In fact, numerous FRET biosensors have been developed and reported [11, 12, 46]. However, the empirical semi-rational design and labor-intensive optimization have hampered the development of highly

sensitive and specific biosensors. In particular, the rational design and engineering of proteins/biomolecules are hindered by our limitation in predicting 3D structure of molecules [47]. With the progress in random mutagenesis, directed evolution employing iterative cycles of mutagenesis and selection has become a powerful tool for protein engineering in cases where rational approaches are ineffective [3]. The current random-mutagenesis methods using error-prone PCR, site saturation mutagenesis, and DNA shuffling can easily generate libraries of millions of mutants [3]. The expression of these large libraries was made possible by the progress in yeast and bacterial display systems [5, 48-50]. Indeed, various scaffold systems have been developed to correctly and efficiently target different peptides/proteins at the outer surface of yeasts and bacteria [48, 49]. The fluorescence-activated cell sorting (FACS) technology based on flow cytometry can further enable the high throughput quantification, identification, and selection of desired proteins from these yeast/bacteria libraries [48]. While bacterial display provides the possibility of larger library size, yeast display is better for producing proteins compatible to mammalian cells because of its eukaryotic protein folding pathways and codon usage [51]. While directed evolution and FACS have been employed to develop fluorescent proteins (FPs) with novel fluorescent properties (color, brightness, photo-stability, or FRET efficiency), there is no general method available to systematically optimize the specificity and sensitivity of FRET biosensors. In this project, site-saturated-mutagenesis, yeast display, and FACS were integrated to systematically optimize FRET-based biosensors.

2.3. Materials and Methods

Constructions of DNA plasmids. The Src homolog 2 (SH2) binding domain was mutagenized using overlap extension saturation mutagenesis, using NNS degenerate codon as described previously [52] and the gene encoding the SH2 domain of *c-Src* as the PCR template. The mutagenized PCR product was cloned into pYD1 vector (Invitrogen Inc.) using *Sty*I and *Xho*I restriction sites.

The original cytosolic Src biosensor (Cyto-Src WT SH2 domain and EIYGEF) used in this study was developed by replacing the C-terminal EYFP of the Src biosensor [53] with YPet and keeping the N-terminal ECFP (enhanced CFP, truncated at the C terminus [54]). The site-directed mutagenesis was conducted using the QuikChange kit (Agilent Technologies Inc.)

The DNAs encoding the Src biosensors were subcloning with *Bam*HI and *Eco*RI restriction sites in pRSETB vector (Invitrogen Inc.) for the protein purification from *Escherichia coli*. The biosensor genes were further cloned with *Bam*HI and *Eco*RI restriction sites in pCDNA3.1 vector (Invitrogen Inc.) and *Eco*RI and *Sal*I restriction sites in customized pCAGGS vector [55, 56] for the protein expression in mammalian cells.

The plasmids used in this study include the constitutively active *c-Src* (active-Src) mutant, wild-type full-length *c-Src* (wt-Src), kinase-dead *c-Src* (ntv-Src) mutant in PMT2 vector, and wild-type full-length *c-Fyn* (wt-Fyn), wild-type full-length *c-Yes* (wt-Yes) in pCDNA 3.1 vector, and p^{CAG}LifeAct-TagRFP (ibidi Inc.). Empty pCDNA3.1 vector was used as a control plasmid. The *c-Src*, *c-Fyn*, *c-Yes*, and their mutants are previously described [24, 57], and their control vector pCDNA3.1 were described elsewhere [58, 59].

All the constructed DNA plasmids were analyzed and confirmed by restriction enzyme digestion and Sanger DNA sequencing (GENEWIZ Inc.).

Yeast transformation and induction. EBY100 (ATCC MYA-4941) was transformed using the LiAc/SS carrier DNA/PEG method as described previously [60], and plated onto the appropriate yeast synthetic drop-out (SD) agar plates with 2% glucose. Two days after transformation, colonies were picked into SD media with 2% glucose for culture. SD media with 2% galactose was used to induce surface display for protein production. A potential limitation of yeast display is that the yeast, a lower eukaryotic organism, may exhibit different codon usage and give different post-translational modification functions as comparing to mammalian cells. Thus, the binding pairs identified may not directly translate into optimal responses of biosensors in mammalian cells. This may partly explain why the CD/GE biosensor containing the strongest phospho-substrate binding domain SH2 C185D showed significantly lower sensitivity than the SCAGE biosensor in mammalian cells (Fig. 2.2.C).

Flow cytometry and FACS. Two days after induction, 2E6 cells were stained for display expression using 1:100 diluted V5 primary antibody (Invitrogen Inc., Catalog No. R960-25), 1:100 diluted goat anti-mouse biotin-conjugated secondary antibody (Sigma-Aldrich Inc., Catalog No. B7264), and 1:200 diluted R-Phycoerythrin (PE) conjugated with streptavidin (SA) (BD Biosciences, BD, Catalog No. 554061). For the examination of SH2 domain and its mutants, cells were stained for peptide affinity using various concentrations of biotin-conjugated peptide followed by 1:100 diluted SA-PE. All staining reagents were diluted at room temperature in a binding buffer (GE, 10 mM HEPES, pH 7.4, 150 mM NaCl, 3 mM EDTA, 0.005% Surfactant P20) containing 0.5%

BSA. Cells were also washed three times in binding buffer + 0.5% BSA before and after each staining step.

Cell sorting was carried out on a BD FACSAria II (BD Biosciences, BD) at UIUC Biotechnology Center. 1% of the most strongly fluorescent cells were sorted in the first round and 0.1% in the second round of sorting. After two rounds of sorting, cells were plated, and several colonies were picked for plasmid isolation and sequencing to identify the responsible mutations.

Cell culture, reagents and transient transfection. Cell lines, including mouse embryonic fibroblast (MEF), HeLa cells, adult male Potorous tridactylus kidney (PtK2) cells, and *Src*/*Fyn*/*Yes* triple knockout MEF (SYF -/-) cells, were from American Tissue Culture Collection (ATCC, Manassas, VA), with the authentication and the verification of the absence of mycoplasma contamination. These cells were cultured at ATCC recommended conditions in a humidified incubator with 5% CO_2 and 95% air at 37°C before experiment. All cells were maintained in Dulbecco's modified Eagle's (DMEM) supplemented with 10% fetal bovine serum (FBS), 2 mM·L-glutamine, 1 unit·ml^{-1} penicillin, 100 μg·ml^{-1} streptomycin, and 1 mM sodium pyruvate, except when indicated otherwise. Cell culture reagents were purchased from Life Technologies Inc. The DNA plasmids were transfected into the cells by using Lipofectamine 2000 or 3000 reagent (Invitrogen Inc.), according to the manufacturer's instructions. The SYF -/- cells were co-transfected with the Src FRET biosensor, and various Src family kinases or mutants to evaluate the biosensor specificity.

Fibronectin from bovine plasma (FN), human epidermal growth factor (EGF), rat recombinant platelet-derived growth factor BB (PDGF), cytochalasin D (CytoD) and

ML-7 were obtained from Sigma Aldrich Inc. Blebbistatin was not used since it has fluorescence which can interfere with the FRET signals [61, 62]. Collagen type-I from rat tail (Col I) was purchased from BD Biosciences, BD. The Src family kinase inhibitor PP1 was obtained from BioMol Inc.

Protein expression and purification, *in vitro* spectroscopy and kinase assays. The Src biosensors were in general expressed in *Escherichia coli* (BL21 strain) as fusion proteins with N-terminal 6xHis tag and purified by nickel chelation chromatography [24]. Fluorescence emission spectra of the purified biosensors were measured in a cuvette with an excitation wavelength of 437 nm by a fluorescence plate reader (infinite M1000 PRO, TECAN Inc.). The emission ratios of ECFP/YPet (476 nm/526 nm) were measured before and after adding 1 mM ATP (Promega Inc.) into the kinase assay buffer (50 mM Tris·HCl, 100 mM NaCl, 10 mM $MgCl_2$, 2 mM DTT, pH 8) at 37°C that contained a mixture of various biosensors and active human Src full-length protein (1 $\mu g \cdot ml^{-1}$, EMD Millipore Inc.) [24]. The purified biosensors were separated by 10% SDS-PAGE gels followed by Coomassie Blue staining. After destaining (50% v/v methanol in water with 10% acetic acid), the proteins were visualized, and the image was recorded by ChemiDoc MP imaging system with Image Lab software (Bio-Rad Inc.). The molecular weight of the Src biosensors is about 67 kDa.

FRET Microscopy, image acquisition and analysis. Cells were cultured for 36 hours in 0.5% FBS DMEM or 0% FBS Advanced medium, and plated on glass-bottom dishes (Cell E&G LLC) coated with Col I (50 $\mu g \cdot ml^{-1}$) or FN (2.5 $\mu g \cdot ml^{-1}$) for overnight prior to growth factor stimulation. During imaging process, cells were maintained in 0.5% FBS DMEM or 0% FBS Advanced medium at 37°C in a 5% CO_2 and 95% air-humidified

chamber. Images were collected by a Nikon Eclipse Ti inverted microscope equipped with a 300 W Xenon lamp (Atlas Specialty Lighting), an electron multiplying (EM) CCD camera (QuantEM:512SC, Photometrics) and a x100 DIC Nikon microscope objective (NA = 1.4) using MetaFluor 7.8.10.0 or MetaMorph 7.8.8.0 software (Molecular Devices, LLC) with a 420DF20 excitation filter, a 455DCXRU dichroic mirror, and two emission filters controlled by a filter changer (480DF40 for ECFP and 535DF25 YPet). All filters and dichroic mirrors were purchased from Chroma Technology Corp. The pixel-by-pixel ratio images of ECFP/FRET were calculated based on the background-subtracted fluorescence intensity images of ECFP and FRET using MetaFluor software. All the ratio images were displayed in the intensity-modified display mode [63] in which the color and brightness of each pixel were determined by the ECFP/FRET ratio and FRET intensity, respectively.

Statistical analysis. D'Agostino-Pearson omnibus normality test was used for the normality test. Data following Gaussian distribution were analyzed by using unpaired two-tailed Student's *t* test with Welch's correction or ordinary one-way ANOVA followed by Bonferroni's multiple comparisons test (Graphpad Prism 6, GraphPad Software) to evaluate the statistical difference between groups. Data not following Gaussian distribution were analyzed by using unpaired two-tailed Mann-Whitney test or Kruskal-Wallis test followed by Dunn's multiple comparison test (Graphpad Prism 6, GraphPad Software). A significant difference was determined by *P* value ($P < 0.05$). Statistical results are presented as mean ± S.E.M. Asterisks indicate critical values (*$P < 0.05$, **$P < 0.01$ and ***$P < 0.001$), and "n.s." indicates no significant difference ($P > 0.05$). All the experiments were replicated at least 3 times and represented biological replicates.

2.4. Results and Discussion

2.4.1. High-throughput screening of the substrate-binding affinity toward a library of *c-Src* SH2 domains

A yeast display system (Fig. 2.1.A) was developed to improve the binding between the SH2 domain and the substrate peptide within the Src FRET biosensor. This system allows a high-throughput screening and identification of optimal SH2 variants and corresponding peptide sequences (Fig. 2.1.A and Fig. 2.3). The staining of V5 epitope tag on the yeast surface confirmed the successful induction of the recombinant cargo proteins (Fig. 2.1.A and Fig. 2.4.A). The buffer conditions and the phosphopeptide concentrations were screened for the binding assay between the expressed SH2 domain and the phosphorylated substrate peptides. The results revealed that the binding buffer containing 0.5% BSA led to consistent staining signals (Fig. 2.4.B, C), which was applied for the binding buffers used in the rest of manuscript. As shown in Fig. 2.5, the substrate peptide conditions for yeast binding assays were also optimized. An ideal substrate sequence in a FRET biosensor should have two features: (1) the substrate sequence is favored by the target kinase for phosphorylation; (2) the substrate peptide upon phosphorylation has an optimal binding affinity toward the intramolecular SH2 domain (or its mutant) in the biosensor for FRET changes. It has been shown that EI**Y**GEF and EI**Y**EEF can serve as optimal substrate sequences for *c-Src* kinase *in vitro* [64], and a different sequence after phosphorylation p**Y**EEI is preferred for binding by the wild-type Src SH2 domain (WT SH2) [65]. Hence, these different phosphopeptides (pYGEF, pYEEF, and pYEEI) as well as the unphosphorylatable negative control after removing the tyrosine residue (FEEI) were compared, with respect to their binding toward WT SH2. The yeast cells displaying

WT SH2 were stained using these peptides. The results indicate that both pYGEF and pYEEF can bind to WT SH2 proportional to the peptide concentration, with pYEEF clearly demonstrating a stronger binding than the previously identified pYEEI [65] (Fig. 2.5.A-C). pYEEF and pYGEF peptides as the Src favorable substrate sequences (0.2 μg/μl, pYGEF<pYEEI<pYEEF in binding toward WT SH2 as shown in Fig. 2.5.A-C) were subsequently utilized to conduct the binding assay against the yeast cells displaying either WT SH2 or its mutant library. The mutant library was generated by site-saturation mutagenesis [52] on the cysteine site (C185) in WT SH2 which is critical for the binding pocket of phosphotyrosine peptides [66]. Compared to yeast cells uniformly expressing WT SH2, the yeast library displaying diversified mutants showed overall stronger binding toward both pYGEF and pYEEF peptides (Fig. 2.1.B, C). Stronger binding of both WT SH2 and the mutant library toward pYEEF over pYGEF were observed (Fig. 2.1.B, C). The yeast cells displaying SH2 mutants with strong binding toward phosphotyrosine peptides (pYEEF and pYGEF) were enriched by sorting and repopulating (Fig. 2.1.B, C). Among the sorted SH2 variants, C185D, C185R, C185T, C185V, and C185A mutations were identified by sequencing and verified by yeast staining to show high binding toward the phosphotyrosine peptides, with pYEEF displaying a significantly higher binding capacity than pYGEF toward each mutant (Fig. 2.1.D and Fig. 2.6). The results suggest that yeast display and random mutagenesis can allow the high-throughput screening and identification of efficient interaction pairs consisting of SH2 mutants and phosphotyrosine peptides. This approach is potentially applicable to the engineering of, in principle, any sensitive FRET biosensor capable of monitoring tyrosine kinase activities.

2.4.2. Characterization of Src biosensors with identified mutations in live mammalian cells

I then constructed FRET-based Src biosensors comprising identified binding pairs of substrates and SH2 mutants, with the expectation that the substrate phosphorylation by Src kinase can cause a conformational change and a reduction of FRET efficiency due to the consequent separation of YPet from ECFP (Fig. 2.7). I replaced EYFP in the original Src biosensor [53] with YPet because YPet has been verified to form a better FRET pair with ECFP in enhancing the sensitivities of biosensors [67]. I examined the sensitivities and specificities of these Src biosensors in mammalian cells and compared them with the parental biosensor [53] used as the template for directed evolution. In HeLa cells expressing different Src biosensors, epidermal growth factor (EGF) induced a large FRET response (~156%) in the SCAGE group (SH2 C185A and substrate EIYEEF, with C->A mutation in residue 185 of WT SH2 and G->E mutation in the substrate, Fig. 2.2.A-C). Smaller FRET responses were observed in other groups, either the Ori group (WT SH2 and EIYGEF, Fig. 2.2.A-C) or groups with a single mutation at the SH2 and/or substrate regions (Fig. 2.2.B, C). I further incorporated additional mutations revealed by our earlier publication [68] in improving the binding affinity of SH2 domain toward phosphotyrosine peptides into the SH2 domain of the SCAGE biosensor and examined their effects. The results indicate that these two additional mutations (SH2 T180V and/or K203L) failed to further improve the biosensor sensitivities (Fig. 2.2.C). In fact, the CA/GE/TV/KL (incorporating triple point mutations SH2 C185A, T180V, K203L with substrate EIYEEF) group gave a much smaller FRET response (~26.5%, Fig. 2.2.C), suggesting that overly high affinity between binding pairs within the biosensor may not

necessarily enhance the biosensor sensitivity. I further examined the platelet-derived growth factor (PDGF)-induced FRET responses of the Ori, CA, GE and SCAGE biosensors in mouse embryonic fibroblasts (MEFs) (Fig. 2.8). Again, the largest FRET response (~108%, Fig. 2.8.C) was observed in the SCAGE group, with 15%-20% ratio changes for the CA or GE only group and ~5.4% ratio change for the Ori group (Fig. 2.8.C). The biosensors in HeLa cells and MEFs had very distinct dynamics (Fig. 2.2.B and Fig. 2.8.B), with a clear transient time course in HeLa cells but a sustained activity in MEFs as particularly highlighted by SCAGE. In HeLa cells expressing SCAGE, EGF-induced FRET response was substantially reduced after pretreatment with PP1, a selective Src family inhibitor (Fig. 2.2.C). To further determine the specificity of SCAGE, I reconstituted *Src*/*Yes*/*Fyn* triple-knockout (SYF -/-) MEFs with active-Src, wt-Src (wild-type *c-Src*), ntv-Src (kinase-dead *c-Src*), wt-Fyn, wt-Yes or an empty vector. Only active-Src and wt-Src restored the ECFP/FRET ratios (Fig. 2.2.D). These results suggest that the new SCAGE biosensor can specifically detect Src kinase activity. FRET response was absent in HeLa cells expressing the inactive CA/GE/YF (SH2 C185A and EIFEEF, Fig. 2.2.C) biosensor in which the substrate tyrosine is mutated to phenylalanine. Therefore, the biosensor response requires the tyrosine phosphorylation of the substrate as designed (Fig. 2.7.B). I further compared this SCAGE biosensor in HeLa cells with our previously developed Src biosensor (WME biosensor) [67] which has a high sensitivity but contains two tyrosine residues in the substrate. In HeLa cells, the SCAGE biosensor showed a significantly higher sensitivity than the WME biosensor (Fig. 2.9). These results indicate that the interaction pairs identified from the high-

throughput screening of libraries successfully enhanced the sensitivities of FRET biosensors.

2.4.3. Characterization of the identified Src biosensors *in vitro*

I furthermore characterized the purified Src biosensor proteins to verify the sensitivities of these different biosensors in solution without the interference of unpredictable co-factors in cellular environment. Fig. 2.10 summarizes the biosensor sensitivity *in vitro* as indicated. After being phosphorylated by the active Src kinase *in vitro*, the SCAGE biosensor had a ~164% change (Fig. 2.10). The Ori, CD, and CD/GE biosensors, on the other hand, showed significantly lower levels of FRET responses (Fig. 2.10). As controls, only minor FRET responses in both the CA/GE/RV and CA/GE/YF biosensors were observed (Fig. 2.11), suggesting that the biosensor response *in vitro* is governed by the intramolecular interaction between the SH2 domain and the substrate peptide as designed [24, 69] (Fig. 2.7.B). Again, the CA and GE groups had significantly larger FRET responses than the Ori group *in vitro* (Fig. 2.10.A, B, H), verifying the beneficial roles of these mutations for the biosensor sensitivities. Based on the above observations, I determined that the sensitivity of the new SCAGE biosensor was about ten times as sensitive as the parental Ori biosensor *in vitro* (Fig. 2.10.H).

2.5. Conclusion

A high-throughput screening method has been developed (Fig. 2.3) that allows the systematic development of FRET biosensors (Fig. 2.7.A). The result is a highly sensitive Src biosensor (SCAGE), which provides a more than 40-fold sensitivity enhancement in live mammalian cells comparing to the parental biosensor template before the directed-evolution-based improvement [53] (Fig. 2.2.C). This new Src biosensor is also more

sensitive than our previously developed Src biosensor based on a rational design with two tyrosine residues in the substrate motif [67] (Fig. 2.9). As such, the high throughput screening method can be applied to systematically develop highly sensitive FRET biosensors for visualizing and quantifying molecular signaling events.

The development of intramolecular FRET biosensors generally suffers from low-throughput optimizations in trial-and-error fashions. The high-throughput screening method provides a new way for development of sensitive FRET biosensors in a systematic fashion. This high-throughput screening platform based on yeast display and directed evolution has a number of advantages. First, upon induction, the yeast display system can correctly express the protein cargo motifs on the yeast surface, readily and specifically accessible by binding partners to be screened (Fig. 2.4.A). In fact, negative control peptide FEEI showed no significant binding to WT SH2 displayed on the yeast surface even at a high concentration. Second, this method allows for effective screening and identification of various interaction pairs with better binding affinities, including but not limited to substrate peptides and SH2 domain variants. This method can hence be readily extended to develop, in principle, any post-translational modification FRET biosensor (*i.e.*, for an enzyme). A limitation of the approach is that the yeast, a lower eukaryotic organism, exhibits different codon usage and gives different post-translational modification functions as comparing to mammalian cells. Thus, the binding pairs identified may not directly translate into optimal responses of biosensors in mammalian cells. This may explain why the CD/GE biosensor containing the strongest phospho-substrate binding domain SH2 C185D showed significantly lower sensitivity than the SCAGE biosensor in mammalian cells (Fig. 2.2.C).

Furthermore, the biosensor characterization in mammalian cells revealed very distinct dynamics and responses of the SCAGE biosensor. In fact, the characterization in mammalian cells revealed that the SCAGE biosensor showed a transient FRET response upon EGF stimulation in HeLa cells (Fig. 2.2.B), but a markedly sustained FRET response upon PDGF stimulation in MEFs (Fig. 2.8.B). It is possible that EGF and PDGF receptors involve distinct regulations, such as downregulation of kinase activation and endocytic trafficking of receptor tyrosine kinases [70-73]. For instance, EGFR in HeLa cells, but not PDGFR in MEFs, may undergo fast ubiquitination, degradation or internalization, which could contribute to the transient nature of EGFR signaling. Hence, the high-sensitivity Src biosensor may be applied to reveal the dynamic differences between EGF and PDGF-mediated signaling transductions and shed new lights on the molecular mechanisms underlying their distinct regulations.

2.6. Figures

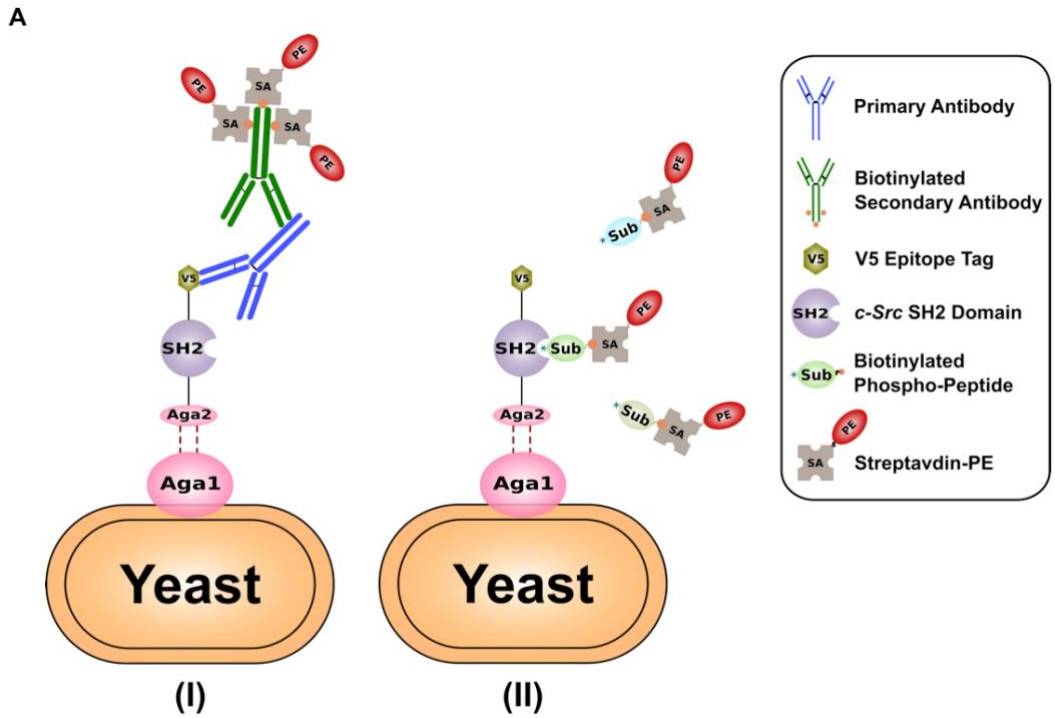

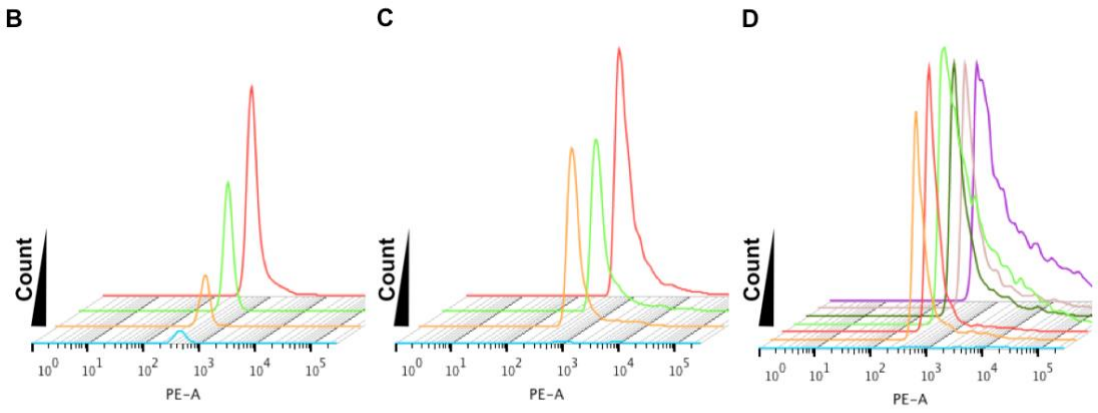

Group	Freq. of Parent
Sorted YGEF	1.343%
Lib. YGEF	0.679%
Ind. YGEF	0.323%
Non-Ind. YGEF	0.0981%

Group	Freq. of Parent
Sorted YEEF	8.557%
Lib. YEEF	5.374%
Ind. YEEF	5.361%
Non-Ind. YEEF	0.225%

Group	Freq. of Parent
C185V YEEF	19.29%
C185T YEEF	12.20%
C185R YEEF	12.31%
C185D YEEF	27.08%
C185A YEEF	10.86%
WT YEEF	9.332%
Non-Ind. YEEF	0.431%

Figure 2.1: The optimal *c-Src* SH2 domain variants and tyrosine kinase substrates identified by high-throughput screening.

(**A**) The SH2 domains from *c-Src* kinase are displayed on the yeast cell surface as a fusion protein carrying the V5 epitope tag at the C-terminus. (I): The V5 epitope tag

Figure 2.1: The optimal *c-Src* SH2 domain variants and tyrosine kinase substrates identified by high-throughput screening, Continued

allows the staining of expressed protein cargoes by the primary antibody and the biotinylated secondary antibody, which can then be labeled by streptavidin-R-phycoerythrin (SA-PE) conjugate. (II): Wild-type SH2 domain (WT) and variant SH2 domain mutants bind to the biotinylated phosphotyrosine-containing substrate peptides, which can then be labeled by SA-PE conjugate. (**B-D**) Identifying the optimal SH2 domain mutants and the corresponding substrate peptides, with phosphorylated peptides EIpYGEF in (**B**), EIpYEEF in (**C**), and EIpYEEF together with different SH2 domain variants (C185A, C185D, C185R, C185T and C185V) as indicated in (**D**). "Non-ind.", "Ind." and "Lib." represent non-induced yeast group, induced yeast group and yeast library group, respectively, stained with phosphorylated peptide EIpYGEF or EIpYEEF. C185A, C185D, C185R, C185T and C185V are different mutations in residue 185 of wild-type *c-Src* SH2 domain.

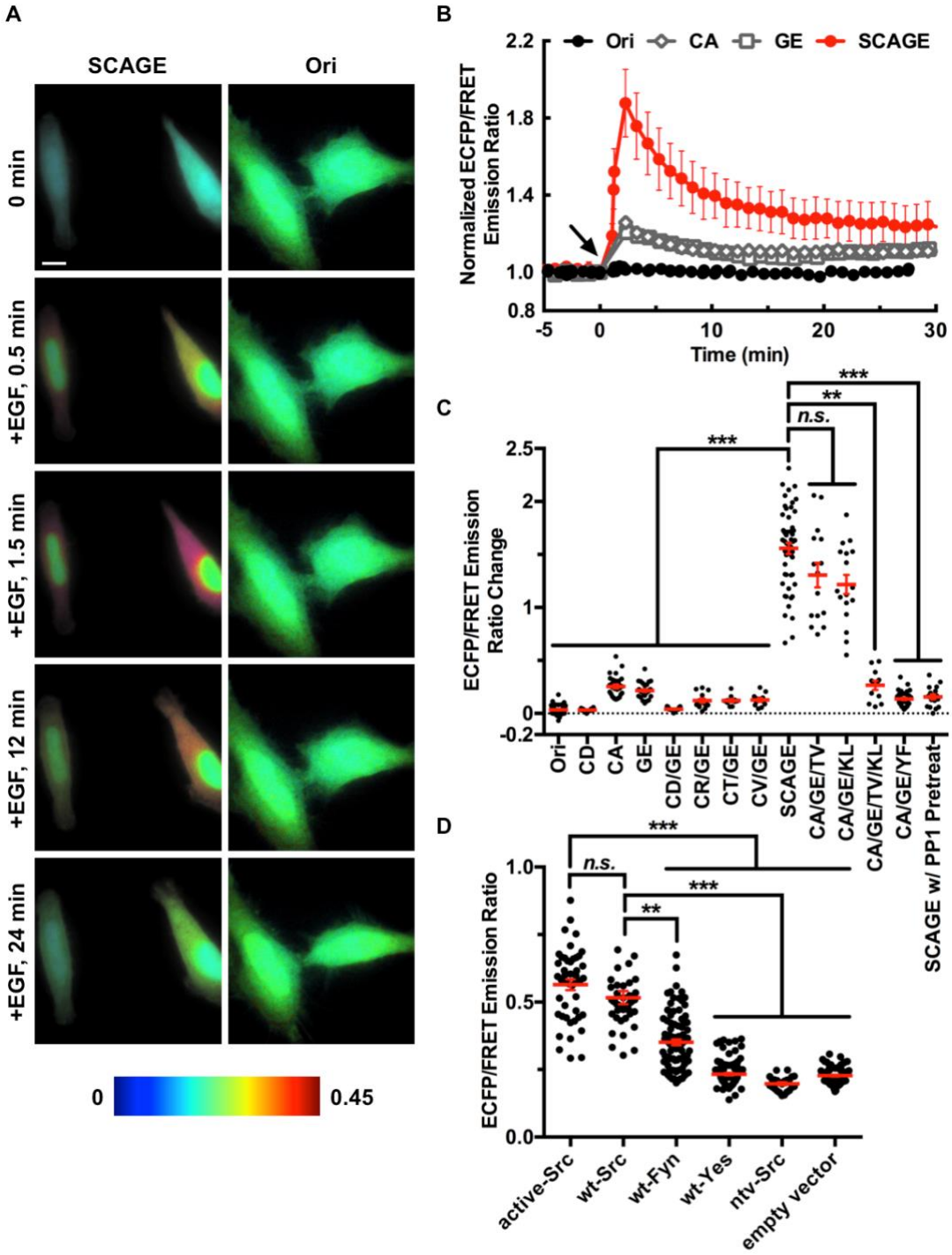

Figure 2.2: Characterization of FRET-based Src biosensors in living mammalian cells.

(**A**) Time-lapse FRET imaging in HeLa cells expressing Src FRET biosensors (SCAGE or Ori) with 50 ng/mL EGF stimulation. ECFP/FRET ratio images of HeLa cells expressing SCAGE biosensor or Ori biosensor at the indicated time points are shown in intensity-modulated display mode. The color scale bar at the bottom shows the range of

Figure 2.2: Characterization of FRET-based Src biosensors in living mammalian cells, Continued

ECFP/FRET emission ratio, with cool and warm colors representing low and high ratios, respectively. Scale bars, 5 μm. (**B**) The time courses of normalized average ECFP/FRET emission ratios of the Ori (black solid circles, n = 6), CA (open diamonds, n = 7), GE (open squares, n = 8), and SCAGE (red solid circles, n = 5) biosensors in HeLa cells before and after 50 ng/mL EGF stimulation (arrow at 0 min). ECFP/FRET emission ratios are normalized against the average values before EGF stimulation. The error bars represent the standard error of the mean (S.E.M.). Average data are presented as mean ± S.E.M. (**C**) The responses of different Src FRET biosensors in HeLa cells stimulated with 50 ng/mL EGF. CA/GE/YF group is the inactive control group and SCAGE w/ PP1 Pretreat group is the SCAGE biosensor group pretreated with 10 μM PP1 for 1 hr (n = 53, 18, 28, 30, 17, 13, 10, 12, 52, 15, 17, 12, 36 and 17 cells for Ori, CD, CA, GE, CD/GE, CR/GE, CT/GE, CV/GE, SCAGE, CA/GE/TV, CA/GE/KL, CA/GE/TV/KL, CA/GE/YF and SCAGE w/ PP1 Pretreat groups, respectively). (**D**) The ECFP/FRET emission ratios of the SCAGE biosensor in *Src*/*Yes*/*Fyn* triple-knockout (SYF -/-) mouse embryonic fibroblasts (MEFs) co-transfected with various Src family kinases or mutant or an empty vector. SYF -/- MEFs are reconstituted with active-Src (n = 46), wt-Src (wild-type *c-Src*, n = 44), ntv-Src (kinase-dead *c-Src*, n = 24), wt-Fyn (n = 90), wt-Yes (n = 107) or an empty vector (n = 81). (**C-D**) In scatter plots, the red lines indicate the mean values, the error bars represent S.E.M. and average data are presented as mean ± S.E.M. *** ($P < 0.001$), ** ($P < 0.01$), n.s. ($P > 0.05$) are from Kruskal-Wallis test followed by Dunn's multiple comparison test.

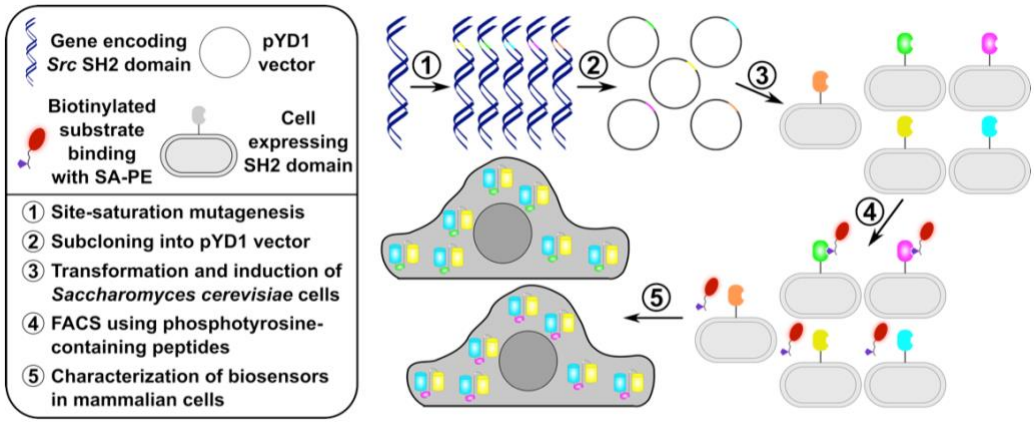

Figure 2.3: System schematic of high-throughput screening for FRET-based biosensors.

Schematics include the generation of a SH2 domain mutant cDNA library by (1) site-saturation mutagenesis, (2) subcloning into pYD1 vector, (3) library transformation into *S. cerevisiae* cells and induction of surface-displayed proteins, (4) binding affinity screening of SH2 domains against different substrate peptides (including EIpYGEF, EIpYEEF, EIpYEEI and EIFEEI), and (5) detailed characterization of Src FRET-based biosensors containing selected SH2 domain variants and substrates in live mammalian cells.

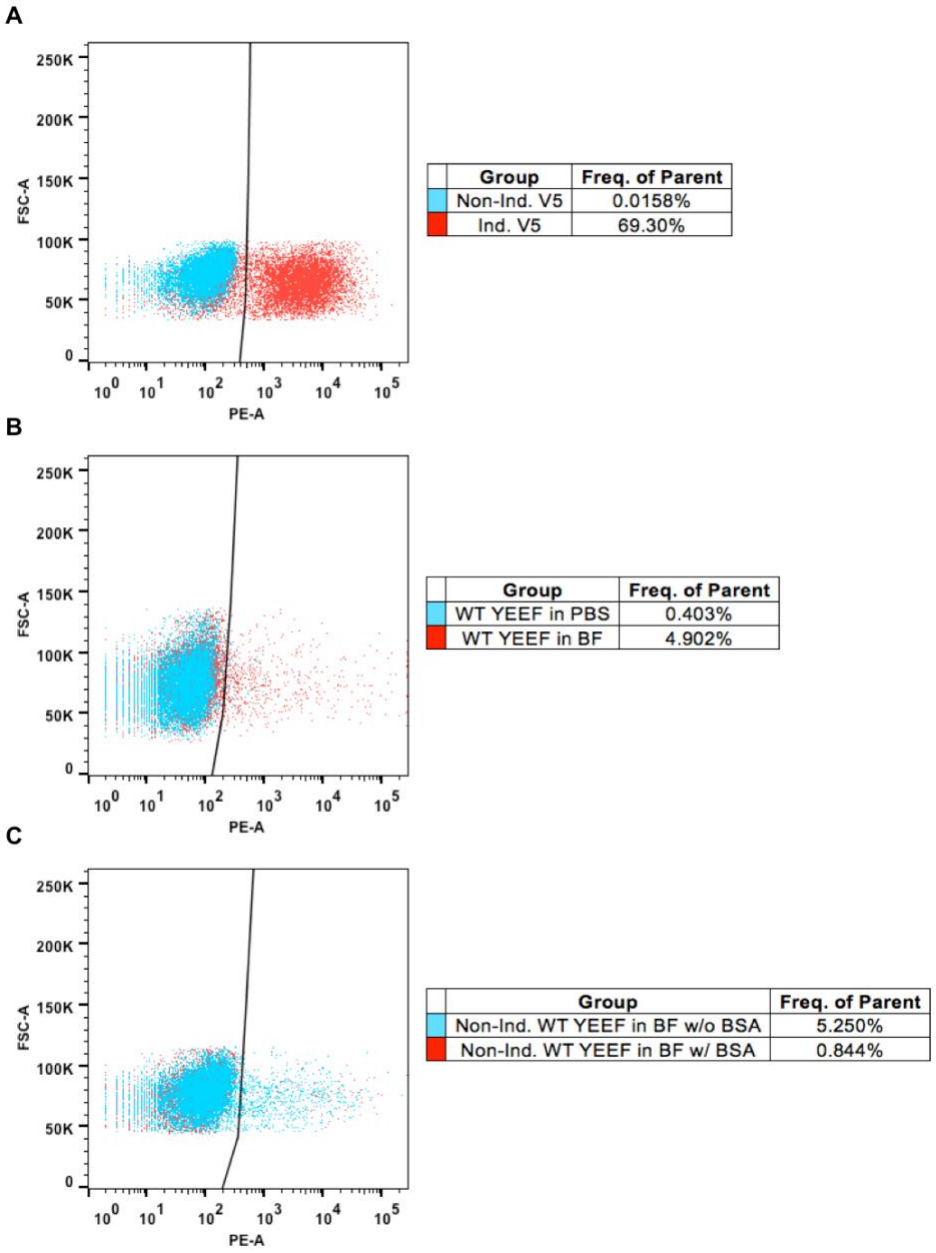

Figure 2.4: Optimizing conditions and validating protein expression for the yeast display system.

(**A**) Flow cytometry data of induced and non-induced yeast cells stained with the anti-V5 antibody. The staining of the yeast surface confirmed the successful induction of the recombinant proteins carrying the V5 epitope tag at the C-terminus (0.0158% and 69.30% staining for non-induced and induced groups, respectively). (**B**) Flow cytometry data of yeast surface displaying the wild-type SH2 domain (WT) for binding to the EIpYEEF phosphopeptide under different buffer conditions. The binding buffer (BF) yielded better staining of the yeast surface than the PBS solution (4.902% in BF and 0.403% in PBS). (**C**) Flow cytometry data of non-induced yeast cells transformed with

Figure 2.4: Optimizing conditions and validating protein expression for the yeast display system, Continued

WT and stained with the EIpYEEF phosphopeptide under different binding buffer conditions. The staining done in the binding buffer without BSA rendered higher background noise than the binding buffer with 0.5% BSA (5.250% in BF without BSA and 0.844% in BF with 0.5% BSA). (**A-C**)"Non-ind." and "Ind." represent non-induced and induced yeast groups, respectively, stained with anti-V5 antibody or EIpYEEF.

A

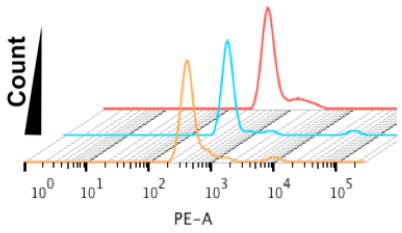

Group	Freq. of Parent
WT YGEF 0.02 µg/µL	0.0849%
WT YGEF 0.1 µg/µL	0.0681%
WT YGEF 0.2 µg/µL	0.0846%

B

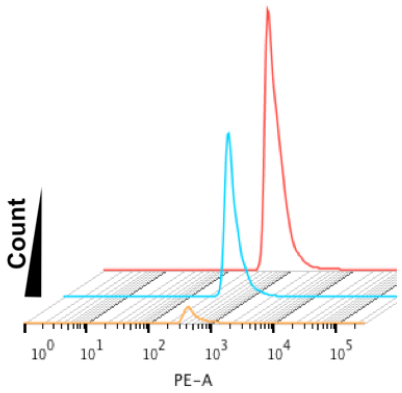

Group	Freq. of Parent
WT YEEF 0.02 µg/µL	0.519%
WT YEEF 0.1 µg/µL	4.436%
WT YEEF 0.2 µg/µL	8.259%

C

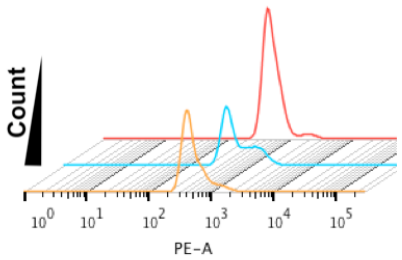

Group	Freq. of Parent
WT YEEI 0.02 µg/µL	0.130%
WT YEEI 0.1 µg/µL	0.119%
WT YEEI 0.2 µg/µL	0.208%

D

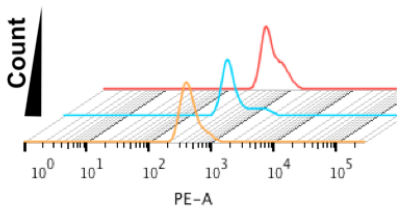

Group	Freq. of Parent
WT FEEI 0.02 µg/µL	0.0553%
WT FEEI 0.1 µg/µL	0.0515%
WT FEEI 0.2 µg/µL	0.0609%

Figure 2.5: Optimizing substrate peptides for the yeast display system.

Figure 2.5: Optimizing substrate peptides for the yeast display system, Continued

(**A-D**) Flow cytometry results of yeast surface displaying the WT SH2 domain binding to different phosphopeptides. **A**, Flow cytometry data of yeast surface displaying the wild-type SH2 domain (WT) binding to the EIpYGEF phosphopeptide of different concentrations (0.02 μg/μl: 0.0849%, 0.1 μg/μl: 0.0681%, 0.2 μg/μl: 0.0846%). **B**, Flow cytometry data of yeast surface displaying WT binding to the EIpYEEF phosphopeptide of different concentrations (0.02 μg/μl: 0.519%, 0.1 μg/μl: 4.436%, 0.2 μg/μl: 8.259%). **C**, Flow cytometry data of yeast surface displaying WT binding to the EIpYEEI phosphopeptide of different concentrations (0.02 μg/μl: 0.130%, 0.1 μg/μl: 0.119%, 0.2 μg/μl: 0.208%). **D**, Flow cytometry data of yeast surface displaying WT binding to the negative control peptide EIFEEI of different concentrations (0.02 μg/μl: 0.0553%, 0.1 μg/μl: 0.0515%, 0.2 μg/μl: 0.0609%).

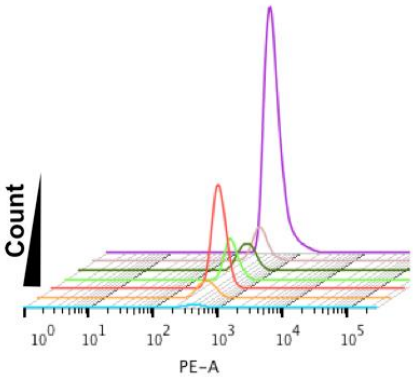

	Group	Freq. of Parent
	C185V YGEF	1.316%
	C185T YGEF	0.217%
	C185R YGEF	0.210%
	C185D YGEF	0.253%
	C185A YGEF	0.600%
	WT YGEF	0.142%
	Non-Ind. YGEF	0.0318%

Figure 2.6: Flow cytometry result of yeast surface displaying different SH2 domains against the EIpYGEF phosphopeptide.

The non-induced yeast cells (0.0318%) and induced yeast cells displaying different SH2 domain variants (WT: 0.142%, C185A: 0.600%, C185D: 0.253%, C185R: 0.210%, C185T: 0.217%, C185V: 1.316%) were stained with the EIpYGEF phosphopeptide. "Non-ind.", "Ind." and "Lib." represent non-induced yeast group, induced yeast group and yeast library group, respectively, stained with phosphorylated peptide EIpYGEF or EIpYEEF. C185A, C185D, C185R, C185T and C185V are different mutations in residue 185 of wild-type *c-Src* SH2 domain.

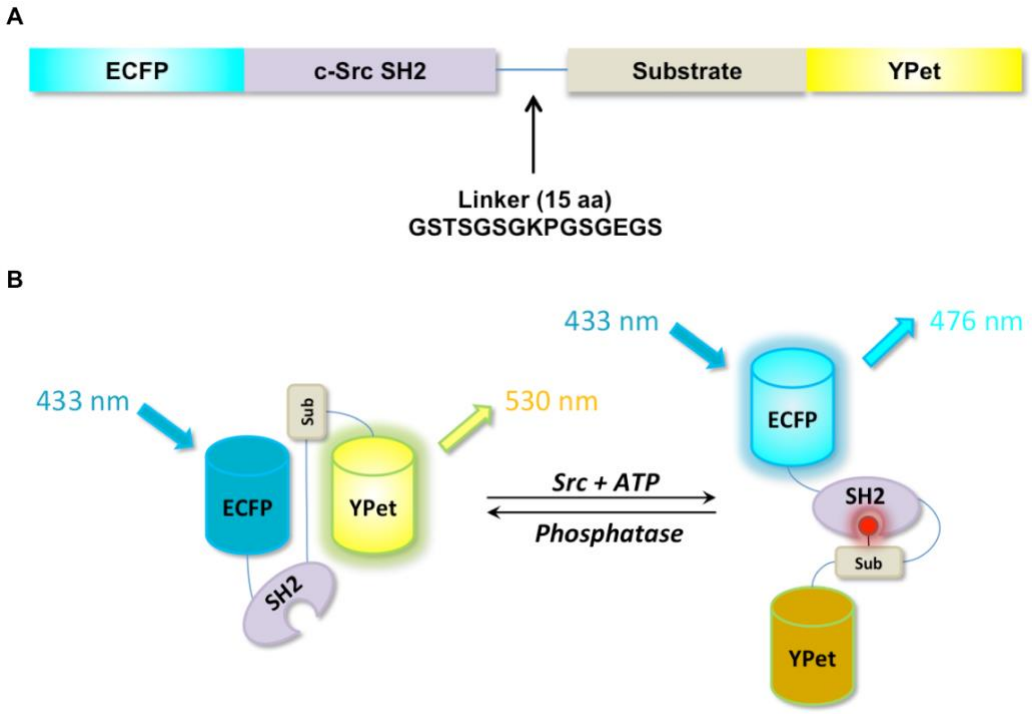

Figure 2.7: The design of the FRET-based Src biosensor.

(**A**) The FRET-based Src biosensor is composed of ECFP, the *c-Src* SH2 domain, a flexible linker (15 amino acids), the substrate peptide for the Src kinase and YPet. (**B**) Schematic representation of the principle of the FRET-based Src biosensor response. The active Src kinase can phosphorylate the substrate peptide in the Src biosensor, which subsequently binds to the intramolecular SH2 domain to cause the conformational change and reduce the FRET efficiency. Dephosphorylation by protein phosphatases reverses the process.

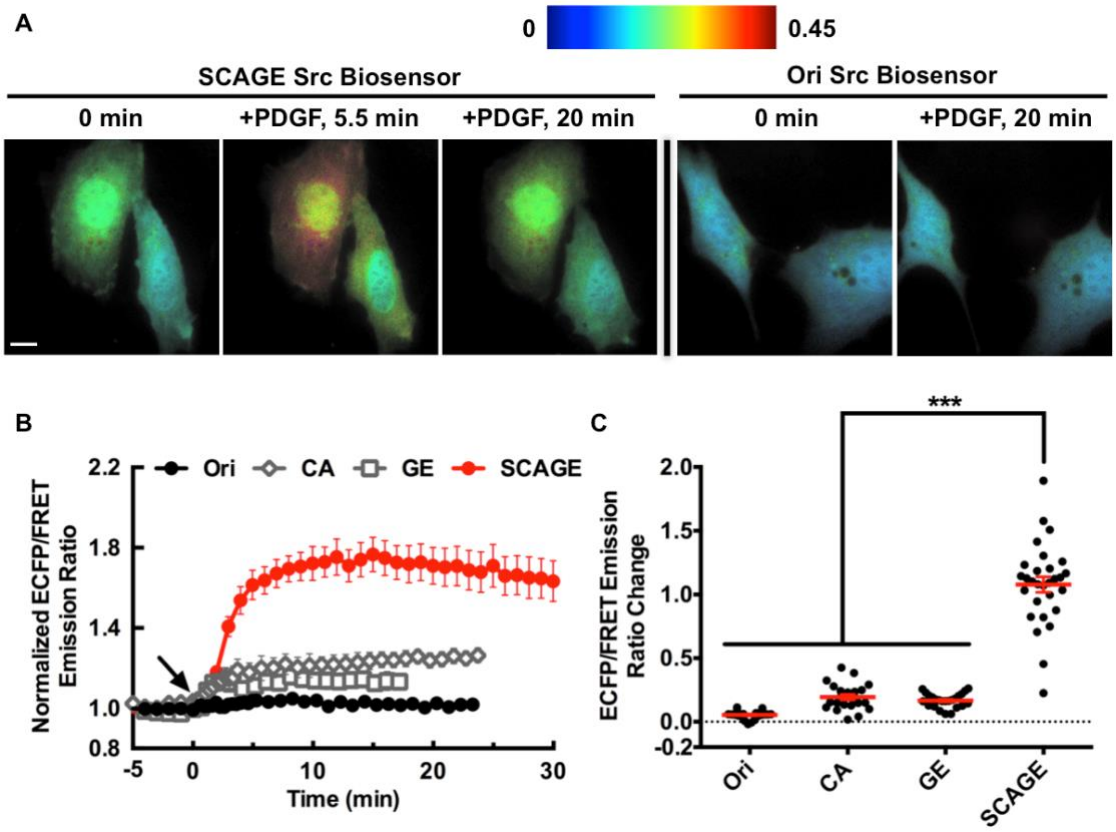

Figure 2.8: Characterization of FRET-based Src biosensors in mouse embryonic fibroblast cells.

(**A**) Time-lapse FRET imaging in mouse embryonic fibroblasts (MEFs) expressing different Src biosensors (SCAGE or Ori) with 50 ng/mL PDGF stimulation. ECPF/FRET ratio images of MEF cells expressing the SCAGE biosensor or Ori biosensor at the indicated time points are shown in intensity-modulated display mode. The color scale bar at the top shows the range of ECFP/FRET emission ratio, with cool and warm colors representing low and high ratios, respectively. Scale bars, 5 μm. (**B**) The time courses of normalized average ECFP/FRET emission ratios of the Ori (black solid circles, n = 4), CA (open diamonds, n = 3), GE (open squares, n = 3), and SCAGE (red solid circles, n = 6) biosensors in MEFs before and after 50 ng/mL PDGF stimulation (arrow at 0 min). The ECFP/FRET emission ratios are normalized against the average values before PDGF stimulation. The error bars represent the standard error of the mean (S.E.M.). Average data are presented as mean ± S.E.M. (**C**) The responses of different Src FRET biosensors in MEFs stimulated with 50 ng/mL PDGF. n = 20, 22, 24 and 29 cells for Ori, CA, GE and SCAGE, respectively. The red lines indicate the mean values, the error bars represent S.E.M. and average data are presented as mean ± S.E.M. *** ($P < 0.001$) is from ordinary one-way ANOVA followed by Bonferroni's multiple comparison test.

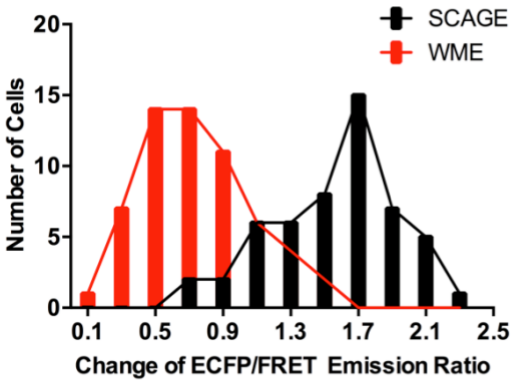

FRET Responses in HeLa Cells	SCAGE	WME
Avg.	1.5575988	0.747868
STD	0.3768386	0.324939
P-Value of T-Test	4.987E-21	

Figure 2.9: Histogram of the sensitivities of different FRET-based Src biosensors.

Histogram comparison between the sensitivities of Src SCAGE biosensor (black column, n = 52) and Src WME biosensor (red column, n = 59) in HeLa cells. P value ($P < 0.05$) represents the significant difference between two groups based on the unpaired two-tailed Student's *t* test with Welch's correction.

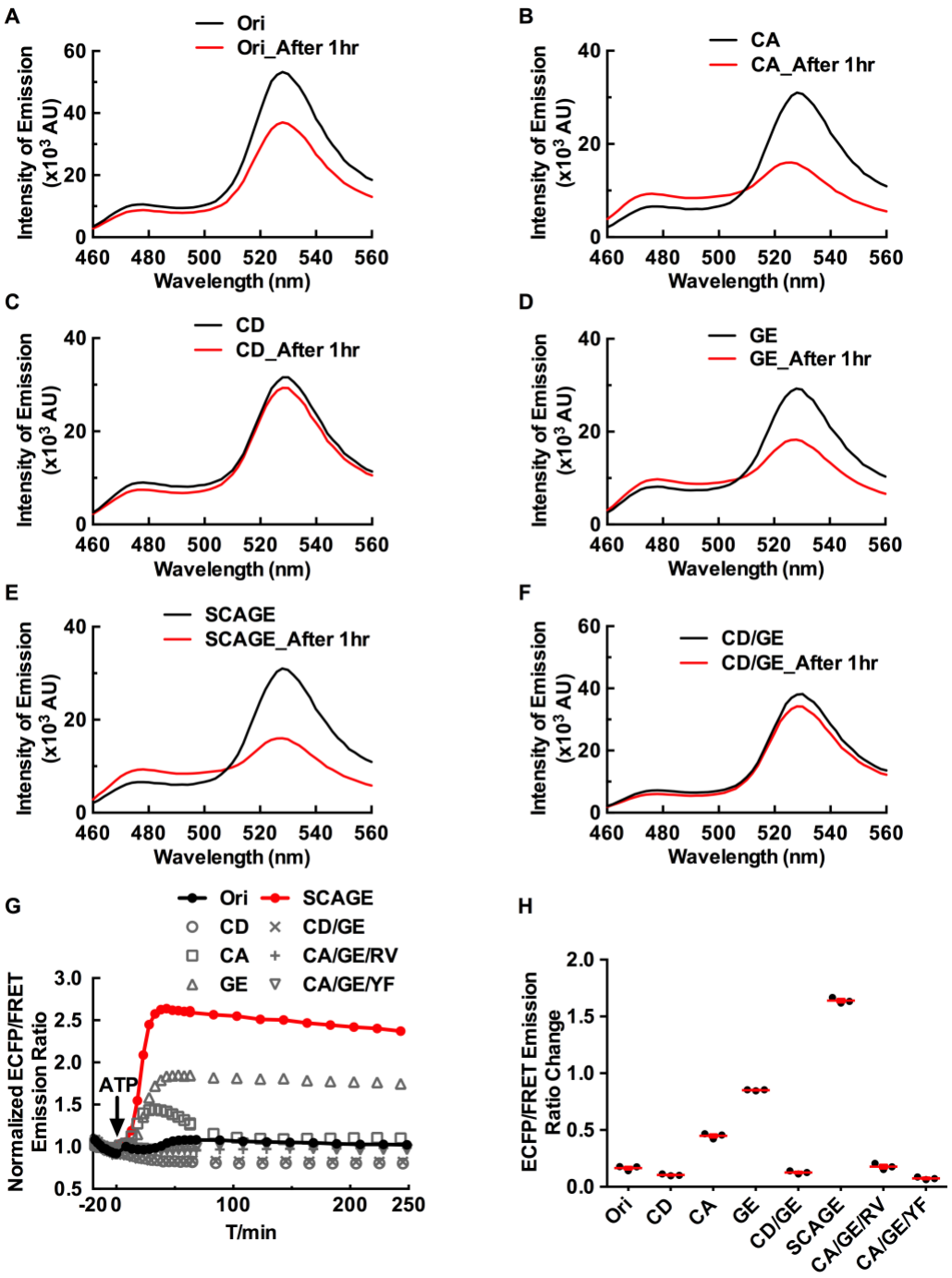

Figure 2.10: Characterization of FRET-based Src biosensors *in vitro*.

(**A-F**) Emission spectra of different Src biosensors (Ori, CA, CD, GE, SCAGE and CD/GE biosensors) before (black line) and after (red line) phosphorylation by the Src kinase for 1 hour. (**G**) The time courses of normalized average ECFP/FRET emission ratios of different Src biosensors (n=3 for Ori, CD, CA, GE, CD/GE, SCAGE, CA/GE/RV and CA/GE/YF biosensors, 1 μM) before and after phosphorylation by the Src kinase *in vitro* (arrow at 0 min with ATP addition). ECFP/FRET emission ratios are

Figure 2.10: Characterization of FRET-based Src biosensors *in vitro*, Continued

normalized against the average values before the Src kinase was added. (**H**). The ECFP/FRET emission ratio changes of different Src biosensors in response to the Src kinase *in vitro*. The red lines indicate the mean values, the error bars represent S.E.M. and average data are presented as mean ± S.E.M. (n = 3 for all groups).

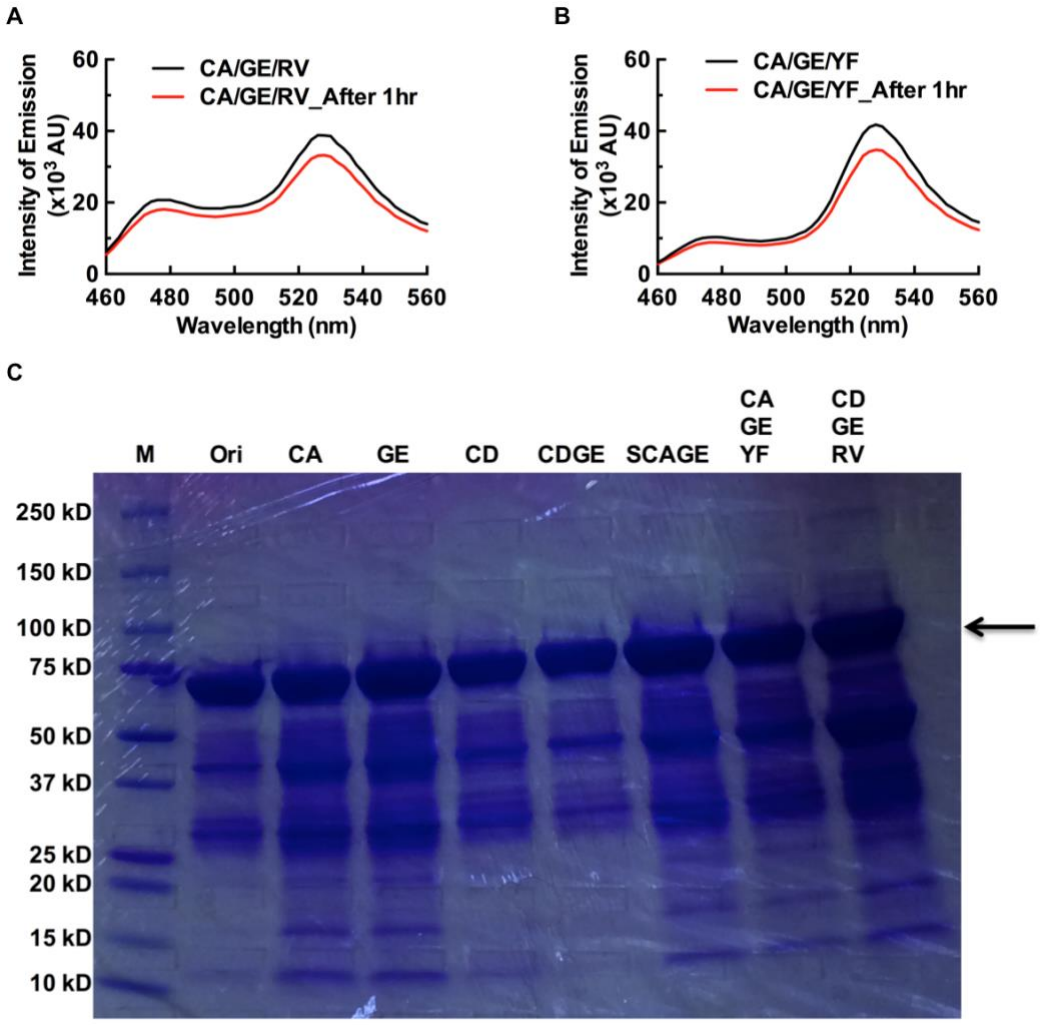

Figure 2.11: Characterization of the inactive FRET-based Src biosensors *in vitro* and confirmation of purified Src biosensors.

(**A-B**) Emission spectra of the inactive Src biosensors (CA/GE/RV and CA/GE/YF biosensors, 1 μM) before (black line) and after (red line) the phosphorylation by the Src kinase for 1 hr. (**C**) Confirmation of purified Src biosensors by Coomassie blue staining of polyacrylamide gel. The expected size of Src biosensors is approximately 75 kD (black arrow). M: the protein molecular-weight marker, Ori: the Ori Src biosensor, CA: the CA Src biosensor, GE: the GE Src biosensor, CD: the CD Src biosensor, CDGE: the CD/GE Src biosensor, SCAGE: the SCAGE Src biosensor, CAGEYF: the CA/GE/YF Src biosensor, CAGERV: the CA/GE/RV Src biosensor.

Chapter 3: Visualizing Spatiotemporal Dynamics of Intercellular Signaling Transmission by An Integrated Photonic Approach

3.1. Abstract

Cell-to-cell communications of physical and mechanical cues are essential for information exchange and functional coordination between cells, especially in multicellular organisms. However, it remains challenging to visualize intercellular signaling dynamics in single live cells. Here, I report a photonic approach, based on robotic laser micro-scissors and fluorescence/Förster resonance energy transfer (FRET) microscopy, to study signaling transmission between adjacent cells. A highly sensitive FRET-based biosensor (SCAGE) for Src kinase, a key regulator of intercellular interactions and signaling cascades, was developed by the high-throughput screening platform described in chapter 2. SCAGE enables the visualization of a transient Src activation across neighboring cells upon local physical perturbations by femtosecond laser pulses, which depends on passive cytoskeletal structure but not active actomyosin contractility. The integrated approach could be broadly applied to introduce local physical perturbations and directly visualize the spatiotemporal dynamics and transmission of ensuing signaling events. This integrated approach will advance our in-depth understanding of the molecular mechanisms underlying the physical-biochemical basis of cellular coupling.

3.2. Introduction

Cell-to-cell communications in multicellular organisms are fundamentally pivotal to their differentiation and development [74-76]. Accurate control of a sophisticated repertoire of signals enables properly exchanging information and coordinating functions and behaviors between cells [74, 77]. Cadherin-mediated cell-cell adhesions are commonly believed to be involved into these well-orchestrated processes. For example, expression of cadherins is tightly regulated during embryonic development and adult tissue homeostasis and remodeling, and correlates with a variety of morphogenetic processes, such as cell sorting, cell rearrangements and cell movements [20, 78]. Cadherins form physical and functional linkages with different cytoplasmic filaments and serve as a scaffold to mediate mechanical and biochemical signaling transductions [21, 79-82]. The perturbation of cadherin expression or function was also found to be associated with cancer progression, such as tumor invasion and metastasis [81, 83]. Moreover, decades of research have revealed multiple mechanisms that underlie the regulation of cadherin-mediated cell-cell contacts [20, 84, 85]. In particular, a wide variety of tyrosine kinases contributes in mediating cadherin-based adhesions, including both receptor and non-receptor protein kinases [84-86]. Among those, Src family kinases (SFKs) are critical regulators of adhesion-associated signals [29, 87]. SFKs have been shown to be concentrated at adherens junctions and correlate with elevated phosphorylation levels of adhesion complex proteins [88]. In addition, some discrepancies on how SFKs positively or negatively affect cadherin adhesions exist among some early studies and remain to be addressed. For instance, during keratinocyte differentiation inhibition of SFKs suppresses adhesion formation and strength [89]. On

the contrary, expression of v-Src oncogene perturbs cadherin adhesions and contributes to invasive and metastatic potential of cells [90, 91]. More recently, multiple studies on the interplay between Src signaling and E-cadherin (epithelial cadherin) signaling have suggested that Src kinase, as the principal member of SFKs, is important to modulate the interaction of E-cadherin with the cytoskeleton and maintain the integrity of E-cadherin adhesion, as well as support apical junctional tension [30-33]. Despite these well-established mechanisms, what the molecular signaling dynamics are and how they are regulated across cells remain poorly understood, partially because of technical limitations by conventional biochemical and imaging methods. Therefore, of significant interest are novel approaches that can directly enable local physical perturbations and visualize the dynamics and transmission of subsequent signaling events across cells, so as to better understand crosstalk and integration of different signaling cascades at cell-cell contacts. Robotic laser micro-scissors allows us to ablate subcellular targets of single live cells with a high spatial precision [13-15]. This approach has been used in a wide variety of studies to introduce local physical perturbations on various cellular structures, such as mitochondria and cytoskeletons, and investigate how cell structures and functions are correlated [16-19]. In this study, I integrated photonics tools with molecular engineering and imaging, at a high spatiotemporal precision, to investigate intercellular signaling processes.

3.3. Materials and Methods

Laser scissors microscopy, image acquisition, and analysis. The robotic laser microscope system employed a Mai Tai laser (a mode-locked Ti:sapphire laser, 76 MHz 200 fs-pulsed, tunable between 710 nm and 990 nm, Spectra-Physics). The beam was

coupled to Zeiss inverted microscope (Axiovert 200M) via a series of highly reflective coated mirrors. A galvo scanner in the beam path enabled the precise scanning of the beam in the microscope optical field. The beam was focused via a 100x phase Zeiss microscope objective (NA = 1.4, transmission factor =0.72) to a diffraction-limited spot (0.618 μm at 740 nm). The pulse energy at the focused spot of 0.332 nJ at the average power of 25.2 mW before the objective was optimized for the desired disruption of cell-cell junctions. An EMCCD camera (QuantEM:512SC, Photometrics) was used to capture the fluorescent images. ECFP and FRET images were collected by the same Zeiss inverted microscope equipped with the X-Cite 120 LED (Excelitas Technologies Inc.) and an EMCCD camera (QuantEM:512SC, Photometrics) using MetaMorph 7.8.8.0 software (Molecular Devices LLC) with a 436DF20 excitation filter, a 455DCXRU dichroic mirror, and two emission filters (480DF30 for ECFP and 535DF30 YPet). The red fluorescent images (mCherry and TagRFP) were obtained with a 575DF50 excitation filter, a 610DCXRU dichroic mirror, and a 630DF50 emission filter. An emission filter wheel housed all the emission filters. All filters and dichroic mirrors were purchased from Carl Zeiss Inc. Cells were cultured for 36 hours in 0% FBS Advanced medium, and plated on glass-bottom dishes coated with FN (10 $\mu g \cdot ml^{-1}$) for one hour or overnight prior to laser ablation experiment. During laser ablation experiment, cells were maintained in 0% FBS Advanced medium at 37°C in a 5% CO_2 and 95% air-humidified stage top incubator (heating and gas incubation system, ibidi Inc.). After seeding cells on glass-bottom dishes, I first found adjacent cells with obvious cell-cell junctions formed, and then used laser scissors system to do multiple cuts around certain junction areas without any direct laser damage on the cell of interest. Thus, images were captured

during the laser-induced disruption of cell-cell junctions between neighboring cells. The image analysis was performed using our customized software *fluocell* [92, 93] written in MATLAB (The MathWorks Inc.). All the images were background-subtracted and smoothed using a median-filter with a window size of 3x3 pixels.

Statistical analysis. D'Agostino-Pearson omnibus normality test was used for the normality test. Data following Gaussian distribution were analyzed by using unpaired two-tailed Student's *t* test with Welch's correction or ordinary one-way ANOVA followed by Bonferroni's multiple comparisons test (Graphpad Prism 6, GraphPad Software) to evaluate the statistical difference between groups. Data not following Gaussian distribution were analyzed by using unpaired two-tailed Mann-Whitney test or Kruskal-Wallis test followed by Dunn's multiple comparison test (Graphpad Prism 6, GraphPad Software). A significant difference was determined by *P* value ($P < 0.05$). Statistical results are presented as mean ± S.E.M. Asterisks indicate critical values ($*P < 0.05$, $**P < 0.01$ and $***P < 0.001$), and "n.s." indicates no significant difference ($P > 0.05$). All the experiments were replicated at least 3 times and represented biological replicates.

For "Constructions of DNA plasmids" and "Cell culture, reagents and transient transfection", please refer to "2.2. Materials and Methods" section.

3.4. Results and Discussion

3.4.1. Observation of Src signaling transmission following the laser-induced disruption of cell-cell contacts

In order to study the dynamics of Src kinase activity during the signal transmission between neighboring cells, I applied the SCAGE biosensor for FRET imaging in adult male *Potorous tridactylus* kidney (PtK2) epithelial cells. Employing

femtosecond robotic laser scissors microscopy, I selectively ablated cytoskeletal stress fibers along cell-cell junctions and visualized the signal transmission and propagation across neighboring cells using our SCAGE Src biosensor (Fig. 3.1.A). Indeed, as shown in Fig. 3.1.B (red lines), I can precisely irradiate single actin filaments, highlighted by LifeAct-RFP [94]. Consequently, the neighboring cells quickly retracted and disassociated from the cell of interest (Fig. 3.1.B), likely due to the loss of mechanical tension upon the stress fiber ablation [17]. In response to the loss of cell-cell contacts, the cell of interest underwent retraction and transient Src activation (Fig. 3.1.C-E). Such FRET responses were absent with the inactive CA/GE/RV/YF biosensor (Fig. 3.1.F). The absence of Src activation in cells residing next to others but not forming stable and physical cell-cell contacts (Fig. 3.1.F, Cutting Control) suggests that the observed Src activation requires physical cell-cell contacts, but not the release and diffusion of chemical constituents between neighboring cells. The response from the Ori biosensor was very minor and almost undetectable, clearly highlighting the power of the new SCAGE Src biosensor (Fig. 3.2).

3.4.2. Regulation of Src signaling activation following the disruption of cell-cell contacts through the passive cytoskeletal structure but not through the active actomyosin contractility

Cytoskeletal support and contractile forces are of vital importance in regulating cell-cell adhesions [26, 29-31, 95]. To understand the regulation of the observed Src transmission upon the laser-induced physical disruption of cell-cell contacts, I investigated the roles of cytoskeleton and its related cellular contractility. I pretreated PtK2 cells with cytochalasin D (CytoD, an inhibitor of actin polymerization) to disrupt

the cytoskeletal structures, or ML-7 (a myosin light chain kinase inhibitor) to suppress the active actomyosin contractility. The transient Src activation was completely eliminated with pretreatment by CytoD but not ML-7 (Fig. 3.1.F), although ML-7 clearly suppressed the activity of focal adhesion kinase in PtK2 cells (Fig. 3.3). These results illustrate that the observed Src signaling transmission depends on the structural support of actin filaments but not the actomyosin contractility. Therefore, integrating the high-sensitivity Src FRET biosensor with laser scissors technology, I have concluded that the Src signaling transmission across neighboring cells requires the passive cytoskeletal structure but not the active actomyosin contractility system.

3.5. Conclusion

Employing FRET microscopy and robotic laser scissors (Fig. 3.1.A), I demonstrated a rapid Src signaling occurring as a signal transmission between neighboring cells upon the femtosecond laser-induced physical disruption of cell-cell contacts (Fig. 3.1.C, D). This rapid activation can be associated with actin reorganization and mechanical adaption during the period when the cell loses its adhesive contacts with its neighbors. Interestingly, the inhibition assay reveals that this fast and transient Src signaling event depends on the passive cytoskeletal structure but not the active actomyosin contractility system. These results suggest that the physical perturbations on cells introduced by laser pulses may deliver a profound physical impact which can be transmitted afar and across to neighboring cells via the passive structural support without the aid of actomyosin contractility. As such, the integrated photonic approach together with highly sensitive FRET biosensors can lead to the revelation of how cells perceive physical perturbations from neighboring cells and trigger biochemical responses.

3.6. Figures

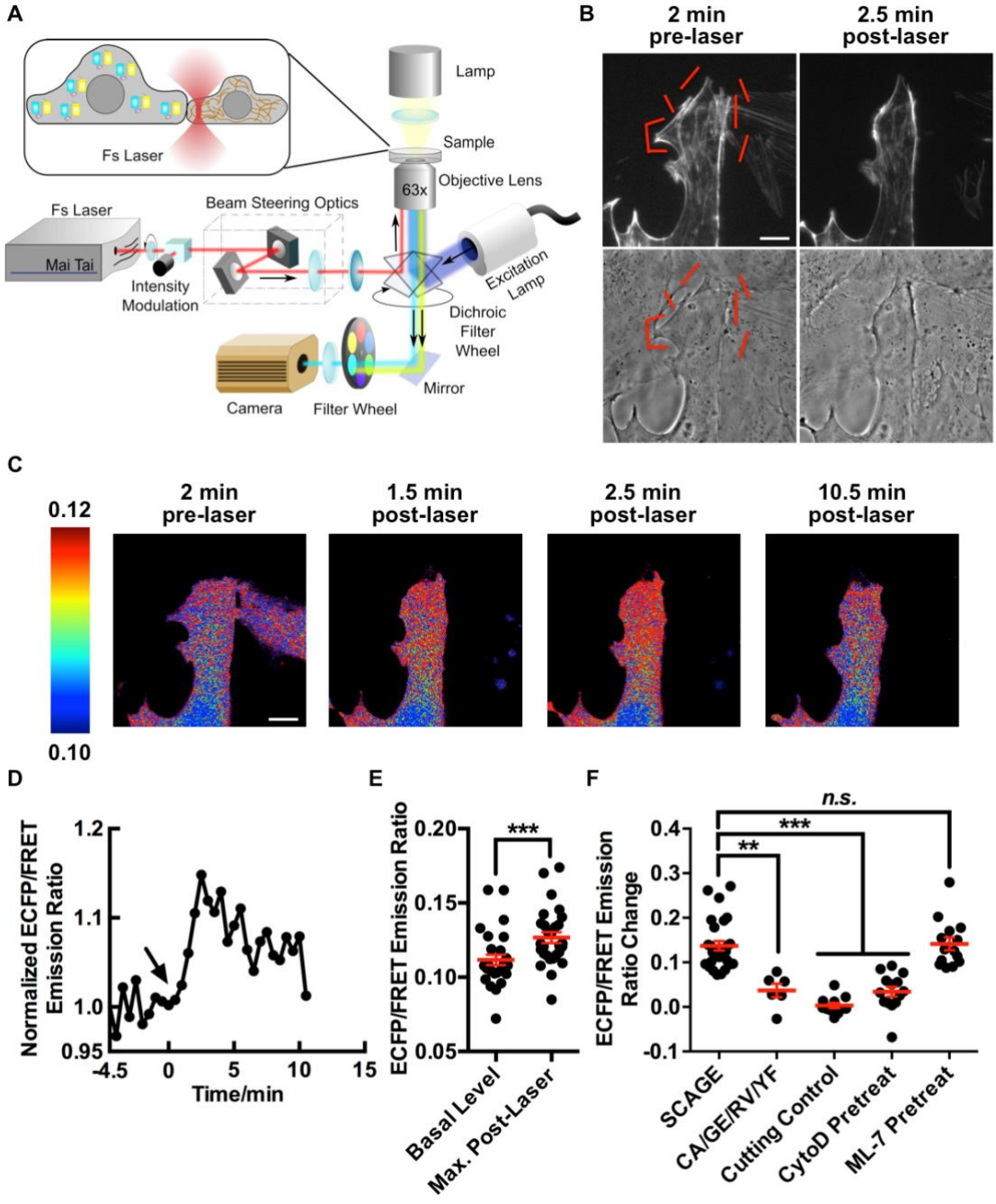

Figure 3.1: Regulation of the transient Src activation following the laser-induced disruption of cell-cell contacts.

(**A**) The system setup diagram of the robotic laser scissors integrated with an inverted fluorescence microscope for FRET imaging. "Fs laser" represents femtosecond-pulsed

Figure 3.1: Regulation of the transient Src activation following the laser-induced disruption of cell-cell contacts, Continued

laser. (**B**) Time-lapse imaging in adult male *Potorous tridactylus* kidney (PtK2) epithelial cells expressing a filamentous actin (F-actin) marker (LifeAct-TagRFP) upon the laser-induced disruption of cell-cell contacts. RFP-channel F-actin images (upper panel) and phase-contrast images (lower panel) of PtK2 cells at the indicated time points before and after laser laser-induced disruption of cell-cell contacts are shown. The red lines indicate the positions of laser ablation. Scale bars, 5 μm. (**C**) Time-lapse FRET imaging in PtK2 cell expressing SCAGE Src biosensor before and after the laser-induced disruption of cell-cell contacts. ECFP/FRET ratio images at the indicated time points are shown in intensity-modulated display mode. The color scale bar at the left shows the range of ECFP/FRET emission ratio, with cool and warm colors representing low and high ratios, respectively. Scale bars, 5 μm. (**D**) The time course of the normalized ECFP/FRET emission ratios of the SCAGE biosensor in PtK2 cell before and after laser-induced disruption of cell-cell contacts (arrow at 0 min). The ECFP/FRET emission ratios are normalized against the average value before laser ablation. (**E**) The ECFP/FRET emission ratios of the SCAGE biosensor in PtK2 cells (n = 28) before and after laser-induced disruption of cell-cell contacts. *** ($P < 0.001$) is from unpaired two-tailed Mann-Whitney test. (**F**) The ECFP/FRET emission ratio changes of SCAGE Src biosensors as indicated in PtK2 cells in response to laser-induced disruption of cell-cell contacts. CA/GE/RV/YF group is the inactive control group, Cutting Control is SCAGE biosensor group in which cells are next to each other without forming direct physical cell-cell contacts, CytoD Pretreat group is SCAGE biosensor group pretreated with cytochalasin D (CytoD), and ML-7 Pretreat group is SCAGE biosensor group pretreated with ML-7 (n = 28, 6, 11, 14, and 14 cells for SCAGE, CA/GE/RV/YF, Cutting Control, SCAGE with CytoD Pretreat and SCAGE with ML-7 Pretreat groups, respectively). 1 μM CytoD and 10 μM ML-7 are applied to inhibit actin polymerization and actomyosin contractility, respectively. *** ($P < 0.001$), ** ($P < 0.01$), n.s. ($P > 0.05$) are from Kruskal-Wallis test followed by Dunn's multiple comparison test. (**E-F**) In scatter plots, the red lines indicate the mean values, the error bars represent S.E.M. and average data are presented as mean ± S.E.M.

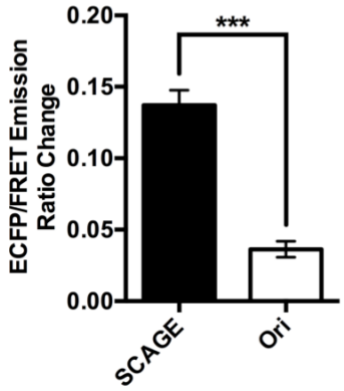

Figure 3.2: The responses of different FRET-based Src biosensors in PtK2 cells subjected to the laser-induced disruption of cell-cell contacts.

Bar graphs represent the average ECFP/FRET emission ratio changes (mean ± S.E.M.) of different Src biosensors in response to the laser-induced disruption of cell-cell contacts in PtK2 cells (n = 28 for the SCAGE group and n = 14 for the Ori group). *** ($P < 0.001$) is from unpaired two-tailed Mann-Whitney test.

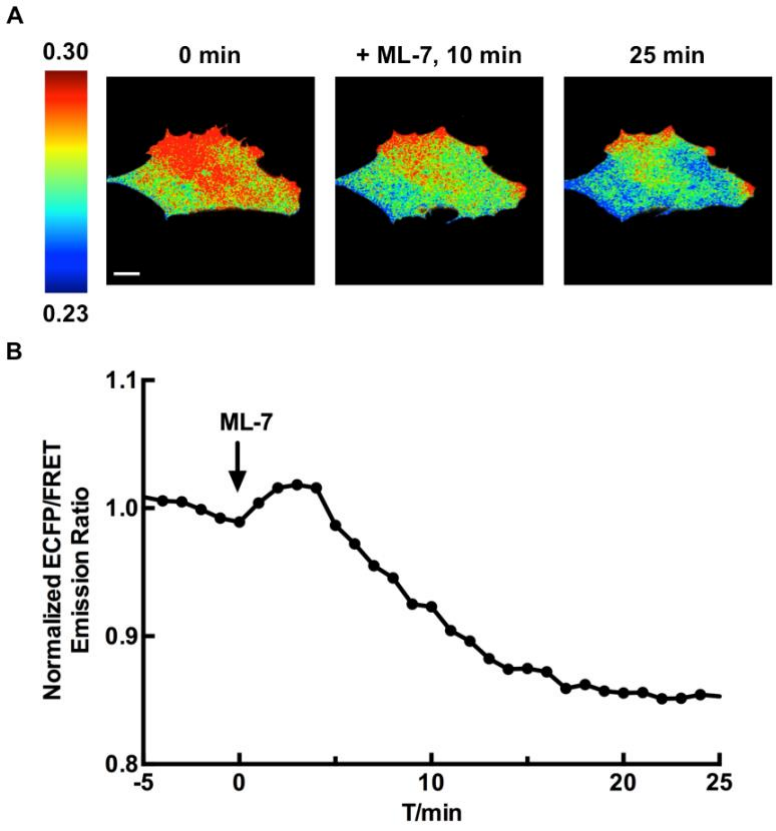

Figure 3.3: Effects of Myosin light chain kinase inhibitor on FAK activity in PtK2 cells.

(**A**) Time-lapse FRET imaging of PtK2 cells expressing Lyn-FAK (focal adhesion kinase) biosensor treated with 10 μM ML-7. ECFP/FRET ratio images of PtK2 cells expressing Lyn-FAK biosensor at the indicated time points before and after ML-7 treatment are shown in intensity-modulated display mode. The color scale bar at the left shows the range of ECFP/FRET emission ratio, with cool and warm colors representing low and high ratios, respectively. Scale bars, 5 μm. (**B**) The time course of the normalized ECFP/FRET emission ratios of Lyn-FAK biosensor in PtK2 cell before and after 10 μM ML-7 treatment (arrow at 0 min). ECFP/FRET emission ratios are normalized against the average value before 10 μM ML-7 treatment.

Chapter 4: Engineering Immune Cells for Cancer Therapy Through Synthetic Molecular Machinery

4.1. Abstract

Immunotherapy, especially T-cell therapy, presents promising potential by stimulating immune system to regain its ability to recognize and attack tumor cells. However, PD-1/PD-L1 (programmed death receptor 1 and its ligand 1) signaling-mediated inhibition of T cells dampens the efficacy of T-cell therapy and makes certain tumors very difficult to treat. Therefore, in this study I employed synthetic biology approaches to rewire co-inhibitory PD-1 signaling with T cell activation signaling via synthetic molecular machineries. Specifically, upon the ligation between PD-1 and PD-L1, the synthetic molecular machineries converted the negative input signal via PD-1/PD-L1 into the positive output signals via ZAP70 kinase (zeta-chain-associated protein kinase 70), which helps to overcome PD-1/PD-L1 signaling-mediated T cell inhibition and thus enhance T cell functions and responses against tumor cells. Together, I demonstrated the potential significance of the synthetic molecular machineries for immunotherapy purposes. These tools may open a new avenue towards cancer therapy and provide innovative and precise therapeutic approaches for better cancer treatment.

4.2. Introduction

Nowadays, cancer diseases with poor survival rates become one of the primary challenging diseases to the global human society [96]. In the US, cancer is the second leading cause of death in 2016, which is only exceeded by heart disease. There are more than one hundred types of cancer caused by many different reasons and they together

account for about one of every four deaths in the US [97, 98]. One of the reasons why cancer could be very lethal is because that cancerous cells grow and divide very rapidly and may become malignant in the late stage of cancer by breaking through the boundary of normal tissues and invading neighboring tissues and even spreading to other parts of the body through the bloodstream or lymphatic system, which is called metastasis and further reduces the chance to treat and eradicate tumor cells [99, 100]. Although the immune system constantly defends and protects people against various diseases, sometimes it fails to provide the protection our body needs, for instance, when it battles against cancer. One of the major causes is that tumor can escape the immune surveillance to enhance their survival, i.e. causing cancer immune evasion [34], and suppress immune system by interfering with the anti-cancer immune responses, such as utilizing certain immune checkpoint signaling pathways to inhibit and turn off T cell functions against tumor cells [35]. As a result, T cells can no longer function normally under the circumstance that cancer cells develop the resistance to immune recognition and killing.

From the laboratory-bench perspective, it is fairly well understood that T lymphocytes, as one of the major components of the adaptive immune system, play the central role in adaptive immune responses and how their functions and behaviors are regulated [36-39]. T cell receptor (TCR) signaling with modulations by co-stimulatory and co-inhibitory receptors controls T cell fate decisions, such as activation, proliferation, differentiation, function and survival [36, 40-42, 101-105].

Antigen-presenting cells (APCs) are also of vital importance to adaptive immune responses. They display antigenic peptides on their surfaces complexed with major histocompatibility complexes (MHCs), i.e. antigen presentation. The interactions between

peptide-MHC molecules on the surfaces of APCs and antigen-specific TCR complexes on the surfaces of T cells initiate the subsequent membrane-proximal TCR signaling cascades by means that multi-subunit TCR complexes transduce the signals across T cell membranes upon binding to the peptide-MHC complexes at immunological synapses [106-108]. This process, known as TCR triggering, results in the activation of T cells in an antigen-specific mode. Other than TCR, there are other crucial molecules involved in the TCR triggering. T cells express co-receptor molecules (cluster of differentiation 4 or 8, i.e. CD4 or CD8) on the surfaces, which can bind to peptide-MHC complexes as well as recruit Src family kinase member Lck [40, 109, 110]. During T cell signaling transduction, the CD4/CD8-associated tyrosine kinase Lck or lipid-raft-localized Fyn serves as a priming module, which phosphorylates the motifs on the cytoplasmic domains of CD3 subunits of TCR/CD3 complexes [111]. The phosphorylated motifs as docking sites recruit one essential kinase called TCR-zeta-chain-associated protein kinase 70 (ZAP70) by binding to its tandem SH2 domains and this binding event results in the phosphorylation by Lck kinase and its trans-autophosphorylation, which leads to the activation of ZAP70 from its autoinhibition [40, 112-114].

ZAP70, as a cytoplasmic tyrosine kinase of spleen tyrosine kinase (SYK) family [115], mainly expresses in T cells and is known to be critical to T cell development and function. After ZAP70 becomes active, it in turn amplifies and disperses the activation signals by phosphorylating numerous signaling proteins, such as the linker for the activation of T cells (LAT) and the SH2-domain-containing leukocyte protein of 76 kDa (SLP76) [40, 112, 114]. The phosphorylated LAT next serves as a scaffold protein to recruit many other signaling molecules, to form a large multimolecular complex, named

"LAT signalosome", which comprises a number of important proteins, such as SLP76, growth factor receptor-bound protein 2 (GRB2), interleukin-2-inducible T cell kinase (ITK) and phospholipase Cγ1 (PLCγ1). The signals received at the LAT signalosome are then transmitted downstream through different signaling branches, which mainly include the calcium signaling, the nuclear factor-κB (NF-κB) signaling and the mitogen-activated protein kinase (MAPK) kinase signaling. These signaling events regulate transcription process for gene expression, actin reorganization and integrin activation. As a consequence, these events together allow T cells to activate, proliferate, and differentiate.

In fact, T cells are like conductors of the immune orchestra. Appropriate T cell behaviors and functions do require accurate control of a sophisticated repertoire of signals to properly coordinate. Otherwise, relevant defects would lead to immunopathology and cause disease or disorder, such as autoimmune diseases, allergic diseases, immunodeficiency disorders and so on [116]. To accomplish the precise coordinated regulation, T cells employ other pivotal mechanisms to determine TCR signaling outcome and modulate their activation, differentiation and function, specifically co-regulatory signals including co-stimulatory signals and co-inhibitory signals [42, 104, 105].

Co-stimulatory signals, as accelerators of immune system, positively modulate TCR signaling and they are required for effective T cell activation to occur, for instance, CD28 bound by its ligand B7-1, i.e. CD80 [104, 105]. Other than T cell activation, co-stimulatory signaling is also crucial to other multiple aspects, such as T cell proliferation, differentiation, cytokine production, effector/cytotoxic function, memory formation, and survival.

As opposed to co-stimulatory signals, co-inhibitory signals like brakes of immune reaction negatively regulate TCR signaling through co-inhibitory receptors and their ligands on T cells and APCs respectively. For instance, a co-inhibitory receptor, cytotoxic T-lymphocyte-associated antigen 4 (CTLA-4 or CD152, a member of CD28 family), can bind to B7-1 (CD80), downregulate CD28 expression and inhibit T cell responses [104, 117-124]. B7-2 (CD86) is discovered to be the second ligand for CTLA-4 and CD28. Besides CTLA-4, program death-1 (PD-1 or CD279) from the CD28 family of receptors is also known to suppress T cell activation and functions [104, 123-129]. There are two ligands from B7 family discovered in PD-1 signaling, i.e. PD-1 ligand 1 (PD-L1 or B7-H1) and PD-1 ligand 2 (PD-L2 or B7-DC) [130-132]. These two PD-1 ligands show distinct expression patterns. PD-L1 expression is much more diverse while PD-L2 has more restricted expression pattern. As for the immune system, it is essential for T cells to distinguish self from nonself so that T cells can properly become activated or anergic under different circumstances. Suitable and precise regulations of central and peripheral T cell tolerance are critical to this process [133, 134].

CTLA-4 and PD-1 are two central immune checkpoint receptor proteins, which involve in maintaining T cell tolerance and homeostasis and preventing T cells from being self-reactive and abnormal autoimmune reactions [123, 124]. CTLA-4 signaling plays a pivotal role in central T cell tolerance by acting early to remove autoreactive T cells during the initial activation of naïve T cells typically in thymus and lymph nodes, possibly spleen. Loss of CTLA-4 can provoke lymphoproliferative disorders and autoimmune diseases [135, 136]. Differently, PD-1 signaling acts late to maintain long-term T cell tolerance by regulating previously activated T cells, principally in peripheral

tissues [137-139]. PD-1 deficiency can cause autoimmune diseases via failure of peripheral self-tolerance [140-144]. The PD-1 downstream signals can also affect numbers of other T cell functions, such as inhibiting T cell proliferation, metabolism, survival, effector function and production of inflammatory cytokines [35, 126, 145, 146].

Furthermore, failure of appropriate T cell tolerance may be responsible to other severe pathological problems like infectious diseases and tumors. Especially by seizing control of T cell tolerance, cancer cells have found smart ways to co-opt immune system and avoid immune surveillance, also called tumor escape. For example, cancerous cells overexpress PD-L1 to evade the host immune system, particularly in solid tumors [147].

In the past, typical ways used to treat tumors include surgery, hormonal therapy, radiation therapy, chemotherapy, and appropriate combination therapy [148, 149]. These traditional therapies indeed can slow down the spread of tumors and lessen the symptoms. However, compared to these conventional treatment approaches, immunotherapy as the next generation cancer therapeutic strategy starts showing improvements on efficacy and safety with durable responses, better tolerability, milder side effects and longer survival [43, 150]. As knowledge and understanding of immune system grows, people are beginning to realize the power and immensity of their immune system and to harness immune system function to treat cancer. In the meantime, recent advances in synthetic biology for genetically engineering immune cells have opened a new avenue towards next-generation cancer immunotherapy by unleashing the potential of our immune system, especially acquired immune system [151]. Based on that, researchers and engineers have made a lot of effort to develop and deploy reliable and effective therapeutic platforms and systems against a variety of tumors. Remarkable milestones in immunotherapy have

already been achieved, especially that chimeric antigen receptor (CAR) T-cell therapy inspired endogenous TCR signaling for blood tumors, including lymphoma and lymphocytic leukemia, and blockade of immune checkpoints (CTLA-4 and PD-1) inspired by endogenous co-regulatory signaling for a wide range of human tumors have already led to enormous success against cancer in compelling clinical trials [152-156]. These together are initiating a new era of medicine and provide transformative ways in the battle against diseases, especially cancer.

In essence, CAR is a recombinant receptor protein with both antigen recognition and T cell activation functions. It has four major components: an antigen-binding domain, a hinge domain, a transmembrane domain and an intracellular domain carrying single or multiple signaling segments [44, 156-158]. The antigen-binding domain is typically a single-chain variable fragment (scFv) derived from a monoclonal antibody and is able to target specific surface antigen expressed on cancer cells. The hinge domain is a flexible region connecting the ectodomain to the transmembrane domain that locates the CAR to plasma membrane. Both hinge and transmembrane domains profoundly affect the functions of CAR T-cell functions [159]. The endodomain is responsible to T cell activation upon CAR engagement, which has different design strategies among different generations of CARs: first-generation CARs have only one activation module derived from CD3ζ, second-generation CARs contain one extra co-stimulatory domain from CD28 or CD137 (4-1BB), and third-generation CARs carry two extra co-stimulatory domains, such as CD27, CD28, CD278 (ICOS), 4-1BB, or/and CD134 (OX40) [44, 155, 156].

Although CAR T-cell therapy presents promising potential by stimulating immune system to regain its ability to recognize and attack certain cancer cells, it is still questionable whether such successful therapies could effectively expand beyond blood cancers. For example, it would require eliminating multiple hurdles to treat malignant solid tumors. CAR T cells need to infiltrate into unique solid tumor microenvironments and sustain proliferative and cytotoxic functions. One of major challenges is PD-1/PD-L1 signaling-mediated inhibition of T cells, which dampens CAR T-cell therapy and makes solid tumors very difficult to treat [123, 160]. One way to tackle that now is through blockade of PD-1, such as genetic disruption and inhibitor treatment. Multiple studies demonstrate that PD-1 blockade can boost T cell potency and enhance CAR T-cell therapy without noticeable negative effects [45, 161-164].

Inspired by the aforementioned work on TCR activation signaling and co-inhibitory signaling, in this study I employ synthetic biology approaches to rewire co-inhibitory signaling with TCR activation signaling via synthetic molecular machineries. Specifically, upon the ligation between PD-1 and PD-L1, the synthetic molecular machineries convert the negative input signal via PD-1/PD-L1 into the positive output signals via ZAP70 kinase, which helps to overcome PD-1/PD-L1 signaling-mediated T cell inhibition and tackles cancer more effectively.

4.3. Materials and Methods

Constructions of DNA plasmids. LacZ-ECFP-linker-YPet-SYK or ZAP70 construct was assembled into customized pCAGGS vector (I named it by pCBI) by 6-piece ligation using T4 DNA ligase (New England Biolabs Inc.) [55, 56]. The pieces include linear customized pCAGGS vector, LacZ, ECFP (enhanced CFP, truncated at the C terminus), a 116 aa linker, YPet and the full-length human SYK or ZAP70 kinase [54, 56]. LacZ part as a screening module used in all my experiments is a portion of LacZ gene instead of full-length LacZ operon, sometimes called LacZ-alpha. iSNAP-SYK or iSNAP-ZAP70s were then constructed based on LacZ-ECFP-linker-YPet-SYK or ZAP70 construct by replacing LacZ part in customized pCAGGS vector with different DNA sequences encoding different substrates derived from CD3 chains using Golden Gate assembly. For full-length human PD-1 or truncated human PD-1 fused iSNAPs, using Golden Gate assembly, DNA sequence encoding full-length human PD-1 (FL-PD-1) or truncated human PD-1 (T-PD-1) was assembled into LacZ-ECFP-linker-YPet-SYK or ZAP70 together with different substrates by replacing the LacZ part in customized pCAGGS vector. Different substrate negative mutants of T-iSNAP-SYK and ZAP70s were made into customized pCAGGS vector by Golden Gate assembly, including S1FF, Z1FF, Z2FF and Z3FF. T-PD-1-iSNAP-ZAP70s with extra internal linkers (34 aa linker or 116 aa linker) were assembled into customized pCAGGS vector by multiple piece ligation. Kinase dead versions of both kinases (SYK K402A and ZAP70 K369A) were first made by site-directed mutagenesis on the wild-type full-length human SYK and wild-type full-length human ZAP70 in pDONR223 vector (Plasmids #23907 and #23887) purchased from Addgene and then assembled into customized pCAGGS vector. The 6xHis tagged

T-iSNAP-SYK and ZAP70s were made into customized pCAGGS vector by Golden Gate assembly for protein purification from human embryonic kidney (HEK) cells. The extracellular domain of human PD-L1 was inserted into pEF-BOS vector using XbaI/SalI restriction sites for protein purification from HEK cells [165, 166]. All PCR templates for human PD-1 and human PD-L1 were pMD-PD1 (HG10377-M) and pMD-PD-L1 (HG10084-M) purchased from Sino Biological Inc. respectively.

For lentivirus expression system in mammalian cells, I used secondary generation lentiviral system with packaging and envelope plasmids (pCMV-VSV-G, pCMV delta R8.2 or psPAX2, pDM2.G). The transfer plasmids include pSIN-EF1a (EF1 alpha constitutive promoter) with Puromycin resistance gene (PuroR) and pSIN-hPGK (human phosphoglycerate kinase constitutive promoter) with cPPT/CTS element and the woodchuck hepatitis virus posttranscriptional regulatory element (WPRE) to increase transgene expression [167]. Full-length human PD-1-GGSGGT-EGFP/YPet/mCherry were first assembled into customized pCAGGS vector by multiple piece ligation and further constructed into pSIN-EF1a-PuroR by SpeI/EcoRI. Full-length human PD-L1 was inserted into pSIN-EF1a-PuroR by same SpeI/EcoRI sites. Linear pSIN-hPGK-WPRE vector as one DNA fragment for ligation was made from PGK-H2BmCherry (Addgene, Plasmid #21217) as the PCR template. LacZ part and linear pSIN-hPGK-WPRE vector were then assembled by Gibson Assembly (New England Biolabs Inc.) to construct pSIN-hPGK-LacZ-WPRE plasmid. iSNAP Constructs, T-PD-1-Z1-full-length-ZAP70 (1 to 619) and T-PD-1-Z1-ZAP70 kinase domain deletion (1 to 337), were made into customized pCAGGS vector by Golden Gate assembly, and further subcloned into pSIN-hPGK-WPRE plasmid by replacing the LacZ part via NheI/XbaI sites. T-PD-1-iSNAP-

ZAP70-Z1 was also transferred into pSIN-hPGK-WPRE plasmid via same NheI/XbaI sites. c-Myc tag (EQKLISEEDL) was inserted right after PD-1 signal peptide (1 to 20) of different iSNAPs using QuikChang kit (Agilent Technologies Inc.) to make different c-Myc tagged T-PD-1-iSNAPs.

All the site-directed mutagenesis experiments were also conducted using the same QuikChange kit. All the constructed DNA plasmids were analyzed and confirmed by restriction enzyme digestion and Sanger DNA sequencing (GENEWIZ Inc.).

Cell culture, reagents and transient transfection. Mouse embryonic fibroblas (MEF), HeLa, and HEK cells were maintained in Dulbecco's modified Eagle's medium (DMEM) supplemented with 10% fetal bovine serum (FBS), 2 mM L-glutamine, 1 unit·ml^{-1} penicillin, 100 μg·ml^{-1} streptomycin, and 1 mM sodium pyruvate, except when indicated otherwise. ASPC-1, MDA-MB-231, PC-3, Jurkat E6.1 cells and peripheral blood mononuclear cells (PBMCs) were maintained in Roswell Park Memorial Institute (RPMI) 1640 medium supplemented with 10% fetal bovine serum (FBS), 2 mM L-glutamine, 25 mM HEPES, 1 unit·ml^{-1} penicillin, and 100 μg·ml^{-1} streptomycin, except when indicated otherwise. NALM-6 cells were maintained in RPMI 1640 medium supplemented with 10% FBS, 1x MEM non-essential amino acids solution, 2 mM L-glutamine, 10 mM HEPES, 1 mM sodium pyruvate and 50 μM 2-mercaptoethanol, except when indicated otherwise. Cell culture reagents were purchased from Thermo Fisher Scientific Inc. NALM-6 cell line expressing firefly luciferase-GFP was a generous gift from Dr. Sadelain at Memorial Sloan Kettering Cancer Center, New York. ASPC-1, MDA-MB-231, and PC-3 cell lines were generous gifts from Dr. Strongin at Sanford Burnham Prebys Medical Discovery Institute, La Jolla. PBMCs were purified using lymphocyte

separation medium (Corning Inc.) from whole blood obtained from San Diego Blood Bank. Other cell lines were purchased from American Tissue Culture Collection (ATCC, Manassas, VA). The different kinds of cells were cultured in ATCC recommended conditions at 37°C in a 5% CO2 and 95% air-humidified incubator. The DNA plasmids were transfected into the cells by using Lipofectamine 2000 or 3000 reagent (Thermo Fisher Scientific Inc.), according to the manufacturer's instructions, or by using my optimal electroporation protocol: 40 μg DNA for 10 million live cells in 4 mm cuvette (Genesee Scientific Inc.) with 500 μL Opti-MUM (Thermo Fisher Scientific Inc.) by Bio-Rad Gene Pulser Xcell Electroporation System at 270 V, 950 μF (exponential wave, infinite resistance) [168].

Pervanadate was prepared following the protocol described before [169]. Fibronectin from bovine plasma (FN), poly-L-lysine (PLL), human epidermal growth factor (EGF) and rat recombinant platelet-derived growth factor BB (PDGF) were obtained from Sigma Aldrich Inc. Collagen type-I from rat tail (Col I) was purchased from BD Biosciences, BD. Recombinant human interferon-gamma was purchased from R&D Systems Inc. Puromycin was purchased from Thermo Fisher Scientific Inc.

Protein expression and purification, *in vitro* spectroscopy and kinase assays. HEK cells transfected with different iSNAPs were washed with cold PBS and then lysed in 1x cell lysis buffer (Cell Signaling Technology Inc.) containing 0.2 mM PMSF and one tablet of cOmplete™ Mini EDTA-free protease inhibitor cocktail (Roche Molecular Systems Inc.). Lysates were sonicated at 4 °C for 5 min and centrifuged at 7,200 x g at 4°C for 20 min. Supernatants were incubated with Ni-NTA agarose beads (QIAGEN Inc.) to capture the desired proteins via their N-terminal 6x His tag and purify by nickel

chelation chromatography [24]. Bead-bound iSNAPs were then washed with 50 mM Tris-HCl pH 7.5, 100 mM NaCl, 10 mM imidazole. iSNAPs were eluted in a buffer containing 50 mM Tris-HCl pH 7.5, 100 mM NaCl, and 100 mM imidazole and then dialysed against the kinase assay buffer (50 mM Tris-HCl, 100 mM NaCl, 10 mM MgCl2, 2 mM DTT, pH 8.0) at 4°C overnight. Fluorescence emission spectra of the purified iSNAPs were measured in a 96-well plate with an excitation wavelength of 433 nm by a fluorescence plate reader (infinite M1000 PRO, TECAN Inc.). The emission ratios of ECFP/YPet (478 nm/528 nm) were measured before and after adding 1 mM ATP (Promega Inc.) into the kinase assay buffer (50 mM Tris-HCl, 100 mM NaCl, 10 mM MgCl2, 2 mM DTT, pH 8.0) at 37°C that contained a mixture of various iSNAPs (1 μM) and N-terminal 6xHis-tagged recombinant full-length human Src, Fyn (5 $\mu g \cdot ml^{-1}$, EMD Millipore Inc.) or N-terminal GST tagged recombinant full-length human Lck kinase (5 $\mu g \cdot ml^{-1}$, Sigma Aldrich Inc.). Kinase activities of purified iSNAPs were measured in a 96-well plate by Synergy HT plate reader (BioTek Instruments Inc.) using ADP-Glo™ kinase assay kit (Promega Inc., 560 nm luminescence). The purified iSNAPs (1 μM) were pulled down by Ni-NTA agarose beads (QIAGEN Inc.) after incubation at 37°C with or without Fyn kinase (5 $\mu g \cdot ml^{-1}$, EMD Millipore Inc.) or Lck kinase (5 $\mu g \cdot ml^{-1}$, Sigma Aldrich Inc.) in the kinase assay buffer for certain duration, and were then measured for kinase activities using ADP-Glo™ kinase assay kit (Promega Inc.) according to the manufacturer's instruction.

Protein expression and purification of recombinant human PD-L1 and its coating on polystyrene particles. Plasmid encoding the extracellular domain of human PD-L1 was

constructed as described in "Constructions of DNA plasmids" based on the plasmid as a gift from Dr. Dennis E. Discher (Molecular and Cell Biophysics Laboratory, University of Pennsylvania) [165, 166]. The plasmid was transfected into HEK cells using Lipofectamine 3000 reagent (Thermo Fisher Scientific Inc.), according to the manufacturer's instruction. After two-day culture, advanced DMEM (Thermo Fisher Scientific Inc.) containing secreted PD-L1-CD4d3+4 with the addition of one tablet of cOmplete™ Mini EDTA-free protease inhibitor cocktail (Roche Molecular Systems Inc.) was concentrated using a 10K MWCO Amicon (EMD Millipore Inc.), and PD-L1-CD4d3+4 was biotinylated at the C terminus using a biotin-protein ligase (Avidity LLC) at 30°C and dialyzed against PBS at 4°C overnight. The biotinylated PD-L1-CD4d3+4 was purified using monomeric avidin resin (Promega Inc.) and dialyzed against PBS at 4°C overnight. The concentration of purified protein was measured using Bradford protein assay. Streptavidin-coated polystyrene particles (2 μm diameter, Spherotech Inc.) were washed and incubated with biotinylated PD-L1 in 0.4% BSA/PBS at 4°C overnight, followed by three washes and resuspension in cell culture medium. The size of PD-L1-CD4d3+4 is about 50 kDa.

Immunoblotting. After purification and biotinylation of human PD-L1, the proteins were resolved by SDS-PAGE, and then transferred onto nitrocellulose membranes and blocked with 5% BSA in TBST buffer (20 mM Tris-HCl, 150 mM NaCl, 0.1% Tween 20, pH 7.6) for 1 hour at room temperature. Membranes were further incubated with primary antibodies at 4°C overnight, washed and then incubated with HRP-conjugated secondary antibodies for 1 hour at room temperature. Protein bands were detected using SuperSignal Western Pico chemiluminescent substrate (Thermo Fisher Scientific Inc.).

Anti-human PD-1 monoclonal antibody and Alexa Fluor 488 streptavidin was purchased from eBiosciences, Thermo Fisher Scientific Inc. Goat anti-mouse IgG HRP-conjugated polyclonal antibody was purchased from Santa Cruz Biotechnology Inc.

Flow cytometry, cell staining, co-culture and T cell activation. For the measurement of surface expression of PD-1, PD-L1, and c-Myc tagged proteins, HEK, ASPC-1, MDA-MB-231, and PC-3 cells were first transfected or infected and detached by treatment of 8 mM EDTA (pH 8.0) in PBS or Accutase (Innovative Cell Technologies Inc.), then washed with 0.5% BSA/PBS. For Jurkat, NALM-6 cells and PBMCs, they were transfected or infected and then washed with 0.5% BSA/PBS. After washing, non-specific surface residues of cells were blocked for 10 min by 0.5% BSA/PBS at 37°C, and incubated with mouse anti-human PD-1 antibody (APC conjugate, BioLegend Inc.), mouse anti-human PD-L1 antibody (APC conjugate, BioLegend Inc.), mouse anti-human PD-L1 isotype antibody (APC conjugate, BioLegend Inc.) or mouse anti-c-Myc tag antibody (Alexa Fluor 647 Conjugate, Cell Signaling Technology Inc.) for 30 min at 37°C.

For the measurement of expression of fluorescent proteins, HEK, Jurkat, NALM-6 cells, and PBMCs were transfected, collected and washed with 0.5% BSA/PBS to remove the cell culture medium before flow cytometry analysis. For the measurement of very early T cell activation marker CD69 on the cell surface, Jurkat cells were transfected and then co-cultured with antigen-presenting cells for 24 hours, for example MDA cells with human interferon-gamma (500 U/mL, i.e. 25 ng/mL) pretreatment. Then Jurkat cells were collected and washed with 0.5% BSA/PBS. After washing, non-specific surface

residues of cells were blocked for 10 min by 0.5% BSA/PBS at 37°C, and incubated with mouse anti-human CD69 antibody (APC conjugate, BioLegend Inc.) for 30 min at 37°C.

All flow cytometric data were acquired using a BD Accuri C6 cytometer (BD Biosciences, BD) and analyzed using BD Accuri C6 1.0.264.21 software (BD Biosciences, BD). The acquisition configurations using a BD Accuri C6 cytometer for different fluorescent proteins and dyes are listed as following: EGFP, YPet (488 nm excitation laser and emission filter 530DF30), and APC (640 nm excitation laser and emission filter 675DF25).

Stable cell line generation. To generate HEK cell line for the stable expression of full-length human PD-L1 driven by EF1α promoter, HEK cells were first lentivirally transduced. Following viral infection, cells were selected using 1 μg/mL puromycin for three days. HEK cells were also transduced to stably express full-length PD-1-GGSGGT-EGFP. To generate NALM-6 cell line for the stable expression of full-length PD-L1 driven by EF1α promoter, NALM-6 cells expressing firefly luciferase-GFP were lentivirally transduced and sorted for stable expression of full-length PD-L1 with surface PD-L1 staining on BD Influx cell sorter (BD Biosciences, BD) at Sanford Consortium for Regenerative Medicine, La Jolla. 30% of the most strongly stained cells were sorted using the gate generated from non-stained infected NALM-6 cells and isotype-control stained infected NALM-6 cells.

FRET Microscopy, image acquisition and analysis. After transfection, adherent cells were cultured for 24 hours in advanced medium (Thermo Fisher Scientific Inc.) without FBS, and plated on glass-bottom dishes (Cell E&G LLC) coated with FN (10 $\mu g \cdot ml^{-1}$) for

overnight before imaging experiment. After transfection, Jurkat cells were cultured for 24 hours in RPMI 1640 medium with 10% FBS, and transferred to glass-bottom dishes (Cell E&G LLC) coated with PLL (10 $\mu g \cdot ml^{-1}$) for about 15 minutes before imaging experiment. During imaging process, cells were maintained at 37°C in a 5% CO_2 and 95% air-humidified chamber. Images were collected by a Nikon Eclipse Ti inverted microscope equipped with a 300 W Xenon lamp (Atlas Specialty Lighting), an electron multiplying (EM) CCD camera (QuantEM:512SC, Photometrics) and a x100 DIC Nikon microscope objective (NA = 1.4) using MetaFluor 7.8.10.0 or MetaMorph 7.8.8.0 software (Molecular Devices, LLC) with a 420DF20 excitation filter, a 455DCXRU dichroic mirror, and two emission filters controlled by a filter changer (480DF40 for ECFP and 535DF25 YPet). All filters and dichroic mirrors were purchased from Chroma Technology Corp. The pixel-by-pixel ratio images of ECFP/FRET were calculated based on the background-subtracted fluorescence intensity images of ECFP and FRET using MetaFluor software. All the ratio images were displayed in the intensity modified display (IMD) mode [170] in which the color and brightness of each pixel is determined by the ECFP/FRET ratio and FRET intensity, respectively. The image analysis was performed using our customized software *fluocell* written in MATLAB (The MathWorks Inc.) [92, 93]. All the images were background-subtracted and smoothed using a median-filter with a window size of 3x3 pixels. For quantifying imaging data of cells with polystyrene particle-bound ligand stimulation, Otsu's method (MATLAB graythresh function) was used to determine threshold and generate mask to separate different regions of interest, including background, cell region and particle region within the cell [171]. Then the background was subtracted for each ECFP or FRET image. The intensity ratio of each

region of interest was calculated and averaged, and the difference between peak intensity ratio and basal intensity ratio was quantified. The percentage of particle region was calculated using particle region mask and cell region mask.

Statistical analysis. D'Agostino-Pearson omnibus normality test was used for the normality test. Data following Gaussian distribution were analyzed by using unpaired two-tailed Student's *t* test with Welch's correction or ordinary one-way ANOVA followed by Bonferroni's multiple comparisons test (Graphpad Prism 6, GraphPad Software) to evaluate the statistical difference between groups. Data not following Gaussian distribution were analyzed by using Mann-Whitney test or Kruskal-Wallis test followed by Dunn's multiple comparison test (Graphpad Prism 6, GraphPad Software). A significant difference was determined by *P* value ($P < 0.05$). Statistical results are presented as mean ± S.E.M. Asterisks indicate critical values (*$P < 0.05$, **$P < 0.01$ and ***$P < 0.001$), and "n.s." indicates no significant difference ($P > 0.05$).

4.4. Results and Discussion

4.4.1. Development and characterization of synthetic molecular machineries

Firstly, I rationally designed iSNAP generally composed of multiple domains as shown in Fig. 4.1.A, including a N-terminal substrate domain, a FRET pair (ECFP and YPet) flanking a flexible linker, a N-terminal SH2 domain, an interdomain A, a C-terminal SH2 domain, an interdomain B and a kinase domain. Based on this design strategy, the N-terminal substrate domain and the C-terminal kinase domain serve as sensing component and activating component of iSNAP respectively. And Fig. 4.1.B, C show iSNAP-ZAP70s and iSNAP-SYK comprising different substrates as their substrate domains. Notably, the internal SH2 domain binds to the N-terminal phosphorylated tyrosine of substrates on iSNAPs as sensing components to triggers the kinase activation and downstream signaling pathways [172, 173], and vice versa. Fig. 4.2 illustrates the general working principle of iSNAPs for ZAP70 and SYK.

Then I constructed different iSNAPs for ZAP70 and SYK as shown in Table 4.1, and characterized them *in vivo* and *in vitro*. Three substrates are selected for iSNAP-ZAP70s, including iSNAP-Z1, iSNAP-Z2 and iSNAP-Z3, and one motif is selected for iSNAP-SYK, i.e. iSNAP-S1. All FF mutants are negative mutants of corresponding iSNAPs, including iSNAP-Z1FF, iSNAP-Z2FF, iSNAP-Z3FF and iSNAP-S1FF.

I began examining iSNAPs for ZAP70 and SYK in HeLa cells and MEFs. Cells were transfected to express different iSNAPs, starved without serum supply and stimulated with different stimulants. FRET responses of iSNAP-expressing cells treated with pervanadate (PVD), a potent tyrosine phosphatase inhibitor [169], are summarized in Fig. 4.3. Among all different iSNAPs, iSNAP-Z1 and iSNAP-S1 showed the largest

FRET responses in HeLa cells. Consistent results for both iSNAP-Z1 and iSNAP-S1 were observed in MEFs by same PVD stimulation. iSNAP-Z2 and iSNAP-Z3 gave decent FRET responses in HeLa cells, although weaker compared with iSNAP-Z1 in HeLa cells. iSNAP-Z1 also gave faster FRET dynamics than iSNAP-Z2 and iSNAP-Z3 in response to PVD stimulation in HeLa cells (Fig. 4.4.A). Together, these observations indicate that three motifs for iSNAPs for ZAP70 and one motif for iSNAP for SYK are all capable to sense upstream phosphorylation signals and exhibit confirmation-dependent FRET responses (Table 4.1). In particular, motif 1 for iSNAP for ZAP70 after phosphorylation may have higher binding affinity towards the tandem SH2 domains of ZAP70 than the other two motifs for iSNAPs for ZAP70. On the other hand, FRET responses were absent in HeLa cells expressing all negative mutants of iSNAPs, in which substrate tyrosine residues are mutated to phenylalanine, indicating FRET responses of iSNAPs require tyrosine phosphorylation of substrate domains as sensing components as designed (Fig. 4.2, Fig. 4.3 and Fig. 4.4.A, B). Moreover, Fig. 4.3 shows stimulation of HeLa cells with EGF or MEFs with PDGF didn't lead to any notable FRET responses of iSNAP-Z1 and iSNAP-S1, which gave the largest FRET responses with PVD stimulation. It suggests that neither EGFR signaling pathway in HeLa cells nor PDGFR signaling pathway in MEFs contribute much to the phosphorylation of the substrates, which may be different from the signaling pathways in T cells. Overall, iSNAP-Z1 and iSNAP-S1 have been demonstrated to have very good sensing capabilities and specificities.

To further characterize iSNAPs, especially assess the performances of activating components, I decided to produce and purify iSNAP-Z1 and iSNAP-Z1FF proteins from

mammalian cells and examine their functions *in vitro*. I first constructed N-terminal His-tagged recombinant iSNAP-ZAP70s as shown in Fig. 4.5, and transfected HEK cells for recombinant protein expression. The desired fusion proteins were captured and purified using immobilized metal ion affinity chromatography by Ni-NTA agarose beads. Then I analyzed FRET dynamics of purified iSNAP-Z1 and iSNAP-Z1FF proteins in response to several different kinases in solution without interference of unpredictable co-factors in cellular environment, in order to verify the function of sensing components. For *in vitro* kinase assays, I chose several SFK members, such as human full-length Src, Fyn and Lck kinases, which are known to be crucial to various T cell signals, for instance TCR triggering on TCR/CD3 complexes [106, 110, 111]. After being phosphorylated by active Src, Fyn or Lck kinases with the addition of ATP *in vitro*, iSNAP-Z1 quickly responded with 65~100% increases of FRET/ECFP emission ratio (Fig. 4.6). On the contrary, only minor FRET responses with quite slow dynamics for iSNAP-Z1FF as negative control were observed (Fig. 4.6), suggesting that FRET responses of iSNAPs *in vitro* are governed by the intramolecular interaction between the tandem SH2 domains and the phosphorylated substrate domain as I designed (Fig. 4.2).

Furthermore, in order to determine the performances of activating components of iSNAPs, I used kinase activity assay to directly measure their kinase activities *in vitro*. As shown in Fig. 4.6 that iSNAP-Z1 with active Fyn kinase had the strongest FRET response, I started doing kinase activity assay with active Fyn kinase (data not shown) but realized active Fyn kinase is His-tagged protein that cannot separate from His-tagged iSNAPs easily. Thus, I decided to use non-His-tagged active Lck kinase for iSNAP kinase activity measurements. Purified iSNAPs were treated with active Lck kinase at 37

^{o}C for one hour and I then used Ni-NTA agarose beads to separate iSNAPs from active Lck kinase before assaying their kinase activities. According to the manufacturer's instruction, the kinase activity assay is a luminescent kinase assay that measures ADP formed from a kinase reaction and the luminescent signal positively correlates with kinase activity. Therefore, kinase activities of iSNAPs were determined by reading corresponding luminescent signals. iSNAP-Z1 showed higher kinase activity (~100% enhancement) after being treated with active Lck kinase, compared with iSNAP-Z1 without active Lck kinase treatment (Table 4.2). Together with observed FRET responses for iSNAP-Z1 (Fig. 4.6), the results from *in vitro* characterization clearly demonstrate kinase activities of activating components are correlated with FRET responses of iSNAPs triggered via the phosphorylation on sensing components.

In addition, apparent kinase activity increase was observed for iSNAP-Z1FF after active Lck kinase treatment (Table 4.2), indicating that besides substrate-mediated activation there must be some other activation mechanisms for iSNAP-ZAP70s. It is known that SYK family kinases (including ZAP70 and SYK) can be activated by phosphorylation of tyrosine residues in the interdomain regions via either Fyn/Lck phosphorylation as activated downstream of SFKs or their own trans-autophosphorylation [111, 115, 174, 175]. In other words, iSNAP-ZAP70s can be activated in an substrate-independent manner via phosphorylation of interdomain tyrosines and release of the activating components. Table 4.2 also shows that the kinase activity of iSNAP-Z1 with Lck treatment is much higher than that of iSNAP-Z1FF with same treatment. This result implicates that iSNAP-Z1 may utilize two independent activation mechanisms together and achieve prolonged and synergistic activation of the

kinase domain. Moreover, the kinase activity of iSNAP-Z1FF with Lck treatment is similar to that of iSNAP-Z1 without Lck treatment. It implies that trans-autophosphorylation or Lck phosphorylation on interdomains may be just enough to maintain certain level of tonic kinase activity for iSNAP-ZAP70s instead of strong and sustained kinase activity generated by substrate phosphorylation.

Taken together, these results from *in vivo* and *in vitro* characterizations strongly suggest that FRET response of iSNAP-Z1 depends on the tyrosine phosphorylation of its sensing component and kinase activity of iSNAP-Z1 relies on the release of its activating component. FRET response and full activation of iSNAP-Z1 are correlated with each other in an substrate-dependent manner. These conclusions may be generally applicable to other iSNAP-ZAP70s and iSNAP-SYK.

4.4.2. Engineering T cells for overcoming PD-1/PD-L1 signaling mediated T cell inhibition via synthetic molecular machineries

Since iSNAP-Z1 and iSNAP-S1 are identified to have best performances, I next constructed different PD-1 fused iSNAPs (PD-1-iSNAPs, Table 4.3) by fusing those optimal iSNAPs to the cytoplasmic tail of human PD-1 receptor, so as that I could apply these synthetic molecular machineries into T cells to reprogram their functions and behaviors for overcoming T cell exhaustion via rewiring PD-1 co-inhibitory signaling with TCR activation signaling. As shown in Fig. 4.7, I constructed PD-1-iSNAPs for ZAP70 following two different strategies, fusing iSNAPs to the C terminus of full-length human PD-1 (FL-PD-1, Fig. 4.7.A) or truncated human PD-1 (T-PD-1, Fig. 4.7.B). The deleted sequence for T-PD-1 part includes immunoreceptor tyrosine-based inhibition motif (ITIM) and immunoreceptor tyrosinebased switch motif (ITSM), which are critical

for the inhibitory function of PD-1 receptor [126, 176]. Particularly, ITSM is already known to recruit the tyrosine phosphatase and this recruitment event leads to downstream suppression of immune cell activation and functions.

I then started testing PD-1-iSNAPs for ZAP70 and SYK (Fig. 4.8) in different cells. Cells were transfected to express different iSNAPs, starved without serum supply and stimulated with PVD. Fig. 4.9.A summarizes FRET responses of iSNAP-expressing HeLa cells in response to PVD stimulation, including full-length human PD-1 and truncated human PD-1 fused iSNAP-ZAP70s. Among all different PD-1-iSNAP-ZAP70s, T-PD-1-iSNAP-Z1 and FL-PD-1-iSNAP-Z1 showed the largest FRET responses in HeLa cells. FRET response was absent in HeLa cells expressing the negative mutant T-PD-1-iSNAP-Z1FF, in which substrate tyrosine residues are mutated to phenylalanine, indicating FRET responses of T-PD-1-iSNAP-Z1 require tyrosine phosphorylation of substrate domains as sensing components as designed (Fig. 4.8 and Fig. 4.9.A). Notably, FL-PD-1-iSNAP-Z1FF as the negative control for FL-PD-1-iSNAP-Z1 showed some FRET/ECFP emission ratio increase upon PVD stimulation, suggesting the ITIM or/and ITSM of PD-1 intracellular domain could be phosphorylated and then elevate FRET efficiency of FL-PD-1-iSNAP-Z1FF via binding to the tandem ZAP70 SH2 domains (Fig. 4.9.A and Fig. 4.10.A). Together, these results suggest that T-PD-1-iSNAP-Z1 gives the highest FRET response according to the design principle (Fig. 4.2). On the other hand, much weaker FRET response was observed in T-PD-1-iSNAP-S1 group than either T-PD-1-iSNAP-Z1 or FL-PD-1-iSNAP-Z1 group subjected to PVD stimulation and opposite FRET response was shown in the T-PD-1-iSNAP-S1FF group (Fig. 4.9.B

and Fig. 4.10.B). It would require further studies on why the unexpected FRET ratio reduction in T-PD-1-iSNAP-S1FF group happens upon PVD stimulation.

Again, consistent FRET response upon PVD stimulation was observed in Jurkat cells expressing T-PD-1-iSNAP-Z1 and negative control group T-PD-1-iSNAP-Z1FF showed almost no FRET response in Jurkat cells stimulated with PVD (Fig. 4.11). Together with the results in HeLa cells above, these confirm that tyrosine phosphorylation on sensing component is necessary for FRET responses of T-PD-1 fused iSNAP-ZAP70s.

I further decided to use more specific stimulants to examine PD-1 fused iSNAP-ZAP70s' performances and I chose the major PD-1 ligand, human PD-L1, as the physiological stimulant. First, I constructed a plasmid for human PD-L1 expression in mammalian cells so that I could produce and purify PD-L1 from HEK cells (see "4.3 Materials and Methods" section for more details). After PD-L1 purification, I did biotinylation for purified PD-L1 and validated by protein gel electrophoresis (Fig. 4.12), and made particle-bound PD-L1 via biotin-streptavidin binding. With particle-bound PD-L1, I examined different PD-1 fused iSNAP-ZAP70s in HeLa cells and Jurkat cells. In HeLa cells expressing T-PD-1-iSNAP-Z1, I again observed consistent strong FRET response, which very colocalizes with particle-bound PD-L1, but HeLa cells expressing negative control group T-PD-1-iSNAP-Z1FF showed very minor FRET response (Fig. 4.14 and Fig. 4.15). For FL-PD-1-iSNAP-Z1 group, HeLa cells gave a lot lower FRET response compared to HeLa cells transfected with T-PD-1-iSNAP-Z1 (Fig. 4.15). FL-PD-1-iSNAP-Z1FF group gave stronger FRET response than T-PD-1-iSNAP-Z1FF group but weaker response than FL-PD-1-iSNAP-Z1 group (Fig. 4.15). Taken together, there

results confirm that tyrosine phosphorylation on sensing component is necessary for FRET responses of T-PD-1 fused iSNAP-ZAP70s, but not FL-PD-1 fused iSNAP-ZAP70s, and T-PD-1 fused iSNAP-ZAP70s respond better than FL-PD-1 fused iSNAP-ZAP70s under PD-1 ligand engagement. In addition, FRET response observed under particle-bound ligand stimulation is very localized, which is quite different from global FRET response observed under PVD stimulation. It indicates that PD-1 fused iSNAP-ZAP70s can very specifically detect the binding events between PD-1 receptor and its ligand as designed (Fig. 4.13). One interesting observation is that T-PD-1-Z1FF group showed some minor local FRET response to particle-bound ligand stimulation, which is stronger than FRET response in T-PD-1-Z1FF group stimulated by PVD (Fig. 4.9.A, Fig. 4.14 and Fig. 4.15). This is unexpected according to the design principle, and could happen because T-PD-1 fused iSNAP-ZAP70s can respond to the clustering of PD-1 receptor and its ligand on the cell surface in an substrate-independent manner via phosphorylation of interdomain tyrosines, and give FRET response upon subsequent intramolecular conformational changes and possibly release of activating domain as shown in the *in vitro* assay described above. Furthermore, I tested how T-PD-1 fused iSNAP-ZAP70s could perform in Jurkat cells in response to PD-1 ligand stimulation. As shown in Fig. 4.16 and Fig. 4.17, Jurkat cells expressing T-PD-1-iSNAP-Z1 showed clear local FRET response, while T-PD-1-iSNAP-Z1FF gave much lower FRET response. It again confirms that T-PD-1 fused ZAP70s respond to PD-1 ligand specifically and T-PD-1-iSNAP-Z1FF may employ the substrate-independent mechanism to generate FRET response (Fig. 4.17) and possibly further activate its activating component. Thus, I demonstrate that PD-1 fused iSNAP-ZAP70s can respond well to the clustering of PD-1

receptor and its ligand on the cell membrane to generate FRET responses, possibly via two different mechanisms, i.e. sensing component tyrosine phosphorylation dependent and interdomain tyrosine phosphorylation dependent modes. Moreover, the tail of PD-1 intracellular domain could interfere with the sensing component via binding to the tandem ZAP70 SH2 domains and reduce the performance of FL-PD-1 fused ZAP70s, and thus T-PD-1 fused ZAP70s are generally better in this respect.

After characterizing PD-1 fused iSNAP-ZAP70s in HeLa and Jurkat cells with PVD or PD-1 ligand as stimulant, I shifted my focus more towards assessing their activating performances under co-culture with PD-L1-expressing cells. First, I constructed and produced virus for human PD-L1 so as to infect HEK cells to generate PD-L1-expressing cell line as APCs. However, infected HEK cells didn't give me a relatively uniform PD-L1 expression (data not shown). I decided to test some other solid tumor cell lines, including ASPC-1, MDA-MB-231 and PC-3 cell lines. These cell lines are reported to have strong surface PD-L1 expression, especially after human interferon-gamma (IFN-γ) treatment [177]. I used anti-human PD-L1 antibody to stain these cells both with and without IFN-γ treatment and measured the surface PD-L1 expression by flow cytometry, and MDA-MB-231 cell line gave the strongest PD-L1 surface expression after 24 hour IFN-γ treatment. I hence chose IFN-γ-pretreated MDA cells as optimal APCs to co-culture with Jurkat cells so as to assess T-PD-1 fused iSNAP-ZAP70s' activation performance via T cell activation assay, and CD69 as very early T cell activation marker on the T cell surface was chosen to determine T cell activation (Fig. 4.18). With different T-PD-1 fused iSNAP-ZAP70s introduced into Jurkat cells, they were co-cultured with IFN-γ-treated MDA cells for 24 hours before doing surface

staining and measurement for CD69 in Jurkat cells by flow cytometry. The results show that Jurkat cells expressing T-PD-1-iSNAP-Z1 or T-PD-1-iSNAP-Z1FF without MDA cell co-culture showed weak CD69 activation (Fig. 4.19) and non-transfected Jurkat cells with or without MDA cell co-culture gave even lower CD69 expression level (data not shown). On the other hand, Jurkat cells expressing T-PD-1-iSNAP-Z1 with MDA cell co-culture got strongly activated (Fig. 4.19). It implies that the specific recognition of PD-L1 by T-PD-1 fused iSNAP-ZAP70s are required for T cells to positively respond and get activated against PD-L1-expressing tumor cells. Jurkat cells expressing T-PD-1-iSNAP-Z1FF with MDA cell co-culture also showed quite strong T cell activation, suggesting that T-PD-1 fused iSNAP-ZAP70s could get activated in a sensing component independent manner. Taking these together with *in vitro* assay and FRET imaging results above, it strongly suggests that T-PD-1-iSNAP-ZAP70s may utilize two independent activation mechanisms together so as to achieve prolonged and synergistic activation of the kinase domain, including interdomain tyrosine phosphorylation dependent and substrate phosphorylation dependent modes (Fig. 4.20).

In particular, the interdomain tyrosine phosphorylation dependent mode may require to during local clustering of T-PD-1 fused iSNAP-ZAP70s and PD-1 ligand on the cell membrane so as that T-PD-1 fused iSNAP-ZAP70s could get proximally close to each other and trans-autophosphorylation on their interdomains could happen as shown in Fig. 4.20 mode B. The results that FRET response was absent for T-PD-1-iSNAP-Z1FF group in HeLa and Jurkat cells upon PVD stimulation also support the model described, since PVD stimulation can trigger substrate phosphorylation as shown in Fig. 4.20 mode A but not local clustering of T-PD-1 fused iSNAP-ZAP70s as PD-1 ligand does.

Therefore, by introducing extra distance to separate activating component further apart from the T-PD-1 part on the cell membrane, it may weaken the effect from local clustering caused by T-PD-1 fused iSNAP-ZAP70s and PD-1 ligand and make T-PD-1 fused iSNAP-ZAP70s become more substrate phosphorylation dependent. As shown in Fig. 4.21, I decided to insert extra internal linker between sensing component and FRET pair or between T-PD-1 part and sensing component in order to see how T-PD-1 fused iSNAP-ZAP70s' performance would be affected. The linkers I chose include a flexible 17 amino acid linker and a 116 amino acid linker [56]. Among those different T-PD-1 fused iSNAP-ZAP70s with extra internal linkers, the one with 166 aa linker insertion between T-PD-1 part and sensing component, i.e. T-PD-1 fused LL-iSNAP-ZAP70s, worked best by giving much stronger CD69 activation in T-PD-1-LL-iSNAP-Z1 group than T-PD-1-LL-iSNAP-Z1FF group (T-LL-Z1 and T-LL-Z1FF in Fig. 4.19), indicating that separating iSNAP-ZAP70s further away from T-PD-1 part on the cell membrane can better differentiate the activating capability between T-PD-1-LL-iSNAP-Z1 and T-PD-1-LL-iSNAP-Z1FF and thus make T-PD-1 fused iSNAP-ZAP70s become more substrate phosphorylation dependent via their sensing components as designed. Therefore, upon the clustering between PD-1 and PD-L1, synthetic molecular machineries, i.e. T-PD-1 fused iSNAP-ZAP70s, can successfully sense the negative input signal via their sensing components and rewire it into the positive output signals via their activating components.

In summary, I successfully developed iSNAPs for ZAP70 and SYK by harnessing the naturally occurring mechanism of tyrosine kinase regulation and characterized them in respect of their sensing and activating functions *in vitro* and *in vivo*. In particular, I successfully proved that iSNAP-ZAP70s can detect the input signal via their sensing

components, exhibit confirmation-dependent FRET ratio changes, and give rise to desirable increase in ZAP70 kinase activity. I then connected optimal iSNAP-ZAP70s to PD-1 receptor and applied PD-1 fused iSNAP-ZAP70s into different cells to further demonstrate their sensing and activating functions after being rewired into PD-1 co-inhibitory signaling pathway. Particularly, introducing these molecular machinery proteins enables T cells to get activated upon negative input signal through PD-1 and its ligand. These indeed help to overcome PD-1/PD-L1 signaling-mediated T cell inhibition.

4.5. Conclusion

CAR T-cell therapy based on cellular engineering by synthetic biology approaches has been proven to be effective to treat blood cancers, but it is still uncertain whether such successful therapeutic approach could be applied to treat other types of tumors with decent clinical efficacy. PD-1/PD-L1 signaling-mediated inhibition of T cell functions has been found to be one major hurdle when using CAR T-cell therapy to treat solid tumors. To tackle the challenge of PD-1/PD-L1 co-inhibitory signaling mediated cancer immune evasion, I was inspired by both T cell receptor-mediated activation signal and immune checkpoint receptor PD-1-mediated co-inhibitory signal, and decided to employ synthetic biology approaches to rewire co-inhibitory signaling with TCR activation signaling via synthetic molecular machineries called iSNAPs. In this study, the results indicates that iSNAPs are able to detect the specific input kinase phosphorylation signals and generate the subsequent active kinase output signals via their activating components, especially ZAP70. After iSNAP-ZAP70s being connected to PD-1 receptor, they can convert the negative input signal via PD-1/PD-L1 into the positive output signals via ZAP70 kinase upon the ligation between PD-1 and PD-L1 between T

cell and PD-1-expressing tumor cells. The activation signals from iSNAP-ZAP70s can further activate the downstream signaling events for T cell activation, which in turn contributes to overcoming PD-1/PD-L1 signaling-mediated T cell inhibition and reacting against solid tumors better. Moreover, I demonstrate these proof-of-concept molecular machineries provide a new class of cancer therapeutic tools, which could be broadly used to engineer immune cell functions and behaviors for better cancer treatment. The combination of CAR and iSNAP-ZAP70-based T cell therapeutic approaches may harness potential synergies and open a new avenue for future next generation T cell therapies.

4.6. Figures and Tables

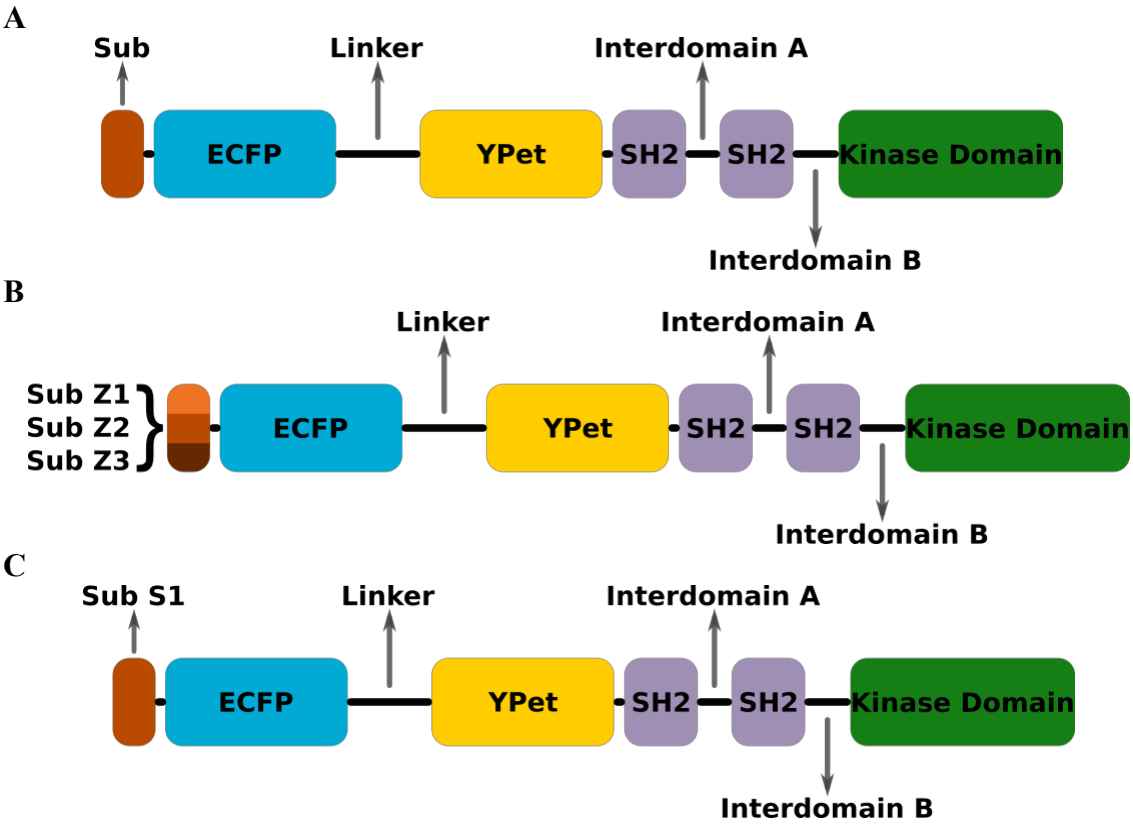

Figure 4.1: The general domain organization of integrated sensing and activating proteins (iSNAPs) for ZAP70 and SYK.

(**A**) The general domain organization of iSNAPs. Schematic representation shows domain organization and main motifs of iSNAPs. A N-terminal substrate domain as sensing component shown in brown is linked to a FRET pair (ECFP in cyan and YPet in yellow) flanking a flexible linker. The C-terminal part is divided into five domains, a N-terminal SH2 domain (purple), an interdomain A, a C-terminal SH2 domain (purple), an interdomain B and a kinase domain (green) as activating component. (**B**) The domain organizations of iSNAP-ZAP70s with different substrates from CD3 chain of TCR/CD3 complex. (**C**) The domain organization of iSNAP-SYK with one substrate from CD3 chain of TCR/CD3 complex.

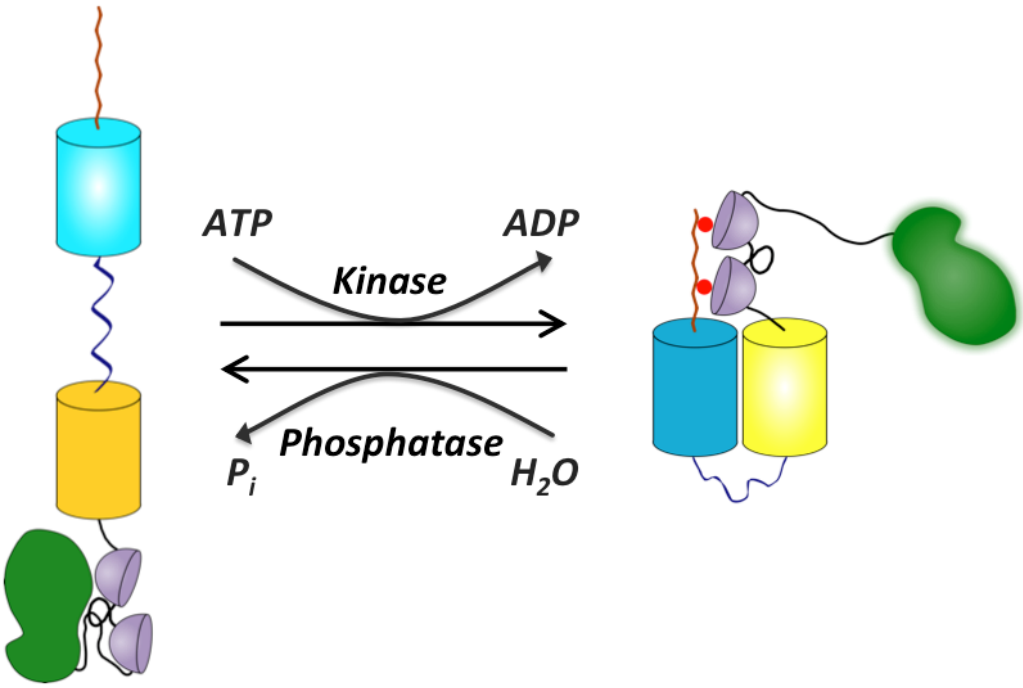

Figure 4.2: The general working principle of iSNAPs for ZAP70 and SYK.

The general working principle of iSNAPs. The active kinase, such as Lck/Fyn kinase, can phosphorylate the sensing component of iSNAPs, which subsequently binds to intramolecular tandem SH2 domains. This binding event results in the conformational change and FRET efficiency increase of iSNAPs, and simultaneously activates iSNAPs from the autoinhibition by releasing the activating component. Dephosphorylating the phosphorylated sensing component by phosphatase can reverse the process.

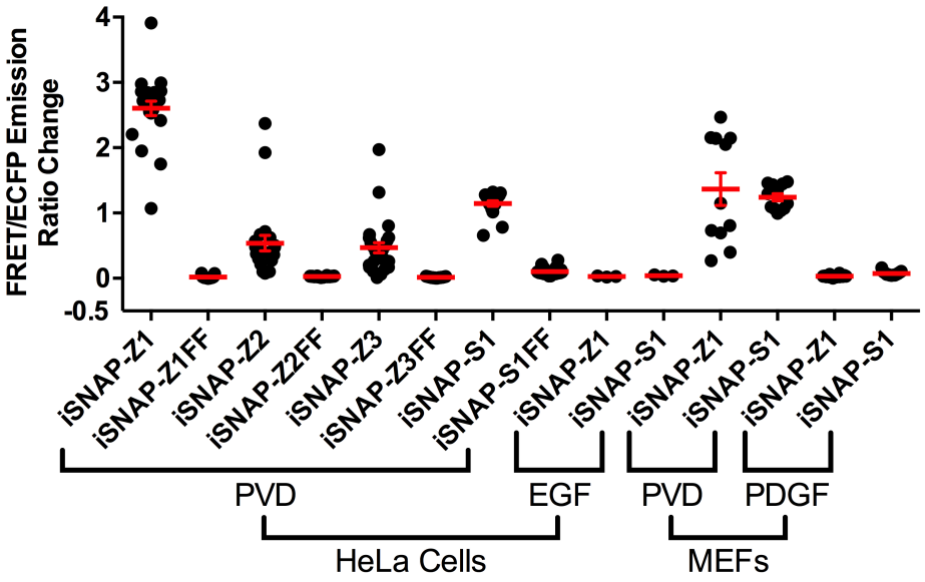

Figure 4.3: The FRET responses of iSNAPs for ZAP70 and SYK in response to different stimulants in living mammalian cells.

The FRET responses of different iSNAPs for ZAP70 and SYK in HeLa cells and MEFs stimulated with 50 ng/mL EGF (epidermal growth factor) or 50 ng/mL PDGF (platelet-derived growth factor) or 20 μM PVD (pervanadate, tyrosine phosphatase inhibitor). iSNAP-ZAP70s include iSNAP-Z1, iSNAP-Z2, iSNAP-Z3 and the corresponding negative control FF mutants, and iSNAP-SYKs include iSNAP-S1 and iSNAP-S1FF. n = 23, 25, 22, 18, 27, 19, 18, and 26 HeLa cells with PVD stimulation for iSNAP-Z1, iSNAP-Z1FF, iSNAP-Z2, iSNAP-Z2FF, iSNAP-Z3, iSNAP-Z3FF, iSNAP-S1 and iSNAP-S1FF, respectively. n = 3 HeLa cells with EGF stimulation for both iSNAP-Z1 and iSNAP-S1. n = 11 and 12 MEF cells with PVD stimulation for iSNAP-Z1 and iSNAP-S1, respectively. n = 12 and 13 MEF cells with PDGF stimulation for iSNAP-Z1 and iSNAP-S1, respectively. In scatter plots, the red lines indicate the mean values, the error bars represent the standard error of the mean (S.E.M.) and average data are presented as mean ± S.E.M.

A

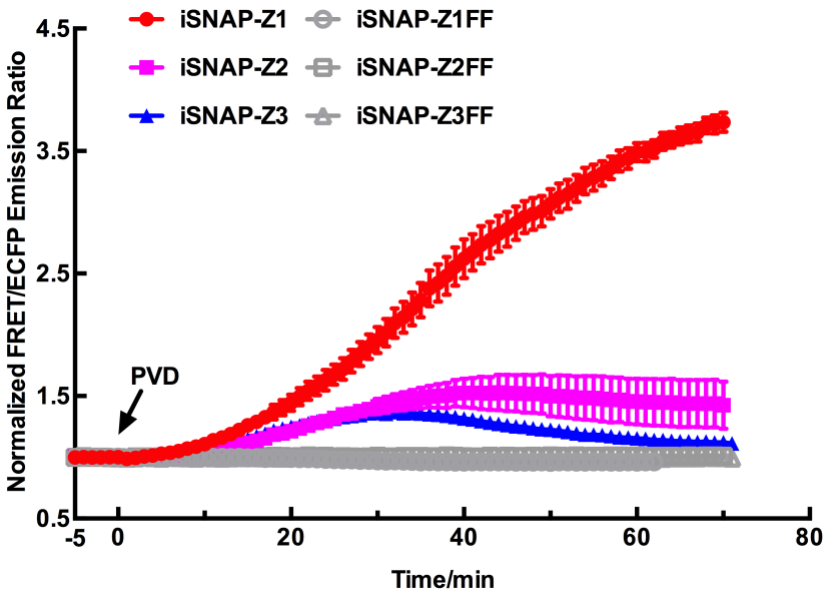

B

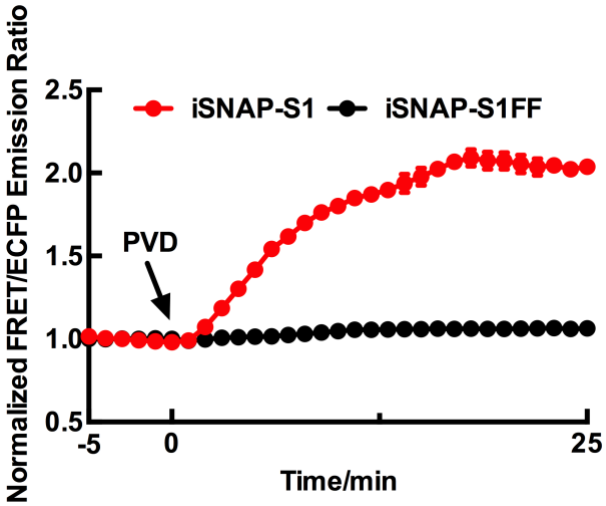

Figure 4.4: The normalized emission ratio time courses of different iSNAPs for ZAP70 and SYK in response to pervanadate (PVD) stimulation in HeLa cells.

(**A**) The time courses of normalized average FRET/ECFP emission ratios of iSNAP-Z1 (red solid circles, n = 18), iSNAP-Z1FF (open circles, n = 20), iSNAP-Z2 (magenta solid squares, n = 14), iSNAP-Z2FF (open squares, n = 18), iSNAP-Z3 (blue solid triangles, n = 16), and iSNAP-Z3FF (open triangles, n = 19) in HeLa cells before and after 20 μM PVD stimulation (arrow at 0 min). (**B**) The time courses of normalized average FRET/ECFP emission ratios of iSNAP-S1 (red solid circles, n = 15) and iSNAP-S1FF (black solid circles, n = 22) in HeLa cells before and after 20 μM PVD stimulation (arrow at 0 min). (**A-B**) FRET/ECFP emission ratios are normalized against the average values

Figure 4.4: The normalized emission ratio time courses of different iSNAPs for ZAP70 and SYK in response to pervanadate (PVD) stimulation in HeLa cells, Continued

before PVD stimulation. The error bars represent the standard error of the mean (S.E.M.). Average data are presented as mean ± S.E.M.

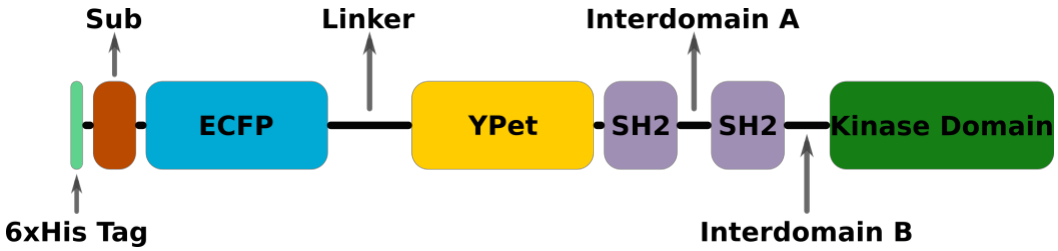

Figure 4.5: The domain organization of His-tagged iSNAPs for ZAP70 and SYK.

The general domain organization of His-tagged iSNAPs for ZAP70 and SYK. Schematic representation shows domain organization and main motifs of His-tagged iSNAPs. A short 6xHis tag is fused at the N-terminal of iSNAPs, and a substrate domain as sensing component shown in brown is linked to a FRET pair (ECFP in cyan and YPet in yellow) flanking a flexible linker. The C-terminal part is divided into five domains, a N-terminal SH2 domain (purple), an interdomain A, a C-terminal SH2 domain (purple), an interdomain B and a kinase domain (green) as activating component.

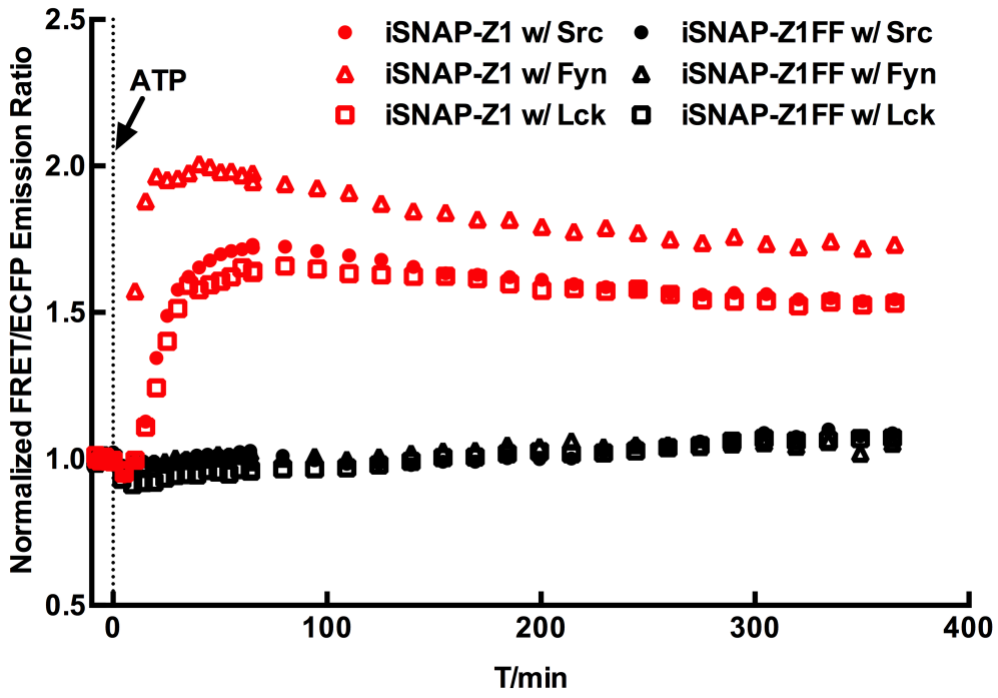

Figure 4.6: Characterization of iSNAP-ZAP70s *in vitro*.

The time courses of normalized FRET/ECFP emission ratios of iSNAP-ZAP70s (iSNAP-Z1 and iSNAP-Z1FF, 1 μM) before and after phosphorylation by the Src, Fyn or Lck kinase *in vitro* (arrow at 0 min with ATP addition, solid red circles for iSNAP-Z1 with Src kinase, black solid circles for iSNAP-Z1FF with Src kinase, red open triangles for iSNAP-Z1 with Fyn kinase, black open triangles for iSNAP-Z1FF with Fyn kinase, red open squares for iSNAP-Z1 with Lck kinase and black open squares for iSNAP-Z1FF with Lck kinase). FRET/ECFP emission ratios are normalized against the average values before the Src kinase was added.

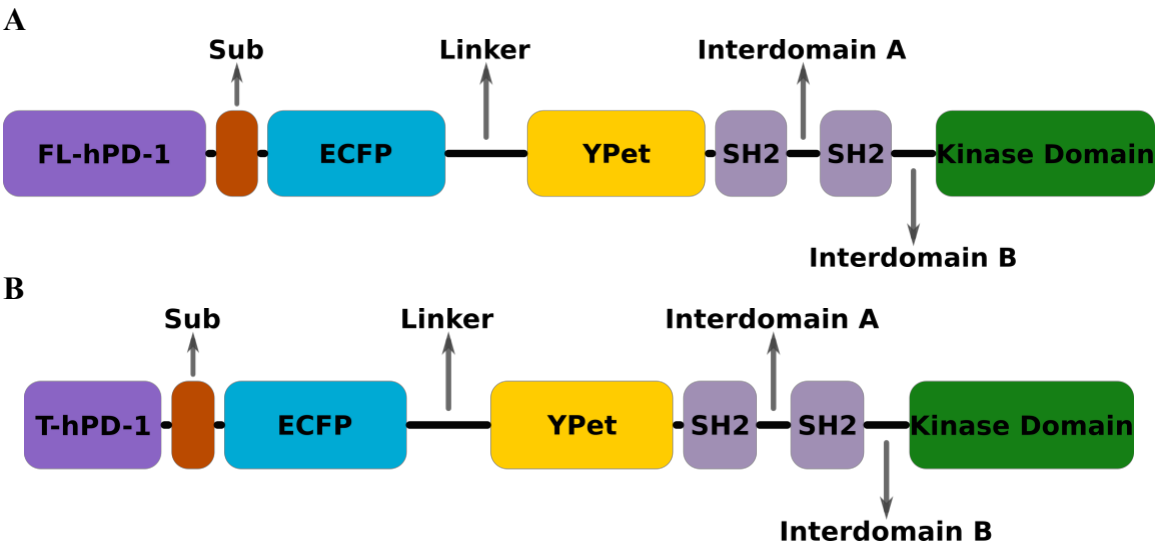

Figure 4.7: The domain organization of different human PD-1 fused iSNAPs for ZAP70 and SYK.

(**A-B**) The general domain organization of human PD-1 fused iSNAPs for ZAP70 and SYK. Schematic representation shows domain organization and main motifs of human PD-1 fused iSNAPs. Full-length PD-1 (FL-PD-1) or truncated PD-1 (T-PD-1) is fused at the N-terminal of iSNAPs, and a substrate domain as sensing component shown in brown is linked to a FRET pair (ECFP in cyan and YPet in yellow) flanking a flexible linker. The C-terminal part is divided into five domains, a N-terminal SH2 domain (purple), an interdomain A, a C-terminal SH2 domain (purple), an interdomain B and a kinase domain (green) as activating component.

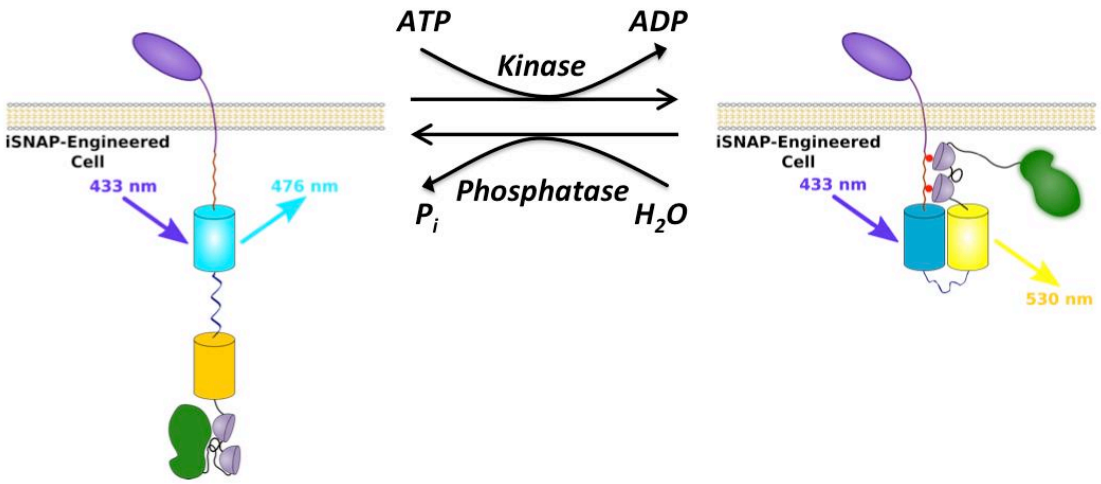

Figure 4.8: The general working principle of truncated human PD-1 fused iSNAPs for ZAP70 and SYK in living mammalian cells.

The schematic diagram of the general working principle of truncated PD-1 fused iSNAPs (T-PD-1-iSNAPs) on the membrane of living mammalian cells. The active kinase, such as Lck/Fyn kinase, can phosphorylate the sensing component of T-PD-1-iSNAPs, which subsequently binds to intramolecular tandem SH2 domains. This binding event results in the conformational change and FRET efficiency increase of iSNAPs, and simultaneously activates iSNAPs from the autoinhibition by releasing the activating component. Dephosphorylating the phosphorylated sensing component by phosphatase can reverse the process.

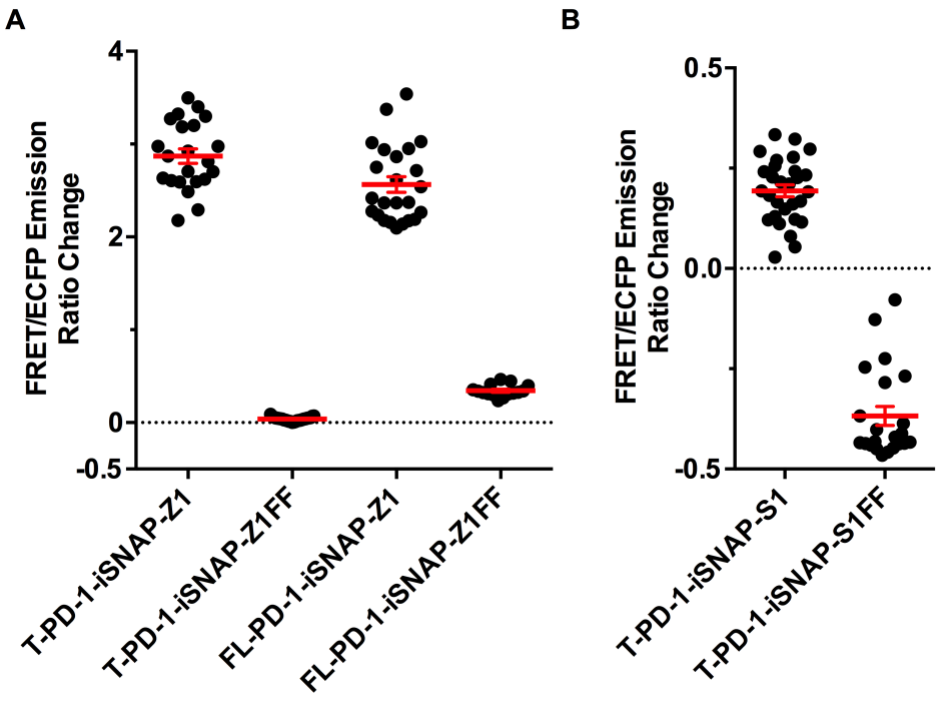

Figure 4.9: The FRET responses of different human PD-1 fused iSNAPs for ZAP70 and SYK in response to pervanadate (PVD) stimulation in HeLa cells.

The FRET responses of different human PD-1 fused iSNAPs for ZAP70 and SYK in HeLa cells stimulated with 20 μM PVD. PD-1 fused iSNAP-ZAP70s include T-PD-1-iSNAP-Z1, FL-PD-1-iSNAP-Z1 and the corresponding negative control T-PD-1-iSNAP-Z1FF, FL-PD-1-iSNAP-Z1FF. PD-1 fused iSNAP-SYKs include T-PD-1-iSNAP-S1 and T-PD-1-iSNAP-S1FF. T-PD-1 and FL-PD-1 represent truncated PD-1 and full-length PD-1, respectively. n = 22, 27, 24, 15, 29 and 22 HeLa cells with PVD stimulation for T-PD-1-iSNAP-Z1, T-PD-1-iSNAP-Z1FF, FL-PD-1-iSNAP-Z1, FL-PD-1-iSNAP-Z1FF, T-PD-1-iSNAP-S1 and T-PD-1-iSNAP-S1FF, respectively. In scatter plots, the red lines indicate the mean values, the error bars represent the standard error of the mean (S.E.M.) and average data are presented as mean ± S.E.M.

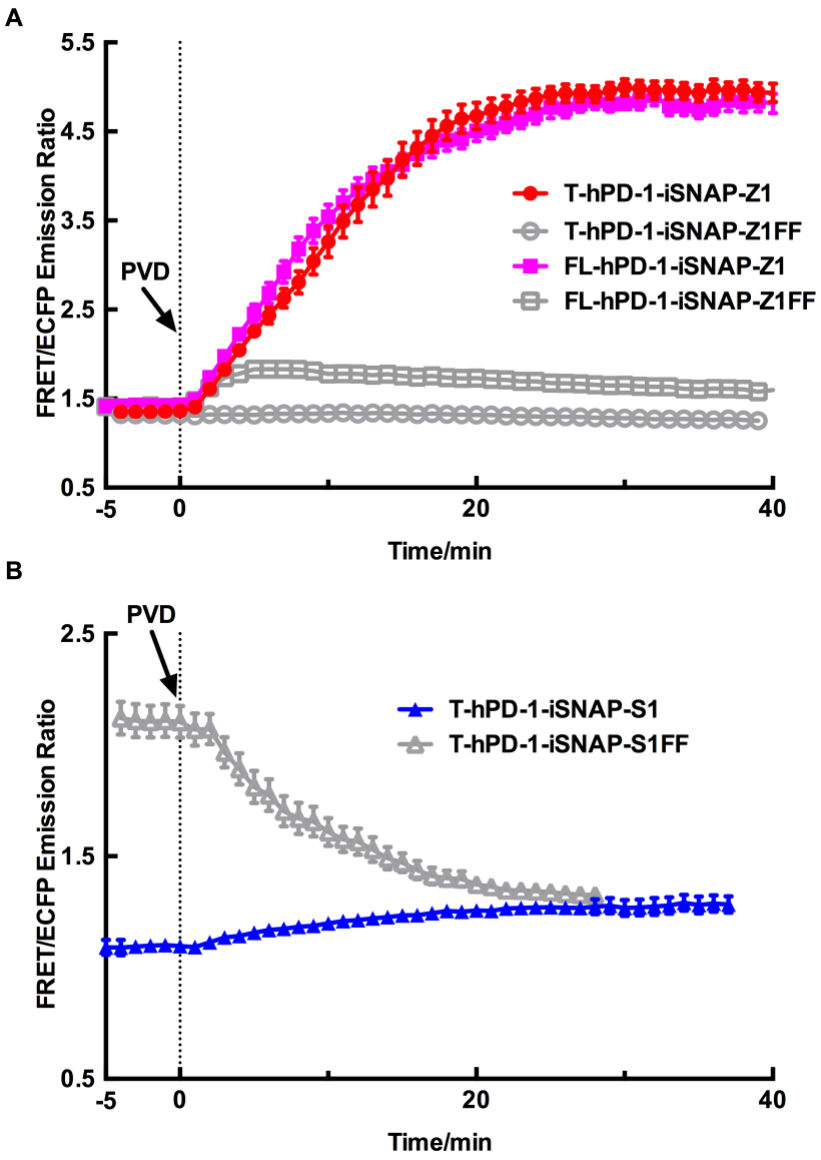

Figure 4.10: The emission ratio time courses of different human PD-1 fused iSNAPs for ZAP70 and SYK in response to pervanadate (PVD) stimulation in HeLa cells.

(**A**) The time courses of average FRET/ECFP emission ratios of T-PD-1-iSNAP-Z1 (red solid circles, n = 22), T-PD-1-iSNAP-Z1FF (open circles, n = 27), FL-PD-1-iSNAP-Z1 (magenta solid squares, n = 24) and FL-PD-1-iSNAP-Z1FF (open squares, n = 15) in HeLa cells before and after 20 μM PVD stimulation (arrow at 0 min). (**B**) The time courses of average FRET/ECFP emission ratios of T-PD-1-iSNAP-S1 (blue solid triangles, n = 29) and T-PD-1-iSNAP-S1FF (open triangles, n = 22) in HeLa cells before and after 20 μM PVD stimulation (arrow at 0 min). (**A-B**) T-PD-1 and FL-PD-1 represent truncated PD-1 and full-length PD-1, respectively. FRET/ECFP emission ratios are normalized against the average values before PVD stimulation. The error bars represent the standard error of the mean (S.E.M.). Average data are presented as mean ± S.E.M.

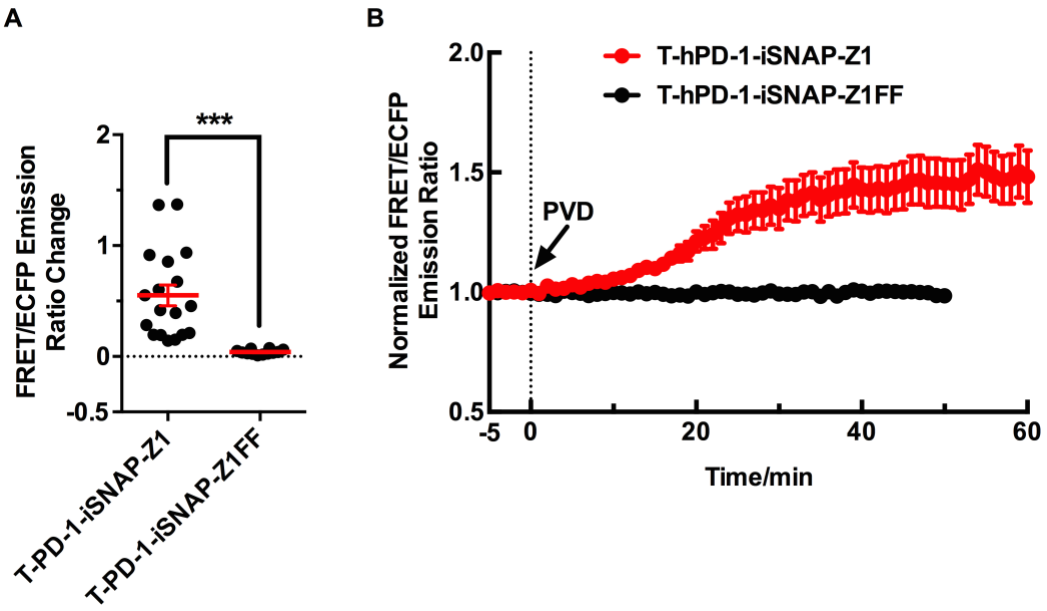

Figure 4.11: Performances of truncated human PD-1 fused iSNAP-ZAP70s in Jurkat cells under pervanadate (PVD) stimulation.

(**A**) The FRET responses of truncated human PD-1 fused iSNAPs for ZAP70 in Jurkat cells stimulated with 20 μM PVD. T-PD-1 represents truncated PD-1. n = 18 and 12 Jurkat cells with PVD stimulation for T-PD-1-iSNAP-Z1 and T-PD-1-iSNAP-Z1FF, respectively. In scatter plots, the red lines indicate the mean values, the error bars represent the standard error of the mean (S.E.M.) and average data are presented as mean ± S.E.M. (**B**) The time courses of normalized average FRET/ECFP emission ratios of T-PD-1-iSNAP-Z1 (red solid circles, n = 18) and T-PD-1-iSNAP-S1FF (black solid circles, n = 12) in Jurkat cells before and after 20 μM PVD stimulation (arrow at 0 min). FRET/ECFP emission ratios are normalized against the average values before PVD stimulation. The error bars represent S.E.M. and average data are presented as mean ± S.E.M.

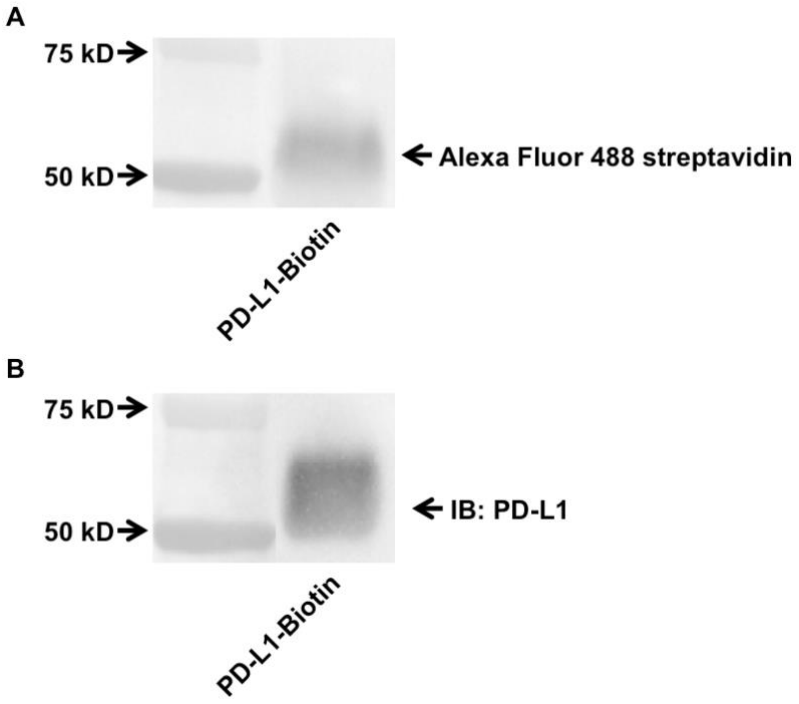

Figure 4.12: Confirmation of biotinylated purified PD-L1 by protein gel electrophoresis.

Blotting results of biotinylated PD-L1 by Alexa Fluor 488 streptavidin (**A**) and by anti-human PD-L1 antibody (**B**). The size of biotinylated PD-L1 is about 50 kDa.

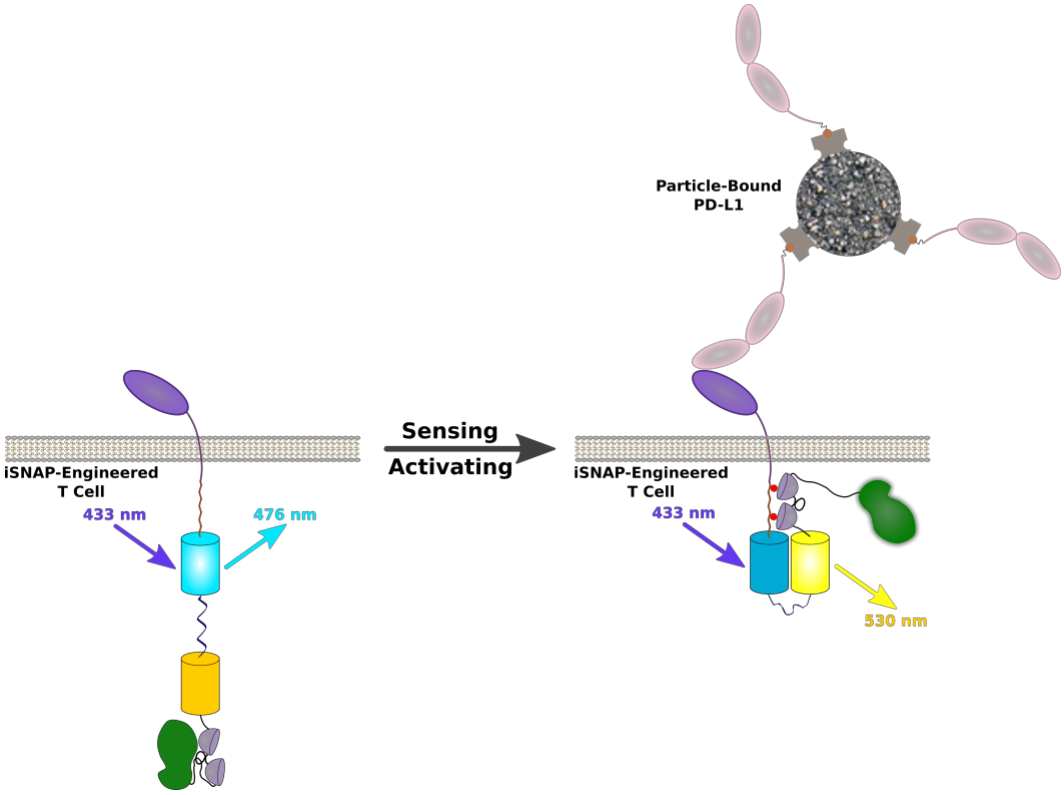

Figure 4.13: The working principle of truncated human PD-1 fused iSNAP-Z1 in living mammalian cells upon PD-L1 ligation.

The schematic diagram of the working principle of truncated PD-1 fused iSNAP-Z1 (T-PD-1-iSNAP-Z1) on the membrane of living mammalian cells treated with particle-bound PD-L1. Upon PD-1 and PD-L1 ligation, the sensing component of T-PD-1-iSNAPs gets phosphorylated and subsequently binds to intramolecular tandem SH2 domains. This binding event results in the conformational change and FRET efficiency increase of iSNAPs, and simultaneously activates iSNAPs from the autoinhibition by releasing the activating component.

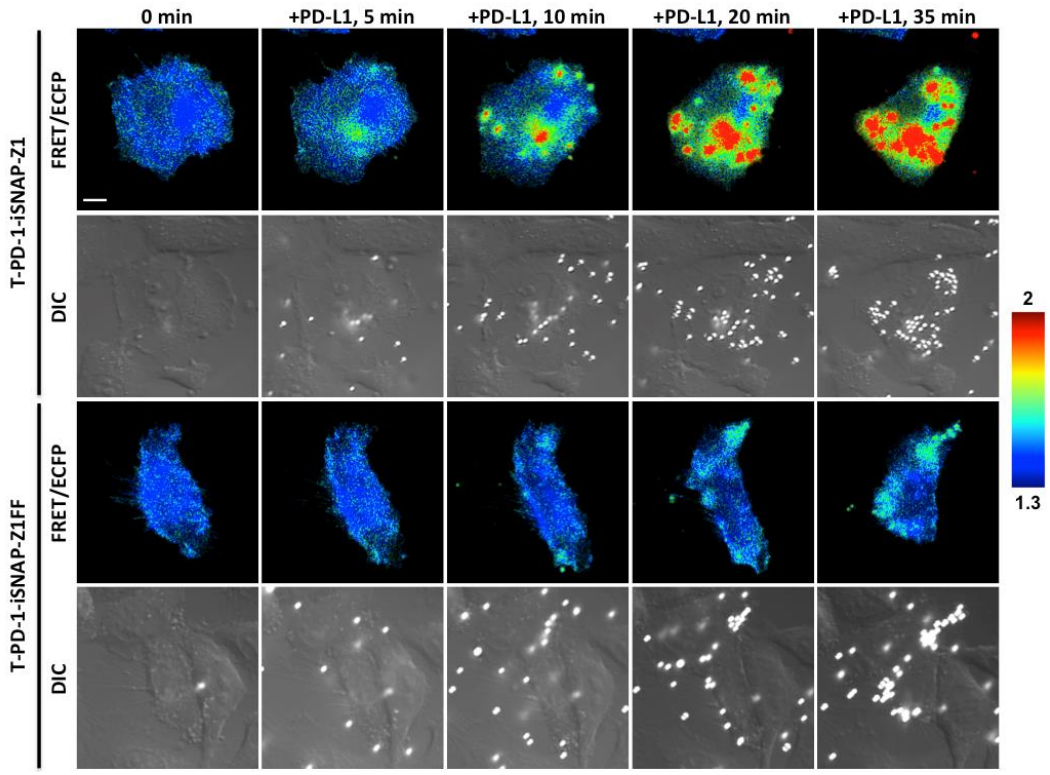

Figure 4.14: Time-lapse imaging in HeLa cells expressing truncated PD-1 fused iSNAP-ZAP70s in response to particle-bound PD-L1.

Time-lapse FRET imaging in HeLa cells expressing truncated PD-1 fused iSNAP-ZAP70s (T-PD-1-iSNAP-Z1 or T-PD-1-iSNAP-Z1FF) upon particle-bound PD-L1 stimulation. FRET/ECFP ratio images of HeLa cells expressing T-PD-1-iSNAP-ZAP70s at the indicated time points are shown in intensity-modulated display mode, and corresponding DIC channel images are shown below FRET/ECFP ratio images. The color scale bar at the right shows the range of FRET/ECFP emission ratio, with cool and warm colors representing low and high ratios, respectively. Scale bars, 5 μm.

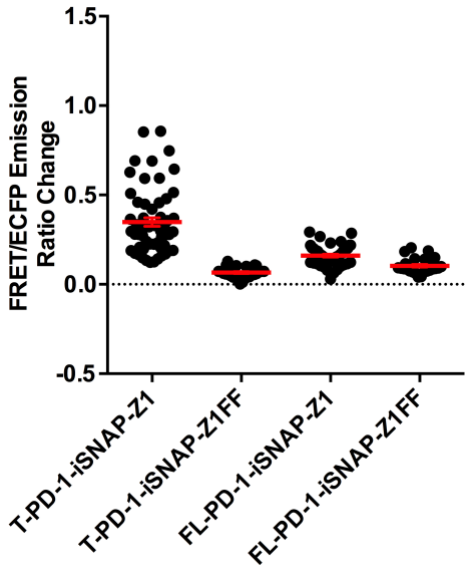

Figure 4.15: The FRET responses of different human PD-1 fused iSNAPs for ZAP70 in response to particle-bound PD-L1 in HeLa cells.

The FRET responses of different human PD-1 fused iSNAPs for ZAP70 in HeLa cells upon particle-bound PD-L1 stimulation. PD-1 fused iSNAP-ZAP70s include T-PD-1-iSNAP-Z1, FL-PD-1-iSNAP-Z1 and the corresponding negative control T-PD-1-iSNAP-Z1FF, FL-PD-1-iSNAP-Z1FF. T-PD-1 represents truncated PD-1. n = 58, 30, 47 and 28 HeLa cells with particle-bound PD-L1 stimulation for T-PD-1-iSNAP-Z1, T-PD-1-iSNAP-Z1FF, FL-PD-1-iSNAP-Z1 and FL-PD-1-iSNAP-Z1FF, respectively. In scatter plots, the red lines indicate the mean values, the error bars represent the standard error of the mean (S.E.M.) and average data are presented as mean ± S.E.M.

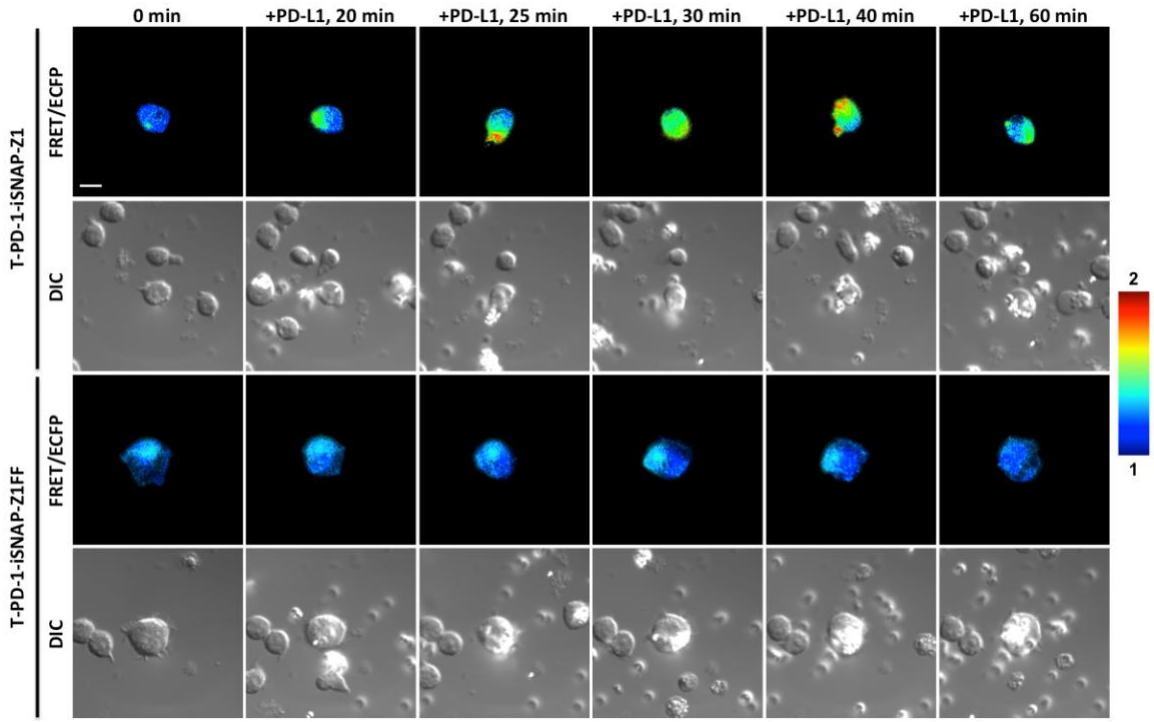

Figure 4.16: Time-lapse imaging in Jurkat cells expressing truncated PD-1 fused iSNAP-ZAP70s in response to particle-bound PD-L1.

Time-lapse FRET imaging in Jurkat cells expressing truncated PD-1 fused iSNAP-ZAP70s (T-PD-1-iSNAP-Z1 or T-PD-1-iSNAP-Z1FF) upon particle-bound PD-L1 stimulation. FRET/ECFP ratio images of Jurkat cells expressing T-PD-1-iSNAP-ZAP70s at the indicated time points are shown in intensity-modulated display mode, and corresponding DIC channel images are shown below FRET/ECFP ratio images. The color scale bar at the right shows the range of FRET/ECFP emission ratio, with cool and warm colors representing low and high ratios, respectively. Scale bars, 5 μm.

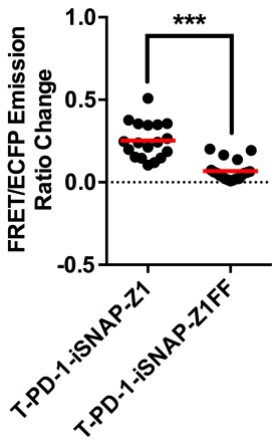

Figure 4.17: The FRET responses of truncated human PD-1 fused iSNAPs for ZAP70 in response to particle-bound PD-L1 in Jurkat cells.

The FRET responses of truncated human PD-1 fused iSNAPs for ZAP70 in Jurkat cells upon particle-bound PD-L1 stimulation. Truncated PD-1 fused iSNAP-ZAP70s include T-PD-1-iSNAP-Z1 and the corresponding negative control T-PD-1-iSNAP-Z1FF. T-PD-1 represents truncated PD-1. n = 18 and 19 Jurkat cells with particle-bound PD-L1 stimulation for T-PD-1-iSNAP-Z1 and T-PD-1-iSNAP-Z1FF, respectively. In scatter plots, the red lines indicate the mean values, the error bars represent the standard error of the mean (S.E.M.) and average data are presented as mean ± S.E.M. *** ($P < 0.001$) is from unpaired two-tailed Mann-Whitney test.

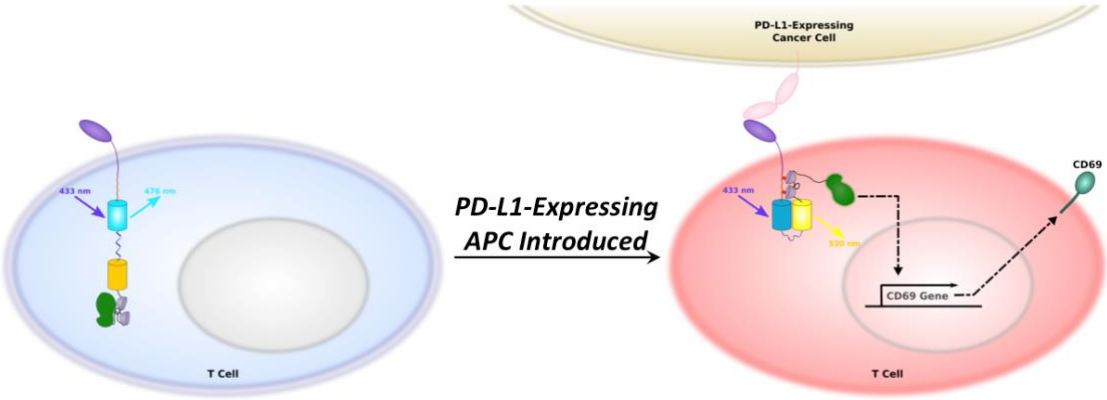

Figure 4.18: Schematic of the activation of T cells expressing PD-1 fused iSNAP-Z1 upon the engagement of PD-L1-expressing cancer cells.

The schematic diagram of the activation of T cells introduced with truncated PD-1 fused iSNAP-Z1 (T-PD-1-iSNAP-Z1) on the membrane of T cells treated co-cultured with PD-L1-expressing cancer cells. Upon PD-1 and PD-L1 ligation, the sensing component of T-PD-1-iSNAP-Z1 gets phosphorylated and subsequently binds to intramolecular tandem SH2 domains. This binding event results in the conformational change and FRET efficiency increase of T-PD-1-iSNAP-Z1, and simultaneously activates T-PD-1-iSNAP-Z1 from the autoinhibition by releasing the activating component. Its active activating component activates downstream T cell activation signaling pathways and leads to the production of very early T cell activation marker CD69 on the cell surface.

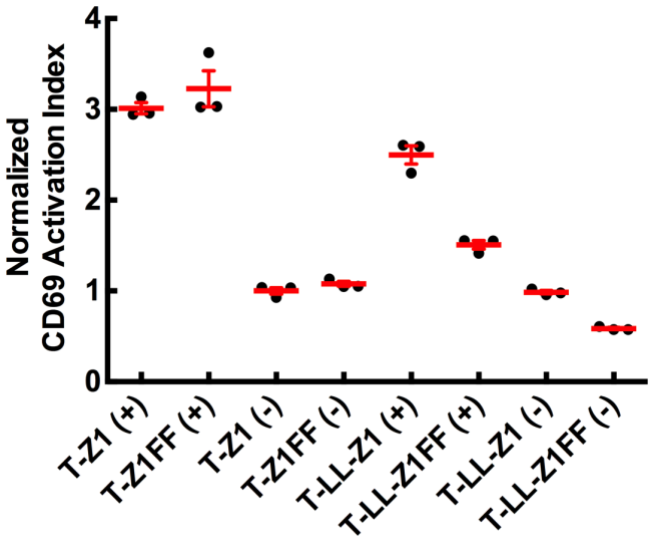

Figure 4.19: CD69 activation in Jurkat cells expressing different truncated human PD-1 fused iSNAP-ZAP70s during co-culture with PD-L1 expressing cancer cells.

The normalized CD69 activation in Jurkat cells expressing truncated human PD-1 fused iSNAPs for ZAP70 in Jurkat cells with or without human interferon gamma-pretreated MDA-MD-231 cell co-culture. Truncated PD-1 fused iSNAP-ZAP70s include T-PD-1-iSNAP-Z1, T-PD-1-LL-iSNAP-Z1 (internal 116 amino acid linker insertion between PD-1 part and sensing component) and the corresponding negative control FF mutants. T-PD-1 represents truncated PD-1. n = 3 Jurkat cells for all eight groups, with (+) representing Jurkat cells with MDA cell co-culture and (-) representing Jurkat cells without MDA cell co-culture. CD69 activation index are normalized against the average value of T-Z1 group without MDA cell co-culture, i.e. T-Z1 (-). In scatter plots, the red lines indicate the mean values, the error bars represent the standard error of the mean (S.E.M.) and average data are presented as mean ± S.E.M.

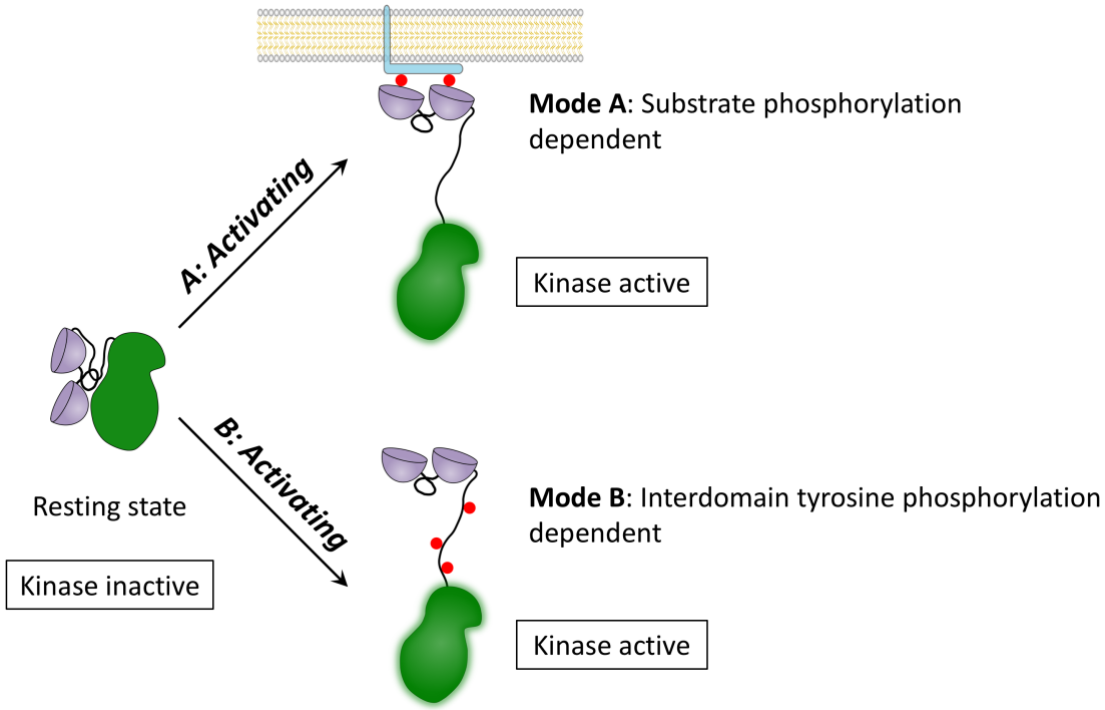

Figure 4.20: Two independent mechanisms of ZAP70 activation.

Schematic diagram of ZAP70 activation mechanisms. ZAP70 is at the resting state due to its autoinihibited conformation determined by the binding of two interdomains to the kinase domain. The dual phosphorylation of the substrate or the phosphorylation of interdomain tyrosine can bind to the tandem ZAP70 SH2 domains and lead to the activation of ZAP70 from its autoinhibition. These two activation mechanisms are independent.

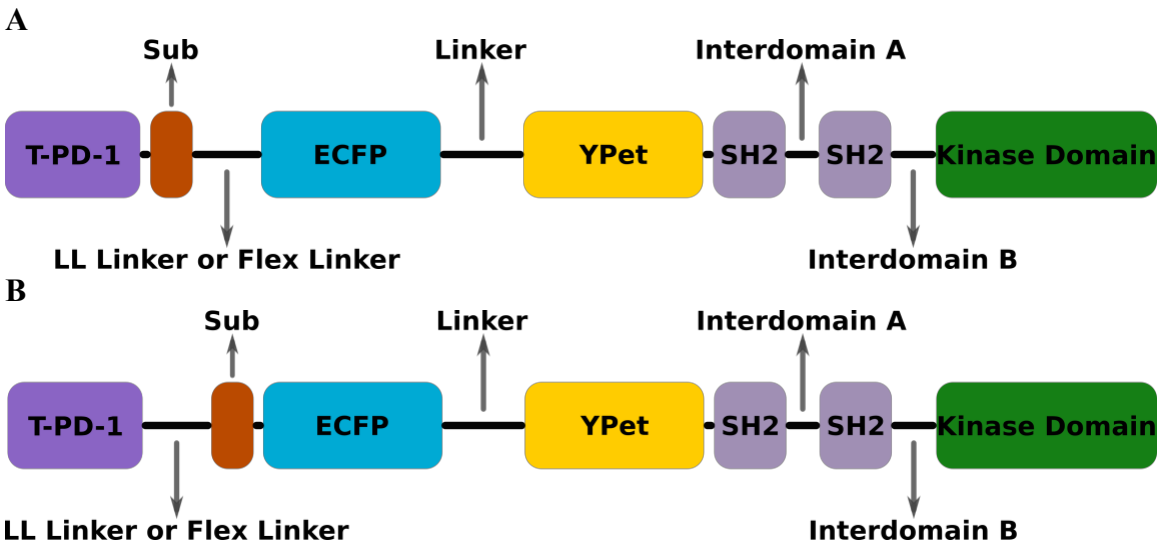

Figure 4.21: The domain organization of truncated human PD-1-fused iSNAPs for ZAP70 with extra internal linkers.

Schematic representation of domain organization and main motifs of truncated human PD-1 fused iSNAP-ZAP70s with extra internal linkers. The general domain organization of truncated human PD-1fused iSNAPs for ZAP70 with internal 116 amino acid long linker (LL) or 17 amino acid flexible linker (Flex linker) inserted between sensing component and FRET pair (**A**) or between PD-1 part and sensing component (**B**). Truncated PD-1 (T-PD-1, 1 to 220 amino acid) is fused at the N-terminal of iSNAPs, and a substrate domain as sensing component shown in brown. A FRET pair (ECFP in cyan and YPet in yellow) flanking a flexible linker is linked to the C-terminal part, which is divided into five domains, a N-terminal SH2 domain (purple), an interdomain A, a C-terminal SH2 domain (purple), an interdomain B and a kinase domain (green) as activating component.

Table 4.1: The substrate sequences of different iSNAPs for ZAP70 and SYK.

The substrate sequences used in different iSNAPs for ZAP70 and SYK are listed with tyrosine and phenylalanine residues bolded. Three CD3 chain substrates are selected for iSNAP-ZAP70s, including iSNAP-Z1, iSNAP-Z2 and iSNAP-Z3, and one CD3 chain substrate is selected for iSNAP-SYK, i.e. iSNAP-S1. All FF mutants are negative mutants of corresponding iSNAPs, including iSNAP-Z1FF, iSNAP-Z2FF, iSNAP-Z3FF and iSNAP-S1FF.

Construct Name	Description
iSNAP-Z1	Substrate 1 of TCR/CD3 complex
iSNAP-Z1FF	Negative mutant of Z1
iSNAP-Z2	Substrate 2 of TCR/CD3 complex
iSNAP-Z2FF	Negative mutant of Z2
iSNAP-Z3	Substrate 3 of TCR/CD3 complex
iSNAP-Z3FF	Negative mutant of Z3
iSNAP-S1	Substrate 4 of TCR/CD3 complex
iSNAP-S1FF	Negative mutant of S1

Table 4.2: The kinase activity assay results of iSNAP-ZAP70s.

Kinase activity measurements of purified iSNAP-Z1 or iSNAP-Z1FF with or without active Lck kinase treatment for 1 hour are listed. Two individual measurements of luminescence intensity in arbitrary unit (a.u.) are averaged and normalized against the mean luminescence internsity of the group iSNAP-Z1FF without Lck kinase treatment.

Group	Luminescence Intensity (a.u.)	Normalized Average Luminescence Intensity (a.u.)
iSNAP-Z1 w/ Lck Kinase	259158	5.92
	258336	
iSNAP-Z1 w/o Lck Kinase	136606	3.09
	133016	
iSNAP-Z1FF w/ Lck Kinase	145726	3.29
	142085	
iSNAP-Z1FF w/o Lck Kinase	42973	1
	44422	

Table 4.3: The descriptions of different human PD-1 fused iSNAPs for ZAP70 and SYK.

The different human PD-1 fused iSNAPs for ZAP70 and SYK are listed. One optimal CD3 chain substrate is selected for full-length PD-1 (FL-PD-1) and truncated PD-1 (T-PD-1) fused iSNAP-ZAP70s, i.e. FL-PD-1-iSNAP-Z1 and T-PD-1-iSNAP-Z1, and one CD3 chain substrate is selected for truncated PD-1 fused iSNAP-SYK, i.e. T-PD-1-iSNAP-S1. All FF mutants are negative mutants of corresponding PD-1 fused iSNAPs, including iSNAP-Z1FF and iSNAP-S1FF.

Construct Name	Substrate Motif	Description of Human PD-1 Part
FL-PD-1-iSNAP-Z1	Substrate 1 of TCR/CD3 complex	Full-length human PD-1
FL-PD-1-iSNAP-Z1FF	Negative mutant of Z1	
T-PD-1-iSNAP-Z1	Substrate 1 of TCR/CD3 complex	Truncated human PD-1
T-PD-1-iSNAP-Z1FF	Negative mutant of Z1	
T-PD-1-iSNAP-S1	Substrate 4 of TCR/CD3 complex	
T-PD-1-iSNAP-S1FF	Negative mutant of S1	

Chapter 5: Summary and Future Directions

Recent advances in molecular engineering and imaging allow us to visualize and quantify a wide variety of molecular signals in single live cells with high-spatiotemporal resolutions using genetically encoded FRET-based biosensors. With highly sensitive biosensors, essentially every subtle signal in different subcellular locations can possibly become observable and the spatiotemporal dynamics of various signaling transductions can be studied, which should advance our understanding on the molecular mechanisms underlying different biological processes, especially cell functions and behaviors.

However, labor-intensive and trial-and-error approaches based on rational assumptions with low efficiency and low effectiveness limit the development of sensitive biosensors. As described in chapter 2, a systematic high-throughput platform based on yeast surface display and directed evolution was developed to identify interaction pairs with better binding affinity. Based on this high-throughput platform, I successfully engineered a highly sensitive FRET biosensor for Src kinase, called SCAGE, and after thorough characterization the newly developed SCAGE biosensor showed more than 40-fold improvement in sensitivities. These results suggest that in principle this high-throughput screening approach can potentially be extended to engineer any sensitive post-translational modification FRET biosensor. On the other hand, a limitation of the approach is that the yeast, a lower eukaryotic organism, exhibits different codon usage and gives different post-translational modification functions as comparing to mammalian cells, which may somewhat influence the biosensor performances, and hence the outcomes from this high-throughput screening approach may not directly result in

optimal responses of biosensors in mammalian cells. Thus, in the future library approach based on higher organism such as mammalian cells is desirable. Furthermore, the biosensor characterization in mammalian cells revealed very distinct dynamics and responses of the SCAGE biosensor under different cellular contexts, suggesting highly sensitive biosensor may be applied to reveal the dynamic differences between different signaling transductions and shed new lights on the molecular mechanisms underlying the distinct regulations.

Moreover, in order to understand intercellular signaling transmission in dynamics, in chapter 3 I integrated FRET microscopy with a unique micro-manipulation photonic system with a high precision, and demonstrated the use for revealing how cells react biochemically to photonic-driven physical perturbations from neighboring cells using the SCAGE biosensor. I also found that the observed rapid Src signaling activation is dependent on passive cytoskeletal structure but not active actomyosin contractility. Therefore, the combination of the two photonic approaches, robotic laser micro-scissors and FRET microscopy, establishes a generally applicable and unique approach to precisely trigger local physical perturbations, and to monitor the spatiotemporal dynamics and transmission of consequent signaling events at the single and multi-cell levels. This novel approach will largely complement the conventional biochemical and imaging methods and shed new light on elucidating cellular crosstalk and integration of physical and biochemical signals.

Beyond detecting molecular signaling events, in chapter 4 I further applied synthetic biology principles to rationally engineer biomolecular machineries, called iSNAPs, which are capable of simultaneously monitoring and manipulating molecular

activities so as to reprogram cell behaviors. Specifically, I applied iSNAPs into T cells and demonstrated how to engineer T cells to overcome immune exhaustion via rewiring the co-inhibitory signaling with the activation signaling by the synthetic molecular machineries.

In summary, by developing and integrating synthetic biology approaches and photonics technologies, the researches in this thesis provide a versatile toolkit, which allows people to not only detect specific biological signaling events via genetically encoded FRET-based biosensors, but also to manipulate various cell signals and behaviors via synthetic molecular machineries. Together, these innovative tools should advance our understanding of complex biological systems and may provide next generation precise therapeutic tools for cancer treatment.

References

1. Andrianantoandro, E.; Basu, S.; Karig, D. K.; Weiss, R., Synthetic biology: new engineering rules for an emerging discipline. *Mol Syst Biol* **2006,** *2*, 2006 0028.

2. Bromley, E. H.; Channon, K.; Moutevelis, E.; Woolfson, D. N., Peptide and protein building blocks for synthetic biology: from programming biomolecules to self-organized biomolecular systems. *ACS Chem Biol* **2008,** *3* (1), 38-50.

3. Schmidt-Dannert, C., Directed evolution of single proteins, metabolic pathways, and viruses. *Biochemistry* **2001,** *40* (44), 13125-36.

4. Lane, M. D.; Seelig, B., Advances in the directed evolution of proteins. *Curr Opin Chem Biol* **2014,** *22*, 129-36.

5. Georgiou, G.; Stathopoulos, C.; Daugherty, P. S.; Nayak, A. R.; Iverson, B. L.; Curtiss, R., 3rd, Display of heterologous proteins on the surface of microorganisms: from the screening of combinatorial libraries to live recombinant vaccines. *Nature biotechnology* **1997,** *15* (1), 29-34.

6. Tsien, R. Y., The green fluorescent protein. *Annu Rev Biochem* **1998,** *67*, 509-44.

7. Shaner, N. C.; Steinbach, P. A.; Tsien, R. Y., A guide to choosing fluorescent proteins. *Nature Methods* **2005,** *2* (12), 905-909.

8. Shaner, N. C.; Patterson, G. H.; Davidson, M. W., Advances in fluorescent protein technology. *Journal of cell science* **2007,** *120* (24), 4247-4260.

9. Periasamy, A.; Day, R., *Molecular imaging: FRET microscopy and spectroscopy*. Elsevier: 2011.

10. Piston, D. W.; Kremers, G. J., Fluorescent protein FRET: the good, the bad and the ugly. *Trends Biochem Sci* **2007,** *32* (9), 407-14.

11. Wang, Y.; Shyy, J. Y.; Chien, S., Fluorescence proteins, live-cell imaging, and mechanobiology: seeing is believing. *Annu Rev Biomed Eng* **2008,** *10*, 1-38.

12. Frommer, W. B.; Davidson, M. W.; Campbell, R. E., Genetically encoded biosensors based on engineered fluorescent proteins. *Chemical Society Reviews* **2009,** *38* (10), 2833-2841.

13. Berns, M. W.; Edwards, J.; Strahs, K.; Girton, J.; McNeill, P.; Rattner, J.; Kitzes, M.; Hammer-Wilson, M.; Liaw, L.; Siemens, A., Laser microsurgery in cell and developmental biology. *Science* **1981,** *213* (4507), 505-513.

14. Botvinick, E. L.; Berns, M. W., Internet-based robotic laser scissors and tweezers microscopy. *Microsc Res Tech* **2005,** *68* (2), 65-74.

15. Berns, M. W., A history of laser scissors (microbeams). *Methods in cell biology* **2007,** *82*, 1-58.

16. Shen, N.; Datta, D.; Schaffer, C. B.; LeDuc, P.; Ingber, D. E.; Mazur, E., Ablation of cytoskeletal filaments and mitochondria in live cells using a femtosecond laser nanoscissor. *Mech. Chem. Biosyst* **2005,** *2* (1), 17-25.

17. Kumar, S.; Maxwell, I. Z.; Heisterkamp, A.; Polte, T. R.; Lele, T. P.; Salanga, M.; Mazur, E.; Ingber, D. E., Viscoelastic retraction of single living stress fibers and its impact on cell shape, cytoskeletal organization, and extracellular matrix mechanics. *Biophysical journal* **2006,** *90* (10), 3762-3773.

18. Wakida, N. M.; Lee, C. S.; Botvinick, E. T.; Shi, L. Z.; Dvornikov, A.; Berns, M. W., Laser nanosurgery of single microtubules reveals location-dependent depolymerization rates. *J Biomed Opt* **2007,** *12* (2), 024022.

19. Tanner, K.; Boudreau, A.; Bissell, M. J.; Kumar, S., Dissecting regional variations in stress fiber mechanics in living cells with laser nanosurgery. *Biophysical journal* **2010,** *99* (9), 2775-83.

20. Gumbiner, B. M., Regulation of cadherin-mediated adhesion in morphogenesis. *Nat Rev Mol Cell Biol* **2005,** *6* (8), 622-34.

21. Juliano, R. L., Signal transduction by cell adhesion receptors and the cytoskeleton: functions of integrins, cadherins, selectins, and immunoglobulin-superfamily members. *Annu Rev Pharmacol Toxicol* **2002,** *42*, 283-323.

22. Lecuit, T.; Lenne, P. F.; Munro, E., Force Generation, Transmission, and Integration during Cell and Tissue Morphogenesis. *Annu Rev Cell Dev Bi* **2011,** *27*, 157-184.

23. Na, S.; Collin, O.; Chowdhury, F.; Tay, B.; Ouyang, M.; Wang, Y.; Wang, N., Rapid signal transduction in living cells is a unique feature of mechanotransduction. *Proceedings of the National Academy of Sciences of the United States of America* **2008,** *105* (18), 6626-31.

24. Wang, Y.; Botvinick, E. L.; Zhao, Y.; Berns, M. W.; Usami, S.; Tsien, R. Y.; Chien, S., Visualizing the mechanical activation of Src. *Nature* **2005,** *434* (7036), 1040-5.

25. Felsenfeld, D. P.; Schwartzberg, P. L.; Venegas, A.; Tse, R.; Sheetz, M. P., Selective regulation of integrin--cytoskeleton interactions by the tyrosine kinase Src. *Nat Cell Biol* **1999,** *1* (4), 200-6.

26. DuFort, C. C.; Paszek, M. J.; Weaver, V. M., Balancing forces: architectural control of mechanotransduction. *Nat Rev Mol Cell Biol* **2011,** *12* (5), 308-19.

27. Guilluy, C.; Osborne, L. D.; Van Landeghem, L.; Sharek, L.; Superfine, R.; Garcia-Mata, R.; Burridge, K., Isolated nuclei adapt to force and reveal a mechanotransduction pathway in the nucleus. *Nat Cell Biol* **2014,** *16* (4), 376-81.

28. Fedorchak, G. R.; Kaminski, A.; Lammerding, J., Cellular mechanosensing: getting to the nucleus of it all. *Prog Biophys Mol Biol* **2014,** *115* (2-3), 76-92.

29. van Roy, F.; Berx, G., The cell-cell adhesion molecule E-cadherin. *Cell Mol Life Sci* **2008,** *65* (23), 3756-88.

30. Owens, D. W.; McLean, G. W.; Wyke, A. W.; Paraskeva, C.; Parkinson, E. K.; Frame, M. C.; Brunton, V. G., The catalytic activity of the Src family kinases is required to disrupt cadherin-dependent cell–cell contacts. *Molecular biology of the cell* **2000,** *11* (1), 51-64.

31. McLachlan, R. W.; Kraemer, A.; Helwani, F. M.; Kovacs, E. M., E-cadherin adhesion activates c-Src signaling at cell–cell contacts. *Molecular biology of the cell* **2007,** *18* (8), 3214-3223.

32. Ren, G.; Helwani, F. M.; Verma, S.; McLachlan, R. W.; Weed, S. A.; Yap, A. S., Cortactin is a functional target of E-cadherin-activated Src family kinases in MCF7 epithelial monolayers. *The Journal of biological chemistry* **2009,** *284* (28), 18913-22.

33. Gomez, G. A.; McLachlan, R. W.; Wu, S. K.; Caldwell, B. J.; Moussa, E.; Verma, S.; Bastiani, M.; Priya, R.; Parton, R. G.; Gaus, K.; Sap, J.; Yap, A. S., An RPTPalpha/Src family kinase/Rap1 signaling module recruits myosin IIB to support contractile tension at apical E-cadherin junctions. *Molecular biology of the cell* **2015,** *26* (7), 1249-62.

34. Swann, J. B.; Smyth, M. J., Immune surveillance of tumors. *J Clin Invest* **2007,** *117* (5), 1137-46.

35. Pardoll, D. M., The blockade of immune checkpoints in cancer immunotherapy. *Nature Reviews Cancer* **2012,** *12* (4), 252-264.

36. Bonilla, F. A.; Oettgen, H. C., Adaptive immunity. *J Allergy Clin Immun* **2010,** *125* (2), S33-S40.

37. Rabb, H., The T cell as a bridge between innate and adaptive immune systems: Implications for the kidney. *Kidney Int* **2002,** *61* (6), 1935-1946.

38. Vesely, M. D.; Kershaw, M. H.; Schreiber, R. D.; Smyth, M. J., Natural innate and adaptive immunity to cancer. *Annu Rev Immunol* **2011,** *29*, 235-71.

39. Gajewski, T. F.; Schreiber, H.; Fu, Y. X., Innate and adaptive immune cells in the tumor microenvironment. *Nat Immunol* **2013,** *14* (10), 1014-22.

40. Malissen, B.; Gregoire, C.; Malissen, M.; Roncagalli, R., Integrative biology of T cell activation. *Nat Immunol* **2014,** *15* (9), 790-7.

41. Smith-Garvin, J. E.; Koretzky, G. A.; Jordan, M. S., T cell activation. *Annu Rev Immunol* **2009,** *27*, 591-619.

42. Scandiuzzi, L.; Ghosh, K.; Zang, X., T cell costimulation and coinhibition: genetics and disease. *Discov Med* **2011,** *12* (63), 119-28.

43. Couzin-Frankel, J., Cancer Immunotherapy. *Science* **2013,** *342* (6165), 1432-1433.

44. Sadelain, M.; Brentjens, R.; Riviere, I., The Basic Principles of Chimeric Antigen Receptor Design. *Cancer Discovery* **2013,** *3* (4), 388-398.

45. John, L. B.; Kershaw, M. H.; Darcy, P. K., Blockade of PD-1 immunosuppression boosts CAR T-cell therapy. *Oncoimmunology* **2013,** *2* (10).

46. Kiyokawa, E.; Hara, S.; Nakamura, T.; Matsuda, M., Fluorescence (Forster) resonance energy transfer imaging of oncogene activity in living cells. *Cancer Sci* **2006,** *97* (1), 8-15.

47. Arnold, F. H.; Moore, J. C., Optimizing industrial enzymes by directed evolution. *Adv Biochem Eng Biotechnol* **1997,** *58*, 1-14.

48. Daugherty, P. S., Protein engineering with bacterial display. *Curr Opin Struct Biol* **2007,** *17* (4), 474-80.

49. Gai, S. A.; Wittrup, K. D., Yeast surface display for protein engineering and characterization. *Curr Opin Struct Biol* **2007,** *17* (4), 467-73.

50. Samuelson, P.; Gunneriusson, E.; Nygren, P. A.; Stahl, S., Display of proteins on bacteria. *J Biotechnol* **2002,** *96* (2), 129-54.

51. Richman, S. A.; Kranz, D. M., Display, engineering, and applications of antigen-specific T cell receptors. *Biomol Eng* **2007,** *24* (4), 361-73.

52. Arnold, F. H.; Georgiou, G., Directed evolution library creation. *Methods in molecular biology* **2003,** *231*.

53. Ting, A. Y.; Kain, K. H.; Klemke, R. L.; Tsien, R. Y., Genetically encoded fluorescent reporters of protein tyrosine kinase activities in living cells. *Proceedings of the National Academy of Sciences of the United States of America* **2001,** *98* (26), 15003-8.

54. Miyawaki, A.; Llopis, J.; Heim, R.; McCaffery, J. M.; Adams, J. A.; Ikura, M.; Tsien, R. Y., Fluorescent indicators for Ca2+ based on green fluorescent proteins and calmodulin. *Nature* **1997,** *388* (6645), 882-7.

55. Niwa, H.; Yamamura, K.; Miyazaki, J., Efficient selection for high-expression transfectants with a novel eukaryotic vector. *Gene* **1991,** *108* (2), 193-9.

56. Komatsu, N.; Aoki, K.; Yamada, M.; Yukinaga, H.; Fujita, Y.; Kamioka, Y.; Matsuda, M., Development of an optimized backbone of FRET biosensors for kinases and GTPases. *Molecular biology of the cell* **2011,** *22* (23), 4647-56.

57. Jalali, S.; Li, Y. S.; Sotoudeh, M.; Yuan, S.; Li, S.; Chien, S.; Shyy, J. Y., Shear stress activates p60src-Ras-MAPK signaling pathways in vascular endothelial cells. *Arteriosclerosis, thrombosis, and vascular biology* **1998,** *18* (2), 227-34.

58. Seong, J.; Lu, S.; Ouyang, M.; Huang, H.; Zhang, J.; Frame, M. C.; Wang, Y., Visualization of Src activity at different compartments of the plasma membrane by FRET imaging. *Chem Biol* **2009,** *16* (1), 48-57.

59. Kim, T. J.; Sun, J.; Lu, S.; Zhang, J.; Wang, Y., The regulation of beta-adrenergic receptor-mediated PKA activation by substrate stiffness via microtubule dynamics in human MSCs. *Biomaterials* **2014,** *35* (29), 8348-56.

60. Gietz, R. D.; Schiestl, R. H., High-efficiency yeast transformation using the LiAc/SS carrier DNA/PEG method. *Nat Protoc* **2007,** *2* (1), 31-34.

61. Kolega, J., Phototoxicity and photoinactivation of blebbistatin in UV and visible light. *Biochemical and biophysical research communications* **2004,** *320* (3), 1020-1025.

62. Sakamoto, T.; Limouze, J.; Combs, C. A.; Straight, A. F.; Sellers, J. R., Blebbistatin, a myosin II inhibitor, is photoinactivated by blue light. *Biochemistry* **2005,** *44* (2), 584-588.

63. Tsien, R. Y.; Harootunian, A. T., Practical design criteria for a dynamic ratio imaging system. *Cell Calcium* **1990,** *11* (2-3), 93-109.

64. Songyang, Z.; Carraway, K. L., 3rd; Eck, M. J.; Harrison, S. C.; Feldman, R. A.; Mohammadi, M.; Schlessinger, J.; Hubbard, S. R.; Smith, D. P.; Eng, C.; et al., Catalytic specificity of protein-tyrosine kinases is critical for selective signalling. *Nature* **1995,** *373* (6514), 536-9.

65. Songyang, Z.; Shoelson, S. E.; Chaudhuri, M.; Gish, G.; Pawson, T.; Haser, W. G.; King, F.; Roberts, T.; Ratnofsky, S.; Lechleider, R. J.; et al., SH2 domains recognize specific phosphopeptide sequences. *Cell* **1993,** *72* (5), 767-78.

66. Bradshaw, J. M.; Mitaxov, V.; Waksman, G., Investigation of phosphotyrosine recognition by the SH2 domain of the Src kinase. *J Mol Biol* **1999,** *293* (4), 971-85.

67. Ouyang, M.; Sun, J.; Chien, S.; Wang, Y., Determination of hierarchical relationship of Src and Rac at subcellular locations with FRET biosensors. *Proceedings of the National Academy of Sciences of the United States of America* **2008,** *105* (38), 14353-8.

68. Kaneko, T.; Huang, H.; Cao, X.; Li, X.; Li, C.; Voss, C.; Sidhu, S. S.; Li, S. S., Superbinder SH2 domains act as antagonists of cell signaling. *Science signaling* **2012,** *5* (243), ra68.

69. Waksman, G.; Kominos, D.; Robertson, S. C.; Pant, N.; Baltimore, D.; Birge, R. B.; Cowburn, D.; Hanafusa, H.; Mayer, B. J.; Overduin, M.; Resh, M. D.; Rios, C. B.; Silverman, L.; Kuriyan, J., Crystal structure of the phosphotyrosine recognition domain SH2 of v-src complexed with tyrosine-phosphorylated peptides. *Nature* **1992,** *358* (6388), 646-53.

70. Ostman, A.; Bohmer, F. D., Regulation of receptor tyrosine kinase signaling by protein tyrosine phosphatases. *Trends Cell Biol* **2001,** *11* (6), 258-66.

71. Chiarugi, P.; Cirri, P.; Taddei, M. L.; Talini, D.; Doria, L.; Fiaschi, T.; Buricchi, F.; Giannoni, E.; Camici, G.; Raugei, G.; Ramponi, G., New perspectives in PDGF receptor downregulation: the main role of phosphotyrosine phosphatases. *Journal of cell science* **2002,** *115* (Pt 10), 2219-32.

72. Thien, C. B.; Langdon, W. Y., Cbl: many adaptations to regulate protein tyrosine kinases. *Nat Rev Mol Cell Biol* **2001,** *2* (4), 294-307.

73. Goh, L. K.; Sorkin, A., Endocytosis of receptor tyrosine kinases. *Cold Spring Harbor perspectives in biology* **2013,** *5* (5), a017459.

74. Gerhart, J., 1998 Warkany lecture: signaling pathways in development. *Teratology* **1999,** *60* (4), 226-39.

75. Dale, B.; Gualtieri, R.; Talevi, R.; Tosti, E.; Santella, L.; Elder, K., Intercellular communication in the early human embryo. *Mol Reprod Dev* **1991,** *29* (1), 22-8.

76. Van Norman, J. M.; Breakfield, N. W.; Benfey, P. N., Intercellular communication during plant development. *Plant Cell* **2011,** *23* (3), 855-64.

77. Alberts, B.; Johnson, A.; Lewis, J.; Raff, M.; Roberts, K.; Walter, P., General principles of cell communication. **2002**.

78. Takeichi, M., Cadherin Cell-Adhesion Receptors as a Morphogenetic Regulator. *Science* **1991,** *251* (5000), 1451-1455.

79. Leckband, D. E.; le Duc, Q.; Wang, N.; de Rooij, J., Mechanotransduction at cadherin-mediated adhesions. *Current opinion in cell biology* **2011,** *23* (5), 523-530.

80. Schwartz, M. A.; DeSimone, D. W., Cell adhesion receptors in mechanotransduction. *Current opinion in cell biology* **2008,** *20* (5), 551-556.

81. Behrens, J., Cadherins and catenins: role in signal transduction and tumor progression. *Cancer Metastasis Rev* **1999,** *18* (1), 15-30.

82. Hartsock, A.; Nelson, W. J., Adherens and tight junctions: structure, function and connections to the actin cytoskeleton. *Biochim Biophys Acta* **2008,** *1778* (3), 660-9.

83. Jeanes, A.; Gottardi, C. J.; Yap, A. S., Cadherins and cancer: how does cadherin dysfunction promote tumor progression? *Oncogene* **2008,** *27* (55), 6920-6929.

84. Daniel, J. M.; Reynolds, A. B., Tyrosine phosphorylation and cadherin/catenin function. *Bioessays* **1997,** *19* (10), 883-91.

85. Gumbiner, B. M., Regulation of cadherin adhesive activity. *The Journal of cell biology* **2000,** *148* (3), 399-404.

86. Lilien, J.; Balsamo, J., The regulation of cadherin-mediated adhesion by tyrosine phosphorylation/dephosphorylation of beta-catenin. *Curr Opin Cell Biol* **2005,** *17* (5), 459-65.

87. Yeatman, T. J., A renaissance for SRC. *Nature reviews. Cancer* **2004,** *4* (6), 470-80.

88. Tsukita, S.; Oishi, K.; Akiyama, T.; Yamanashi, Y.; Yamamoto, T.; Tsukita, S., Specific Protooncogenic Tyrosine Kinases of Src Family Are Enriched in Cell-to-Cell Adherens Junctions Where the Level of Tyrosine Phosphorylation Is Elevated. *Journal of Cell Biology* **1991,** *113* (4), 867-879.

89. Calautti, E.; Cabodi, S.; Stein, P. L.; Hatzfeld, M.; Kedersha, N.; Dotto, G. P., Tyrosine phosphorylation and src family kinases control keratinocyte cell-cell adhesion. *Journal of Cell Biology* **1998,** *141* (6), 1449-1465.

90. Matsuyoshi, N.; Hamaguchi, M.; Taniguchi, S.; Nagafuchi, A.; Tsukita, S.; Takeichi, M., Cadherin-mediated cell-cell adhesion is perturbed by v-src tyrosine phosphorylation in metastatic fibroblasts. *The Journal of cell biology* **1992,** *118* (3), 703-14.

91. Behrens, J.; Vakaet, L.; Friis, R.; Winterhager, E.; Van Roy, F.; Mareel, M. M.; Birchmeier, W., Loss of epithelial differentiation and gain of invasiveness correlates with tyrosine phosphorylation of the E-cadherin/beta-catenin complex in cells transformed with a temperature-sensitive v-SRC gene. *The Journal of cell biology* **1993,** *120* (3), 757-66.

92. Lu, S.; Kim, T. J.; Chen, C. E.; Ouyang, M.; Seong, J.; Liao, X.; Wang, Y., Computational analysis of the spatiotemporal coordination of polarized PI3K and Rac1 activities in micro-patterned live cells. *PLoS One* **2011,** *6* (6), e21293.

93. Lu, S. Y.; Seong, J.; Wang, Y.; Chang, S. C.; Eichorst, J. P.; Ouyang, M. X.; Li, J. Y. S.; Chien, S.; Wang, Y. X., Decipher the dynamic coordination between enzymatic activity and structural modulation at focal adhesions in living cells. *Sci Rep-Uk* **2014,** *4*.

94. Riedl, J.; Crevenna, A. H.; Kessenbrock, K.; Yu, J. H.; Neukirchen, D.; Bista, M.; Bradke, F.; Jenne, D.; Holak, T. A.; Werb, Z.; Sixt, M.; Wedlich-Soldner, R., Lifeact: a versatile marker to visualize F-actin. *Nat Methods* **2008,** *5* (7), 605-7.

95. Ratheesh, A.; Yap, A. S., A bigger picture: classical cadherins and the dynamic actin cytoskeleton. *Nature reviews Molecular cell biology* **2012,** *13* (10), 673-679.

96. Allemani, C.; Weir, H. K.; Carreira, H.; Harewood, R.; Spika, D.; Wang, X. S.; Bannon, F.; Ahn, J. V.; Johnson, C. J.; Bonaventure, A.; Marcos-Gragera, R.; Stiller, C.; Azevedo e Silva, G.; Chen, W. Q.; Ogunbiyi, O. J.; Rachet, B.; Soeberg, M. J.; You, H.; Matsuda, T.; Bielska-Lasota, M.; Storm, H.; Tucker, T. C.; Coleman, M. P.; Group, C. W., Global surveillance of cancer survival 1995-2009: analysis of individual data for 25,676,887 patients from 279 population-based registries in 67 countries (CONCORD-2). *Lancet* **2015,** *385* (9972), 977-1010.

97. American Cancer Society: Cancer Facts & Figures 2017. Atlanta, GA: American Cancer Society. **2017**.

98. Siegel, R. L.; Miller, K. D.; Jemal, A., Cancer statistics, 2016. *CA Cancer J Clin* **2016,** *66* (1), 7-30.

99. Fidler, I. J., The pathogenesis of cancer metastasis: the 'seed and soil' hypothesis revisited. *Nature reviews. Cancer* **2003,** *3* (6), 453-8.

100. Gupta, G. P.; Massague, J., Cancer metastasis: building a framework. *Cell* **2006,** *127* (4), 679-95.

101. Samelson, L. E., Signal transduction mediated by the T cell antigen receptor: the role of adapter proteins. *Annu Rev Immunol* **2002,** *20*, 371-94.

102. Cantrell, D. A., T-cell antigen receptor signal transduction. *Immunology* **2002,** *105* (4), 369-74.

103. Brownlie, R. J.; Zamoyska, R., T cell receptor signalling networks: branched, diversified and bounded. *Nat Rev Immunol* **2013,** *13* (4), 257-69.

104. Sharpe, A. H.; Freeman, G. J., The B7-CD28 superfamily. *Nat Rev Immunol* **2002,** *2* (2), 116-26.

105. Chen, L.; Flies, D. B., Molecular mechanisms of T cell co-stimulation and co-inhibition. *Nat Rev Immunol* **2013,** *13* (4), 227-42.

106. Choudhuri, K.; van der Merwe, P. A. In *Molecular mechanisms involved in T cell receptor triggering*, Seminars in immunology, Elsevier: 2007; pp 255-261.

107. Varma, R., TCR triggering by the pMHC complex: valency, affinity, and dynamics. *Science signaling* **2008,** *1* (19), pe21.

108. Davis, S. J.; van der Merwe, P. A., The kinetic-segregation model: TCR triggering and beyond. *Nat Immunol* **2006,** *7* (8), 803-9.

109. Artyomov, M. N.; Lis, M.; Devadas, S.; Davis, M. M.; Chakraborty, A. K., CD4 and CD8 binding to MHC molecules primarily acts to enhance Lck delivery. *Proceedings of the National Academy of Sciences of the United States of America* **2010,** *107* (39), 16916-21.

110. Chakraborty, A. K.; Weiss, A., Insights into the initiation of TCR signaling. *Nature Immunology* **2014,** *15* (9), 798-807.

111. Palacios, E. H.; Weiss, A., Function of the Src-family kinases, Lck and Fyn, in T-cell development and activation. *Oncogene* **2004,** *23* (48), 7990-8000.

112. Wang, H.; Kadlecek, T. A.; Au-Yeung, B. B.; Goodfellow, H. E.; Hsu, L. Y.; Freedman, T. S.; Weiss, A., ZAP-70: an essential kinase in T-cell signaling. *Cold Spring Harbor perspectives in biology* **2010,** *2* (5), a002279.

113. Klammt, C.; Novotna, L.; Li, D. T.; Wolf, M.; Blount, A.; Zhang, K.; Fitchett, J. R.; Lillemeier, B. F., T cell receptor dwell times control the kinase activity of Zap70. *Nat Immunol* **2015,** *16* (9), 961-9.

114. Katz, Z. B.; Novotna, L.; Blount, A.; Lillemeier, B. F., A cycle of Zap70 kinase activation and release from the TCR amplifies and disperses antigenic stimuli. *Nat Immunol* **2017,** *18* (1), 86-95.

115. Mocsai, A.; Ruland, J.; Tybulewicz, V. L., The SYK tyrosine kinase: a crucial player in diverse biological functions. *Nat Rev Immunol* **2010,** *10* (6), 387-402.

116. Warrington, R.; Watson, W.; Kim, H. L.; Antonetti, F. R., An introduction to immunology and immunopathology. *Allergy Asthma Clin Immunol* **2011,** *7 Suppl 1*, S1.

117. Walunas, T. L.; Lenschow, D. J.; Bakker, C. Y.; Linsley, P. S.; Freeman, G. J.; Green, J. M.; Thompson, C. B.; Bluestone, J. A., Ctla-4 Can Function as a Negative Regulator of T-Cell Activation. *Immunity* **1994,** *1* (5), 405-413.

118. Krummel, M. F.; Allison, J. P., Cd28 and Ctla-4 Have Opposing Effects on the Response of T-Cells to Stimulation. *Journal of Experimental Medicine* **1995,** *182* (2), 459-465.

119. Thompson, C. B.; Allison, J. P., The emerging role of CTLA-4 as an immune attenuator. *Immunity* **1997,** *7* (4), 445-450.

120. McCoy, K. D.; Le Gros, G., The role of CTLA-4 in the regulation of T cell immune responses. *Immunol Cell Biol* **1999,** *77* (1), 1-10.

121. Chambers, C. A.; Kuhns, M. S.; Egen, J. G.; Allison, J. P., CTLA-4-mediated inhibition in regulation of T cell responses: Mechanisms and manipulation in tumor immunotherapy. *Annual Review of Immunology* **2001,** *19*, 565-594.

122. Egen, J. G.; Kuhns, M. S.; Allison, J. P., CTLA-4: new insights into its biological function and use in tumor immunotherapy. *Nature Immunology* **2002,** *3* (7), 611-618.

123. Buchbinder, E. I.; Desai, A., CTLA-4 and PD-1 Pathways Similarities, Differences, and Implications of Their Inhibition. *Am J Clin Oncol-Canc* **2016,** *39* (1), 98-106.

124. Fife, B. T.; Bluestone, J. A., Control of peripheral T-cell tolerance and autoimmunity via the CTLA-4 and PD-1 pathways. *Immunological Reviews* **2008,** *224*, 166-182.

125. Riley, J. L.; June, C. H., The CD28 family: a T-cell rheostat for therapeutic control of T-cell activation. *Blood* **2005,** *105* (1), 13-21.

126. Chinai, J. M.; Janakiram, M.; Chen, F. X.; Chen, W. T.; Kaplan, M.; Zang, X. X., New immunotherapies targeting the PD-1 pathway. *Trends in Pharmacological Sciences* **2015,** *36* (9), 587-595.

127. Rudd, C. E.; Taylor, A.; Schneider, H., CD28 and CTLA-4 coreceptor expression and signal transduction. *Immunol Rev* **2009,** *229* (1), 12-26.

128. Li, Y.; Li, F.; Jiang, F.; Lv, X.; Zhang, R.; Lu, A.; Zhang, G., A Mini-Review for Cancer Immunotherapy: Molecular Understanding of PD-1/PD-L1 Pathway & Translational Blockade of Immune Checkpoints. *Int J Mol Sci* **2016,** *17* (7).

129. Mahoney, K. M.; Freeman, G. J.; McDermott, D. F., The Next Immune-Checkpoint Inhibitors: PD-1/PD-L1 Blockade in Melanoma. *Clin Ther* **2015,** *37* (4), 764-782.

130. Dong, H. D.; Zhu, G. F.; Tamada, K.; Chen, L. P., B7-H1, a third member of the B7 family, co-stimulates T-cell proliferation and interleukin-10 secretion. *Nature Medicine* **1999,** *5* (12), 1365-1369.

131. Freeman, G. J.; Long, A. J.; Iwai, Y.; Latchman, Y.; Bourque, K.; Brown, J. A.; Boussiotis, V. A.; Dorfman, D. M.; Chernova, T.; Nishimura, H.; Fitz, L.; Malenkovich, N.; Okazaki, T.; Byrne, M.; Horton, H.; Fouser, L.; Carter, L.; Sharpe, A. H.; Carreno, B.; Collins, M.; Wood, C. R.; Honjo, T., Engagement of the PD-1 immunoinhibitory receptor by a novel B7-family member leads to negative regulation of lymphocyte activation. *Blood* **2000,** *96* (11), 810a-811a.

132. Latchman, Y.; Wood, C.; Chemova, T.; Iwai, Y.; Malenkovich, N.; Long, A.; Bourque, K.; Boussiotis, V.; Nishimura, H.; Honjo, T.; Sharpe, A.; Freeman, G., PD-L2, a novel B7 homologue, is a second ligand for PD-1 and inhibits T cell activation. *Faseb Journal* **2001,** *15* (4), A345-A345.

133. Mueller, D. L., Mechanisms maintaining peripheral tolerance. *Nat Immunol* **2010,** *11* (1), 21-7.

134. Xing, Y.; Hogquist, K. A., T-cell tolerance: central and peripheral. *Cold Spring Harbor perspectives in biology* **2012,** *4* (6).

135. Waterhouse, P.; Penninger, J. M.; Timms, E.; Wakeham, A.; Shahinian, A.; Lee, K. P.; Thompson, C. B.; Griesser, H.; Mak, T. W., Lymphoproliferative Disorders with Early Lethality in Mice Deficient in Ctla-4. *Science* **1995,** *270* (5238), 985-988.

136. Tivol, E. A.; Borriello, F.; Schweitzer, A. N.; Lynch, W. P.; Bluestone, J. A.; Sharpe, A. H., Loss of Ctla-4 Leads to Massive Lymphoproliferation and Fatal Multiorgan Tissue Destruction, Revealing a Critical Negative Regulatory Role of Ctla-4. *Immunity* **1995,** *3* (5), 541-547.

137. Keir, M. E.; Butte, M. J.; Freeman, G. J.; Sharpel, A. H., PD-1 and its ligands in tolerance and immunity. *Annual Review of Immunology* **2008,** *26*, 677-704.

138. Francisco, L. M.; Sage, P. T.; Sharpe, A. H., The PD-1 pathway in tolerance and autoimmunity. *Immunological Reviews* **2010,** *236*, 219-242.

139. Gianchecchi, E.; Delfino, D. V.; Fierabracci, A., Recent insights into the role of the PD-1/PD-L1 pathway in immunological tolerance and autoimmunity. *Autoimmun Rev* **2013,** *12* (11), 1091-1100.

140. Nishimura, H.; Nose, M.; Hiai, H.; Minato, N.; Honjo, T., Development of lupus-like autoimmune diseases by disruption of the PD-1 gene encoding an ITIM motif-carrying immunoreceptor. *Immunity* **1999,** *11* (2), 141-51.

141. Nishimura, H.; Okazaki, T.; Tanaka, Y.; Nakatani, K.; Hara, M.; Matsumori, A.; Sasayama, S.; Mizoguchi, A.; Hiai, H.; Minato, N.; Honjo, T., Autoimmune dilated cardiomyopathy in PD-1 receptor-deficient mice. *Science* **2001,** *291* (5502), 319-22.

142. Ansari, M. J. I.; Salama, A. D.; Chitnis, T.; Smith, R. N.; Yagita, H.; Akiba, H.; Yamazaki, T.; Azuma, M.; Iwai, H.; Khoury, S. J.; Auchincloss, H.; Sayegh, M. H., The programmed death-1 (PD-1) pathway regulates autoimmune diabetes in nonobese diabetic (NOD) mice. *Journal of Experimental Medicine* **2003,** *198* (1), 63-69.

143. Wang, J.; Yoshida, T.; Nakaki, F.; Hiai, H.; Okazaki, T.; Honjo, T., Establishment of NOD-Pdcd1(-/-) mice as an efficient animal model of type I diabetes. *Proceedings of the National Academy of Sciences of the United States of America* **2005,** *102* (33), 11823-11828.

144. Fife, B. T.; Guleria, I.; Bupp, M.; Tang, Q.; Eagar, T.; Bour-Jordan, H.; Yagita, H.; Azuma, M.; Sayegh, M. H.; Bluestone, J., The programmed death-1 (pd-1) pathway regulates peripheral T cell tolerance during autoimmune diabetes in nonobese diabetic (NOD) mice. *Clinical Immunology* **2007,** *123*, S27-S27.

145. Baecher-Allan, C.; Brown, J. A.; Freeman, G. J.; Hafler, D. A., CD4+CD25(high) regulatory cells in human peripheral blood. *Journal of Immunology* **2001,** *167* (3), 1245-1253.

146. Sandner, S. E.; Clarkson, M. R.; Salama, A. D.; Sanchez-Fueyo, A.; Domenig, C.; Habicht, A.; Najafian, N.; Yagita, H.; Azuma, M.; Turka, L. A.; Sayegh, M. H., Role of the programmed death-1 pathway in regulation of alloimmune responses in vivo. *Journal of Immunology* **2005,** *174* (6), 3408-3415.

147. Patel, S. P.; Kurzrock, R., PD-L1 Expression as a Predictive Biomarker in Cancer Immunotherapy. *Molecular cancer therapeutics* **2015,** *14* (4), 847-856.

148. Baskar, R.; Lee, K. A.; Yeo, R.; Yeoh, K. W., Cancer and Radiation Therapy: Current Advances and Future Directions. *Int J Med Sci* **2012,** *9* (3), 193-199.

149. Chabner, B. A.; Roberts, T. G., Timeline - Chemotherapy and the war on cancer. *Nature Reviews Cancer* **2005,** *5* (1), 65-72.

150. Steinman, R. M.; Mellman, I., Immunotherapy: Bewitched, bothered, and bewildered no more. *Science* **2004,** *305* (5681), 197-200.

151. Lim, W. A.; June, C. H., The Principles of Engineering Immune Cells to Treat Cancer. *Cell* **2017,** *168* (4), 724-740.

152. Couzin-Frankel, J., Breakthrough of the year 2013. Cancer immunotherapy. *Science* **2013,** *342* (6165), 1432-3.

153. Fesnak, A. D.; June, C. H.; Levine, B. L., Engineered T cells: the promise and challenges of cancer immunotherapy. *Nature Reviews Cancer* **2016,** *16* (9), 566-581.

154. Pardoll, D. M., Immunology beats cancer: a blueprint for successful translation. *Nat Immunol* **2012,** *13* (12), 1129-32.

155. Maus, M. V.; Grupp, S. A.; Porter, D. L.; June, C. H., Antibody-modified T cells: CARs take the front seat for hematologic malignancies. *Blood* **2014,** *123* (17), 2625-2635.

156. Dai, H. R.; Wang, Y.; Lu, X. C.; Han, W. D., Chimeric Antigen Receptors Modified T-Cells for Cancer Therapy. *Jnci-J Natl Cancer I* **2016,** *108* (7).

157. Barrett, D. M.; Singh, N.; Porter, D. L.; Grupp, S. A.; June, C. H., Chimeric Antigen Receptor Therapy for Cancer. *Annu Rev Med* **2014,** *65*, 333-347.

158. Sharpe, M.; Mount, N., Genetically modified T cells in cancer therapy: opportunities and challenges. *Dis Model Mech* **2015,** *8* (4), 337-350.

159. Dotti, G.; Gottschalk, S.; Savoldo, B.; Brenner, M. K., Design and development of therapies using chimeric antigen receptor-expressing T cells. *Immunological Reviews* **2014,** *257* (1), 107-126.

160. Chen, L. P.; Han, X., Anti-PD-1/PD-L1 therapy of human cancer: past, present, and future. *Journal of Clinical Investigation* **2015,** *125* (9), 3384-3391.

161. Ren, J. T.; Liu, X. J.; Fang, C. Y.; Jiang, S. G.; June, C. H.; Zhao, Y. B., Multiplex Cripsr/Cas9 Genome Editing to Generate Potent Universal CART and PD1-Deficient Cells Against Leukemia. *Blood* **2015,** *126* (23).

162. Su, S.; Hu, B.; Shao, J.; Shen, B.; Du, J.; Du, Y. N.; Zhou, J. K.; Yu, L. X.; Zhang, L. R.; Chen, F. J.; Sha, H. Z.; Cheng, L.; Meng, F. Y.; Zou, Z. Y.; Huang, X. X.; Liu, B. R., CRISPR-Cas9 mediated efficient PD-1 disruption on human primary T cells from cancer patients. *Sci Rep-Uk* **2016,** *6*.

163. Welstead, G.; Fang, J.; Nye, C.; Buquicchio, F.; Collins, M.; Selleck, W.; Jayaram, H.; Salmon, R.; Baturevych, A.; Mudri, S.; Jones, J.; Bumcrot, D.; Sather, B. D.,

Successful Generation of CAR+PD-1(-) Primary T Cells Using Cas9-Mediated Genome Editing. *Mol Ther* **2016,** *24*, S229-S229.

164. Cherkassky, L.; Morello, A.; Villena-Vargas, J.; Feng, Y.; Dimitrov, D. S.; Jones, D. R.; Sadelain, M.; Adusumilli, P. S., Human CAR T cells with cell-intrinsic PD-1 checkpoint blockade resist tumor-mediated inhibition. *Journal of Clinical Investigation* **2016,** *126* (8), 3130-3144.

165. Mizushima, S.; Nagata, S., Pef-Bos, a Powerful Mammalian Expression Vector. *Nucleic acids research* **1990,** *18* (17), 5322-5322.

166. Vernon-Wilson, E. F.; Kee, W. J.; Willis, A. C.; Barclay, A. N.; Simmons, D. L.; Brown, M. H., CD47 is a ligand for rat macrophage membrane signal regulatory protein SIRP (OX41) and human SIRP alpha 1. *European Journal of Immunology* **2000,** *30* (8), 2130-2137.

167. Follenzi, A.; Ailles, L. E.; Bakovic, S.; Geuna, M.; Naldini, L., Gene transfer by lentiviral vectors is limited by nuclear translocation and rescued by HIV-1 pol sequences. *Nature Genetics* **2000,** *25* (2), 217-+.

168. Chen, C. L.; Lin, C. F.; Chang, W. T.; Huang, W. C.; Teng, C. F.; Lin, Y. S., Ceramide induces p38 MAPK and JNK activation through a mechanism involving a thioredoxin-interacting protein-mediated pathway. *Blood* **2008,** *111* (8), 4365-4374.

169. Huyer, G.; Liu, S.; Kelly, J.; Moffat, J.; Payette, P.; Kennedy, B.; Tsaprailis, G.; Gresser, M. J.; Ramachandran, C., Mechanism of inhibition of protein-tyrosine phosphatases by vanadate and pervanadate. *Journal of Biological Chemistry* **1997,** *272* (2), 843-851.

170. Hinman, L. E.; Sammak, P. J., Intensity modulation of pseudocolor images. *Biotechniques* **1998,** *25* (1), 124-8.

171. Otsu, N., Threshold Selection Method from Gray-Level Histograms. *Ieee T Syst Man Cyb* **1979,** *9* (1), 62-66.

172. Hatada, M. H.; Lu, X. D.; Laird, E. R.; Green, J.; Morgenstern, J. P.; Lou, M. Z.; Marr, C. S.; Phillips, T. B.; Ram, M. K.; Theriault, K.; Zoller, M. J.; Karas, J. L.,

Molecular basis for interaction of the protein tyrosine kinase ZAP-70 with the T-cell receptor (vol 377, pg 32, 1995). *Nature* **2007,** *446* (7137), 824-824.

173. Arias-Palomo, E.; Recuero-Checa, M. A.; Bustelo, X. R.; Llorca, O., 3D structure of Syk kinase determined by single-particle electron microscopy. *Bba-Proteins Proteom* **2007,** *1774* (12), 1493-1499.

174. Yan, Q.; Barros, T.; Visperas, P. R.; Deindl, S.; Kadlecek, T. A.; Weiss, A.; Kuriyan, J., Structural basis for activation of ZAP-70 by phosphorylation of the SH2-kinase linker. *Mol Cell Biol* **2013,** *33* (11), 2188-201.

175. Adachi, T.; Wienands, J.; Tsubata, T.; Kurosaki, T., Interdomain A is crucial for ITAM-dependent and -independent regulation of Syk. *Biochem Biophys Res Commun* **2007,** *364* (1), 111-7.

176. Boussiotis, V. A.; Chatterjee, P.; Li, L., Biochemical signaling of PD-1 on T cells and its functional implications. *Cancer J* **2014,** *20* (4), 265-71.

177. Grenga, I.; Donahue, R. N.; Lepone, L.; Bame, J.; Schlom, J.; Farsaci, B., PD-L1 and MHC-I expression in 19 human tumor cell lines and modulation by interferon-gamma treatment. *Journal for immunotherapy of cancer* **2014,** *2* (3), P102.